ISSN 1949-8470 (online)

World Journal of *Radiology*

World J Radiol 2022 June 28; 14(6): 114-179

Published by Baishideng Publishing Group Inc

World Journal of Radiology

Contents

Monthly Volume 14 Number 6 June 28, 2022

World Journal of Radiology

Monthly Volume 14 Number 6 June 28, 2022

Contents

ABOUT COVER

Editorial Board Member of *World Journal of Radiology*, Jaber S Alqahtani, MSc, PhD, Academic Research, Assistant Professor, Research Scientist, Department of Respiratory Care, Prince Sultan Military College of Health Sciences, Dammam 34313, Saudi Arabia. Alqahtani-Jaber@hotmail.com

AIMS AND SCOPE

The primary aim of *World Journal of Radiology* (*WJR*, *World J Radiol*) is to provide scholars and readers from various fields of radiology with a platform to publish high-quality basic and clinical research articles and communicate their research findings online.

WJR mainly publishes articles reporting research results and findings obtained in the field of radiology and covering a wide range of topics including state of the art information on cardiopulmonary imaging, gastrointestinal imaging, genitourinary imaging, musculoskeletal imaging, neuroradiology/head and neck imaging, nuclear medicine and molecular imaging, pediatric imaging, vascular and interventional radiology, and women's imaging.

INDEXING/ABSTRACTING

The *WJR* is now abstracted and indexed in Emerging Sources Citation Index (Web of Science), PubMed, PubMed Central, Reference Citation Analysis, China National Knowledge Infrastructure, China Science and Technology Journal Database, and Superstar Journals Database. The 2021 edition of Journal Citation Reports® cites the 2020 Journal Citation Indicator (JCI) for *WJR* as 0.51.

RESPONSIBLE EDITORS FOR THIS ISSUE

NAME OF JOURNAL
World Journal of Radiology

ISSN
ISSN 1949-8470 (online)

LAUNCH DATE
January 31, 2009

FREQUENCY
Monthly

EDITORS-IN-CHIEF
Thomas J Vogl

EDITORIAL BOARD MEMBERS
https://www.wjgnet.com/1949-8470/editorialboard.htm

PUBLICATION DATE
June 28, 2022

INSTRUCTIONS TO AUTHORS
https://www.wjgnet.com/bpg/gerinfo/204

GUIDELINES FOR ETHICS DOCUMENTS
https://www.wjgnet.com/bpg/GerInfo/287

GUIDELINES FOR NON-NATIVE SPEAKERS OF ENGLISH
https://www.wjgnet.com/bpg/gerinfo/240

PUBLICATION ETHICS
https://www.wjgnet.com/bpg/GerInfo/288

PUBLICATION MISCONDUCT
https://www.wjgnet.com/bpg/gerinfo/208

ARTICLE PROCESSING CHARGE
https://www.wjgnet.com/bpg/gerinfo/242

STEPS FOR SUBMITTING MANUSCRIPTS
https://www.wjgnet.com/bpg/GerInfo/239

ONLINE SUBMISSION
https://www.f6publishing.com

World Journal of Radiology

Submit a Manuscript: https://www.f6publishing.com

World J Radiol 2022 June 28; 14(6): 114-136

DOI: 10.4329/wjr.v14.i6.114

ISSN 1949-8470 (online)

REVIEW

Tuberculosis conundrum - current and future scenarios: A proposed comprehensive approach combining laboratory, imaging, and computing advances

Suleman Adam Merchant, Mohd Javed Saifullah Shaikh, Prakash Nadkarni

Specialty type: Radiology, nuclear medicine and medical imaging

Provenance and peer review: Invited article; Externally peer reviewed.

Peer-review model: Single blind

Peer-review report's scientific quality classification

Grade A (Excellent): A
Grade B (Very good): B
Grade C (Good): C, C
Grade D (Fair): 0
Grade E (Poor): 0

P-Reviewer: Barbosa OA, Brazil; Phan LMT, South Korea; Primadhi RA, Indonesia

A-Editor: Zhu JQ, United States

Received: January 17, 2022
Peer-review started: January 17, 2022
First decision: March 16, 2022
Revised: April 17, 2022
Accepted: May 27, 2022
Article in press: May 27, 2022
Published online: June 28, 2022

Suleman Adam Merchant, Lokmanya Tilak Municipal Medical College and General Hospital, Mumbai 400022, Maharashtra, India

Mohd Javed Saifullah Shaikh, Department of Radiology, North Bengal Neuro Centre, Jupiter magnetic resonance imaging, Diagnostic Centre, Siliguri 734003, West Bengal, India

Prakash Nadkarni, College of Nursing, University of Iowa, Iowa 52242, IA, United States

Corresponding author: Suleman Adam Merchant, MBBS, MD, Former Dean, Professor & Head (Radiology), Lokmanya Tilak Municipal Medical College and General Hospital, Sion Hospital, Mumbai 400022, Maharashtra, India. suleman.a.merchant@gmail.com

Abstract

Tuberculosis (TB) remains a global threat, with the rise of multiple and extensively drug resistant TB posing additional challenges. The International health community has set various 5-yearly targets for TB elimination: mathematical modelling suggests that a 2050 target is feasible with a strategy combining better diagnostics, drugs, and vaccines to detect and treat both latent and active infection. The availability of rapid and highly sensitive diagnostic tools (GeneXpert, TB-Quick) will vastly facilitate population-level identification of TB (including rifampicin resistance and through it, multi-drug-resistant TB). Basic-research advances have illuminated molecular mechanisms in TB, including the protective role of Vitamin D. Also, Mycobacterium tuberculosis impairs the host immune response through epigenetic mechanisms (histone-binding modulation). Imaging will continue to be key, both for initial diagnosis and follow-up. We discuss advances in multiple imaging modalities to evaluate TB tissue changes, such as molecular imaging techniques (including pathogen-specific positron emission tomography imaging agents), non-invasive temporal monitoring, and computing enhancements to improve data acquisition and reduce scan times. Big data analysis and Artificial Intelligence (AI) algorithms, notably in the AI subfield called "Deep Learning", can potentially increase the speed and accuracy of diagnosis. Additionally, Federated learning makes multi-institutional/multi-city AI-based collaborations possible without sharing identifiable patient data. More powerful hardware designs - *e.g.*, Edge and Quantum Computing- will facilitate the role of computing applications in TB. However, "Artificial Intelligence needs real Intelligence to guide it!" To have maximal impact, AI must use a holistic

approach that incorporates time tested human wisdom gained over decades from the full gamut of TB, *i.e.*, key imaging and clinical parameters, including prognostic indicators, plus bacterial and epidemiologic data. We propose a similar holistic approach at the level of national/international policy formulation and implementation, to enable effective culmination of TB's endgame, summarizing it with the acronym "TB - REVISITED".

Key Words: Tuberculosis; Radiology; GenXpert; Artificial intelligence; Molecular imaging; Quantum computing

Core Tip: A Holistic (comprehensive) approach is suggested to achieve tuberculosis (TB) elimination goals. Early diagnosis especially for Multi-Drug Resistant TB. Utility of Modern Rapid Diagnostic Tools. The role of Imaging in TB and key radiological signs. Comprehensive Artificial Intelligence(AI) algorithms incorporating key Imaging and clinical signs. The role of Vitamin D supplementation in complementing the TB drug regimen. Molecular Imaging. Quantum Computing and other perspectives in TB strategies to help achieve the various targets set for elimination of TB. A unified Global approach with edge computing/ dashboards and other technological innovations.

Citation: Merchant SA, Shaikh MJS, Nadkarni P. Tuberculosis conundrum - current and future scenarios: A proposed comprehensive approach combining laboratory, imaging, and computing advances. *World J Radiol* 2022; 14(6): 114-136
URL: https://www.wjgnet.com/1949-8470/full/v14/i6/114.htm
DOI: https://dx.doi.org/10.4329/wjr.v14.i6.114

INTRODUCTION

Nearly 1.5 centuries after Robert Koch discovered *Mycobacterium tuberculosis* (MTB) in 1882, tuberculosis (TB) remains a global threat and a deadly human pathogen, ubiquitous enough to comprise an occupational hazard for medical personnel in many locales. Its high prevalence in both immunocompetent and immunocompromised individuals historically made TB a top-10 cause of death worldwide and the leading cause of death from a single infectious agent, though it fell to 13th after being overtaken by COVID-19 in 2021[1]. 95% of cases and deaths occur in developing countries. About one-quarter of the world's population has a TB infection, though most are not (yet) symptomatic and contagious[2]. Because people with active TB can infect 5-15 other people through close contact over a single year, the consequence of delayed/missed diagnosis cascade[2]. However, TB is curable and preventable[2].

The incessant rise of Multidrug-resistant TB (MDR-TB) and extensively drug-resistant (XDR) TB, either primary or acquired, pose an additional challenge[3,4]. Incidence of either varies in different studies: More concerning, only 1/3rd of such individuals accessed treatment in 2020[2].

The three countries with the largest share of the global burden in 2019 were India (27%, 2.8 million cases annually, 150,000 MDR-TB cases every year), China (14%), and the Russian Federation (8%)[5,6]. In 2020, an estimated 10 million people fell ill with TB worldwide. The largest number of new TB cases occurred in the WHO South-East Asian Region (43%), African Region (25%), and Western Pacific (18%)[2]. In descending case-count order, eight countries account for two thirds of the total: India, China, Indonesia, the Philippines, Pakistan, Nigeria, Bangladesh, and South Africa[2].

Ending the TB epidemic by 2030 is among the health targets of the United Nations Sustainable Development Goals[2]. The End TB Strategy defines five-yearly milestones/targets for reducing TB cases and deaths. The targets for 2030 are a 90% reduction in TB deaths and an 80% reduction in new cases per year, compared with levels in 2015, with a reduction in new cases to < 1 per million population annually by 2050[7,8].

DIAGNOSIS OF TB

MDR-TB: Advances in laboratory diagnosis

MDR-TB is defined as an infection with MTB strains non-responsive to isoniazid (INH) and rifampicin (RIF), the 2 most effective first-line anti-TB drugs. Mutations in the INH and RIF resistance gene confers high competitive fitness, favoring their spread: >90% of RIF-resistant strains are also INH-resistant[9-11]. Most people develop MDR-TB because of delayed or incomplete treatment, increasing subsequent

healthcare costs dramatically[12]. MDR-TB is curable with second-line drugs: In 2018, the treatment success rate of MDR-TB patients was 59% worldwide. The earlier treatment regimens for up to 2 years have been superseded by WHO's updated (2021) recommendation for shorter (9-11 mo) and fully oral regimens, which increase compliance greatly[2,13,14]. Previously laboratory confirmation of TB by culture required 6-8 wk: Diagnosing MDR-TB, which used to be exclusively clinical, involved delays of up to 4 mo to identify therapeutic response failure; coupled with persistently positive sputum smears after 4 mo of regular treatment with a first-line DOTS (Directly Observed Treatment, Short-course Regimen)[15-17]. Such therapeutic setbacks especially impacted impoverished or illiterate patients psychologically: after expecting a treatment duration of 7-9 mo only, to be informed halfway through that a new regimen was necessary, they often stopped treatment and were lost to follow-up, eventually spreading MDR-TB to others, exponentially. The spread of MDR-TB was also worsened by policies of using the much cheaper 'regular TB' drug regimen empirically: Treating MDR-TB is 5-200 times more expensive than treating nondrug resistant TB[18].

However, PCR based technologies such as cartridge based nucleic acid amplification techniques [CBNAAT] (GeneXpert®, Cepheid United States, introduced in 2010), can now rapidly detect both MTB genetic material from sputum samples and RIF resistance within 2 h using the current generation of technology, without requiring special technicians/rooms and barely occupying the space of a computer printer, at a cost of $5/test[19,12]. This has been called the most exciting innovation in TB diagnostics in over a century[12]. It is recommended by WHO, which developed policies/guidelines and monitoring frameworks for its use to support developing countries' Ministries of Health (MOHs) in their implementation[12,20]. The latest GeneXpert technology (MTB/RIF Ultra) has a ten-fold improvement in the lower limit of TB detection, and improves differentiation of certain silent mutations, RIF resistance detection in mixed infections (in 3-7 d), increased specificity in detecting RIF resistance in paucibacillary specimens, and better sensitivity in both pulmonary samples and extrapulmonary samples such as pleural/ascitic fluid and biopsied material such as lymph nodes[12,19,21-23]. Our group were amongst the first to successfully use it for lymph nodes and also to recommend the same being used to detect MDR TB upfront.

TB-QUICK is a recent ultrasensitive MTB detection platform which combines loop-mediated isothermal amplification and clustered regularly interspaced short palindromic repeats (CRISPR)-Cas12b reaction for M TB detection. It is highly sensitive (with a near single-copy sensitivity), requires less sample input and offers even a shorter turnaround time than Gene-Xpert for RIF resistance[24].

In South Africa, national screening of high-risk groups [*e.g.*, human immunodeficiency virus (HIV)-infected individuals), deployment of Gene-Xpert machines, treating latent TB, and using quality MTB drugs with shorter regimens led to a decline in TB[25]. We suggest that an identical approach be deployed elsewhere to control the spread of this dreaded scourge.

Overall, TB, either incident or prevalent, is found in 4.1% of the MDR-TB contacts, which is higher than the corresponding prevalence rates of 1.9% and 1.7% reported among household contacts of drug-susceptible TB in the same locality[26,27]. In a study it was shown that RFLP analysis confirmed the transmission of MDR-TB among household contacts while regression analysis showed XDR-TB had an even higher risk of household transmission among all MDR-TB cases[28]. We have successfully used CBNAAT to diagnose extrapulmonary TB, and feel this has tremendous potential to revolutionize TB, especially MDR-TB early diagnosis, treatment, and further management. Piatek *et al*[12] and Mechal *et al*[23] have independently reported the same.

National TB control programs are working to eliminate TB mainly by intensifying efforts to find and cure patients with active disease. Mathematical models developed by Dye and Williams[29] suggest that, while most TB patients can be cured with present drug regimens, the 2050 target is far more likely to be achieved with a synergistic combination of diagnostics, drugs, and vaccines to detect and treat both latent infection and active disease.

IMAGING METHODS IN TUBERCULOSIS

Note: While interventional radiology plays a major role in TB treatment, we deliberately limit this review's scope to diagnostic/prognostic imaging.

TB has a known propensity for dissemination from its primary site and can affect virtually any organ system in the body. It therefore demonstrates a variety of clinical and radiologic findings and can mimic numerous other diseases[30]. Hence, the role of imaging in TB has grown exponentially. The possibility of TB is often first suggested on an imaging study, particularly in relatively inaccessible sites.

In a known case of TB, imaging is often requested to assess the extent of disease, evaluate response to therapy, or detect residual infection after completion of anti-TB therapy. Imaging is also vital in guiding aspiration biopsies, therapeutic drainage of collections of pathological fluid *etc*[31]. Hence, Radiologists will continue to play a vital role in eliminating TB.

Imaging findings in TB depend upon the extent of the disease process. Familiarity with various imaging features permits early diagnosis and prompt management, thereby reducing patient morbidity [30].

In this section, we will also refer to various techniques that fall into the category of "Molecular Imaging Technology" (MIT). MIT visualizes molecules of relevance to a disease at both microscopic levels and in living subjects. For the latter, it provides 3D spatial characterization (often using existing imaging modalities) and non-invasive, temporal monitoring within the same subject[32]. MIT may augment TB research by advancing fundamental knowledge and accelerating the development of novel diagnostics, biomarkers, and therapeutics[32].

Conventional Chest radiography

While radiology training has moved away from conventional radiology, most of the developing world's population cannot access tomographic (cross sectional) imaging readily for logistic or financial reasons. Therefore, the time-tested signs/patterns of TB in conventional chest X-ray (CXR) cannot be forgotten. There is no excuse for missing a Ghon's focus/complex or lamellar effusion of childhood TB in a CXR taken for a different purpose (Figure 1). CXR has high sensitivity but limited specificity for detecting pulmonary TB. As recommended by WHO's guidelines, it is very suitable for TB screening and triaging, to stratify for risk, assess asymptomatic active disease, and for follow-up[33]. Stability of radiographic findings for 6 mo distinguishes inactive from active disease. Where CT is unavailable, lordotic view and penetrated (high kV) views improve depiction of the lung apices and mediastinal/carinal nodes, respectively[34]. Dual-energy radiography with bone subtraction, has also been used to improve depiction of the lung apices[34].

Ultrasonography

Ultrasonography (US) is one of the commonest recommended examinations for TB, including in the evaluation of suspected/affected lymph nodes and for guiding biopsies for the same. Basic details are well known and beyond the scope of this manuscript. It is a very useful non-invasive examination method in children including those with cervical lymphadenitis (across age groups). The US signs of hilar absence, short to long axis (S/L) ratio ≥ 0.5, an unclear edge, necrosis, an echogenic thin layer, strong echoes and capsular or peripheral vascularity; may aid in the diagnosis of cervical tuberculous lymphadenitis[35]. Endobronchial US-guided fine-needle aspiration biopsy for intrathoracic TB lymphadenopathy is valuable when bronchoalveolar lavage and sputum culture are ambiguous[36].

US elastography: [Strain/shear wave] is useful for further evaluation of lymph nodes and the detection of complications such as fibrosis[37,38]. US elastography (USE) techniques are classified by the type of excitation applied: (1) Strain elastography; and (2) Shear wave elastography. Strain elastography includes constant force-induced displacement (static/quasi-static imaging) or acoustic energy-induced physiologic motion. Shear wave elastography is sub-classified as: Transient elastography, point shear wave elastography (pSWE), two-dimensional SWE (2D-SWE), and three-dimensional SWE. Shear wave USE has clear advantages over strain USE by virtue of being quantitative and user independent. However, shear wave measurements are effective only till 3 cm depth from the skin surface, as the shear wave signal tends to attenuate rapidly beyond this depth. This though is an ideal depth for evaluating most cervical TB lymph nodes. On the color elastogram, red represents the softest and blue represents the hardest areas, while intermediate stiffness is indicated by green. These colors represent the relative hardness of tissues on the elastogram (Figure 2A-C). The units of measurement are kilopascal (kPA) or Velocity (V) in meters/sec (m/s) - [1 KPa = 3 × V^2(m/s)][39].

Cervical, axillary, and inguinal lymph nodes are easily evaluated by standard USE; and USE has the potential to non-invasively differentiate tuberculous from metastatic lymph nodes because of the latter's greater stiffness[40,41]. On strain USE a cut-off value of 3.0 (strain ratio) has been suggested for determining if a mass/tissue is benign or malignant[42-44]. Shehata *et al*[43] stated that the best shear wave elasticity ratio cut-off value that allows significant differentiation between benign and malignant mass groups was > 4.9. USE also has great potential for marking biopsy sites in a lymph node for collecting samples for confirmation of the disease, as well as for drug sensitivity purposes, especially in drug resistant TB (Figure 2D). The samples collected should also be run through CBNAAT techniques such as GenXpert. This will enable MDR TB to be detected upfront (refer 'diagnosis of TB section).

These non-invasive techniques will be useful both for initial diagnosis and follow-up, including treatment - response assessment and monitoring of sequelae; *e.g.*, post TB medication Liver fibrosis (Figure 3); where avoiding a liver biopsy would be a great boon[38]. Shear wave Elastography features while assessing liver tissue stiffness are as follows: (1) Normal: 1.37 m/s, Metavir F0-F1; (2) Mild Fibrosis: 1.37 - 1.55 m/s, Metavir F2; (3) Advanced Fibrosis: 1.55 - 1.8 m/s, Metavir F3; and (4) Cirrhosis: > 1.8 m/sec, F4[39]. Metavir is an acronym for "meta-analysis of histological data in viral hepatitis".

EUS: EUS elastography has proven to be useful for the evaluation of mediastinal and abdominal lymph nodes and can provide additional information about the structure and pathology of mediastinal and abdominal lymph nodes. It is an excellent method for targeting different areas of the lymph node to avoid unnecessary needle passes in EUS guided biopsies[40].

Multimodal ultrasound imaging: Multimodal ultrasound imaging combines several US modalities simultaneously: Color Doppler US, US elastography, and contrast-enhanced ultrasound (discussed

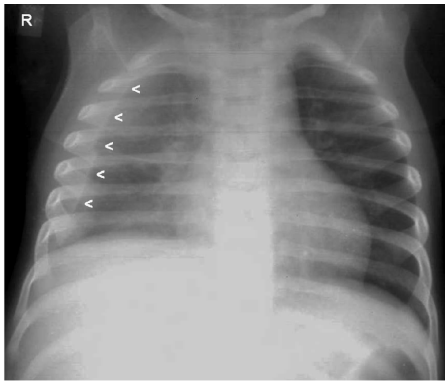

DOI: 10.4329/wjr.v14.i6.114

Figure 1 Lamellar pleural effusion. Frontal chest radiograph of an 18-mo-old child with Pulmonary tuberculosis (primary complex) reveals a lamellar pleural effusion- (homogeneous increased radio-opacity along lateral aspect of right lung field with blunting of the right costophrenic angle- mimicking the appearance of pleural thickening) - [arrowheads]. Image courtesy – Department of Radiology, KEM Hospital, Mumbai.

shortly). It differentiates tuberculous from non-tuberculosis superficial tuberculous lymphadenitis with 100.00% sensitivity and a 94.12% positive predictive value[45].

Micro-Bubbles in diagnosis and theragnostics: "Theragnostics" combines disease diagnosis with therapy[46,47]. Micrometer-sized gas bubbles "micro-bubbles (MB)" allow for intravenous contrast-enhanced US: MBs oscillate resonantly when subjected to high-frequency US, which they reflect intensely[48].

The utility of the same in diagnostic radiology, especially for the urinary tract, is well established[49]. They can readily be utilized for US assessment of vesico-ureteric reflux in patulous golf-hole ureterovesical junctions seen in TB, circumventing the use of ionizing radiation. Kiessling *et al*[50] discuss conjugation of antibodies to the MB surface and incorporation of various molecules inside or onto the MB shell.

MBs have potential for targeted therapies. High-intensity US (HIUS) temporarily disrupts the blood-brain barrier, allowing medications contained in MBs, which HIUS also disrupts, to treat CNS cancers and intracranial TB[50]. Additionally, MBs can deliver medications to TB lymph nodes, as well as gene therapy to tissues exhibiting congenital disease phenotypes[51].

Ultra-high-frequency US and Ultrasound biomicroscopy: Ultrasound biomicroscopy (UBM) is a superb tool to assess superficial TB lesions such as skin TB (lupus vulgaris), both in their diagnosis, as well as during follow up (Figure 4). This is safe and easily repeatable and avoids the use of repeated biopsies. Ma *et al*[48] have designed a small-aperture (0.6 mm × 3 mm) IVUS probe optimized for high-frequency contrast imaging. Their design utilizes a dual-frequency (6.5 MHz/30 MHz) transducer for exciting microbubbles at low frequencies (near their resonance) and detecting their broadband harmonics at high frequencies. Fei *et al*[52] have developed broadband lithium niobate single element ultrasonic transducers in the range of 100-300 MHz for high resolution imaging. They claim a performance comparable to optical resolution and state that availability of ultrahigh frequency transducers will make Ultrasound Biomicroscopy (UBM) a promising tool to study fine biological structures. Future applications of CEUS and UBM could be expected in TB too.

Dark Field Radiography

X-ray dark-field radiography relies on ultra-small-angle scattering (diffraction) of X-rays at the material interfaces within the tissue under investigation[53]. "Dark field", when applied to visible light, refers to the bright appearance of scattering objects on a dark background. Healthy lung tissue, with numerous air/parenchyma interfaces in the alveoli, produces a relatively high signal[54,55]. Introduced experimentally in 2008, Dark field radiography may increase sensitivity for early detection of varied lung pathologies involving the alveoli, including tuberculosis.

Computed Tomography

Computed tomography (CT) enables non-invasive diagnosis of TB in patients with negative sputum examination or no sputum production (as occurs in the follow-up of patients on anti-tuberculosis therapy (ATT) or at presentation) non-invasively: it permits empirical ATT initiation until culture results are obtained[56]. Contrast-enhanced CT is the investigation of choice for evaluating mediastinal LNs and identifying pleural enhancement in empyema (Figure 5). High-resolution CT (HRCT) reconstructions are especially useful to detect miliary and centrilobular nodules, ground-glass opacities,

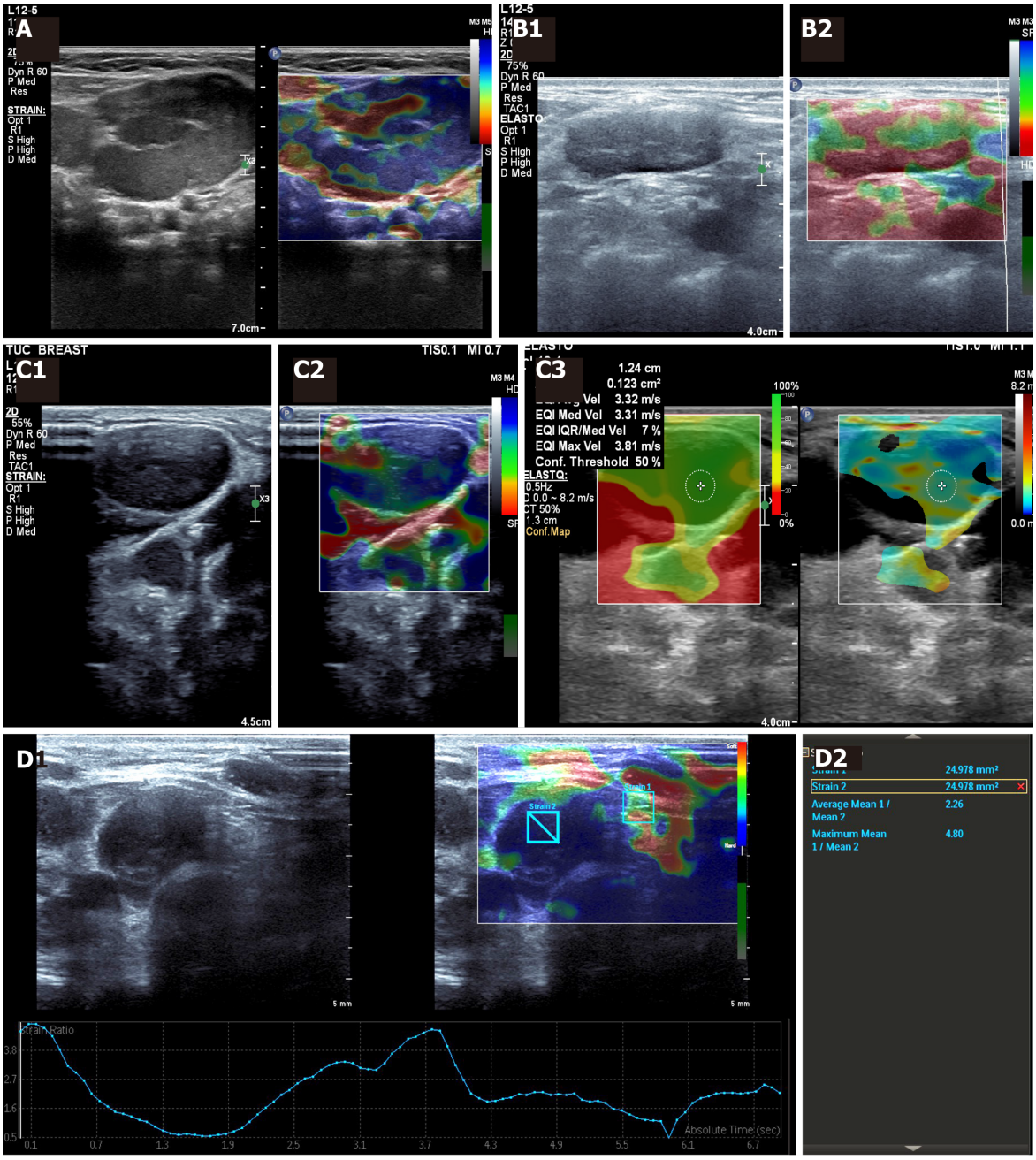

DOI: 10.4329/wjr.v14.i6.114

Figure 2 Cervical tuberculosis lymph node. A: Cervical tuberculosis lymph node: Ultrasonography (US) elastography - central necrotic area appears soft (red); B: Tuberculous lymphadenopathy: A 16-year-old female with fever and neck swelling; B1: Grey scale B-mode image: shows an enlarged lymph node with diffusely hypoechoic echotexture and loss of fatty hilum; B2: Strain US Elastography: Showing a mixed pattern, predominantly soft (red); C: Tuberculous lymphadenopathy: 35-year-old male with neck swelling and history of weight loss; C1: Grey scale image: shows an enlarged lymph node with diffusely hypoechoic echotexture and loss of fatty hilum; C2: Strain US elastography: Showing soft areas within (red areas) s/o necrosis / liquefaction; C3: Shear wave US elastography: Shows relatively low shear wave values; D: Tuberculous lymphadenopathy: Neck US of a 14-year-old female (known case of drug resistant tuberculosis); D1: Grey scale B-mode image: enlarged lymph nodes with diffusely hypoechoic echotexture and loss of fatty hilum; D2: Strain US Elastography: The strain elastography reveals a low strain ratio (2.26). Elastography details are noted on the elastography graph too. Trucut biopsy was done - results awaited. Images courtesy Dr. Chaubal N, Thane Ultrasound Centre, India.

and air-trapping (Figure 6).

Multi-detector CT and its volumetric capability enables earlier and more accurate diagnosis of pulmonary lesions: detection of radiographically occult disease; assessment of disease activity, parenchymal lesions (including miliary TB), mediastinal lymph nodes (LNs), and visualized bones. It also helps evaluate complications like bronchiectasis, cavitation, associated fungal balls, LN necrosis, and pleural/airway/diaphragmatic pathology (Figure 7).

Spectral imaging on CT (dual-/tri-/quad-energy), when it becomes widely available, should further enhance radiologists' diagnostic armamentarium[38]. Khan *et al*[57] concluded that dual energy CT is superior to high-resolution CT for assessing pulmonary TB. Recent CT iterative reconstructions allow

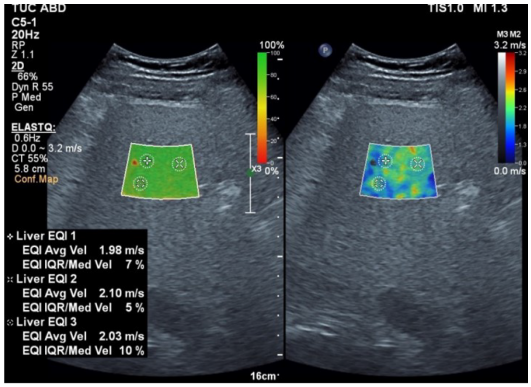

DOI: 10.4329/wjr.v14.i6.114

Figure 3 Shear wave ultrasonography elastography of Liver: 28-year male, on tuberculosis medications for 8 mo, with altered liver functions. Stiffness median - 1.76 metres/sec -- Metavir F3: indicative of Enhanced liver fibrosis. Images courtesy Dr. Chaubal N, Thane Ultrasound Centre, India.

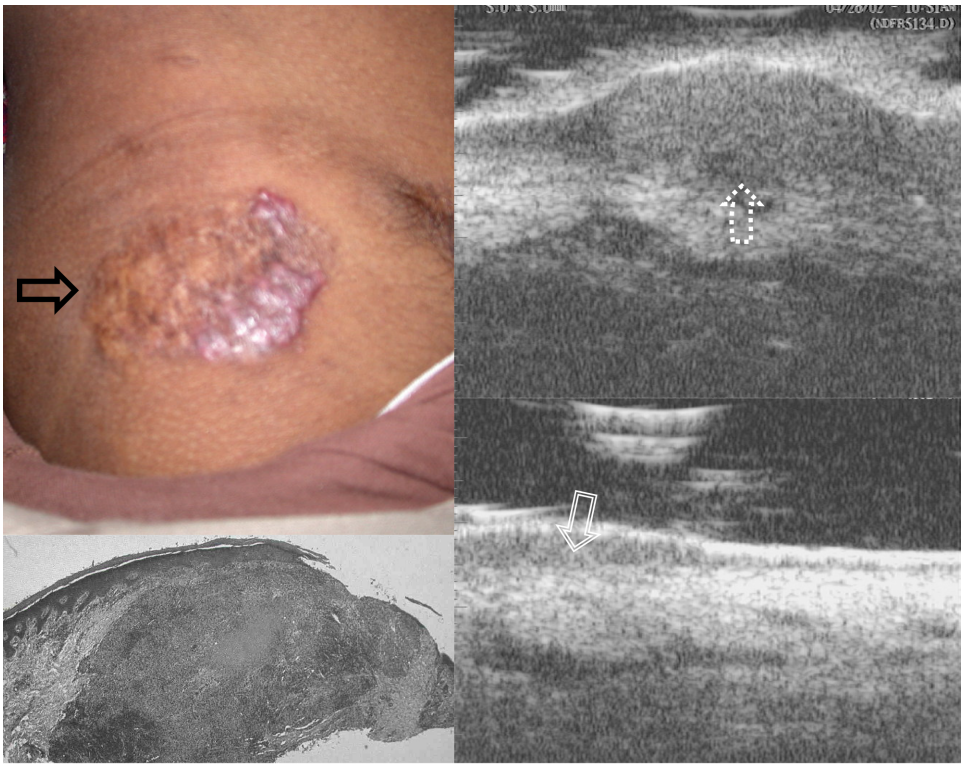

DOI: 10.4329/wjr.v14.i6.114

Figure 4 Ultrasound Biomicroscopy scanned at 50 MHz - Skin tuberculosis - lupus vulgaris. A well-defined reddish-brown plaque with papulo-nodular borders is seen on the skin (black arrow), Ultrasound biomicroscopy (UBM) shows a well-defined heterogenous mass lesion in the dermis (up arrow-dotted), Histopathology shows a well-defined tuberculous granuloma in the dermis (white filled arrow), Follow up UBM after 6 mo of AKT shows marked decrease in the size of granuloma in the dermis (down arrow- dashed). Images Courtesy Dr. Bhatt K, UBM Institute & Sonography Centre, Mumbai.

significant X-ray dose reduction and improved image quality over conventional filtered back-projection reconstruction methods[58]. These advantages would enable greater use of CT in Molecular Imaging.

Magnetic Resonance Imaging

Magnetic resonance imaging (MRI) yields high soft tissue contrast and resolution with high sensitivity for detection of tissue necrosis, as occurs in TB[59]. While MRI lacks the ionizing-radiation hazard, it usually requires longer acquisition times. However, more recently, short-sequence lung MRI (such as HASTE T2, BLADE T2, TRUFI T2 and VIBE T1) have been used for pulmonary imaging in TB patients [60]. Cardiac MRI has made rapid progress too and is the ideal modality for diagnosing Cardiac TB.

Cardiac TB can take the form of Pericarditis, Peri-Myocarditis or a Pancarditis. Pericardial TB is the commonest manifestation of Cardiac TB (Figure 8A and B). In its early form it is seen as pericardial thickening. In advanced cases, pericardial effusion and septations are seen. Accompanying para-spinal

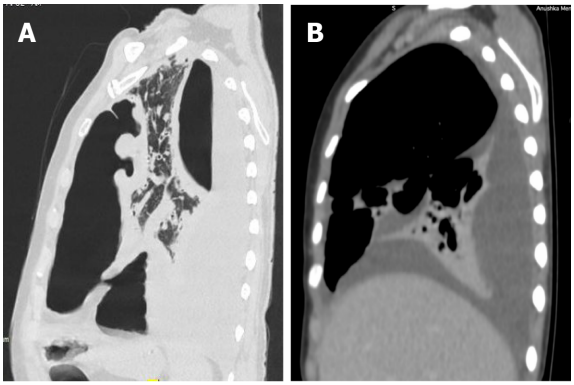

DOI: 10.4329/wjr.v14.i6.114

Figure 5 Tuberculous pyo-pneumothorax. A: Sagittal high-resolution computed tomography image in lung window showing a thick-walled cavity communicating with the left pleural space. A large loculated collection in the left pleural space showing air-fluid level; B: Sagittal image in a mediastinal window showing a Right pleural effusion with partial collapse of Right lower lobe. Images courtesy Dr. Thakkar H, Prof & Head (Radiology), KEM Hospital, Mumbai.

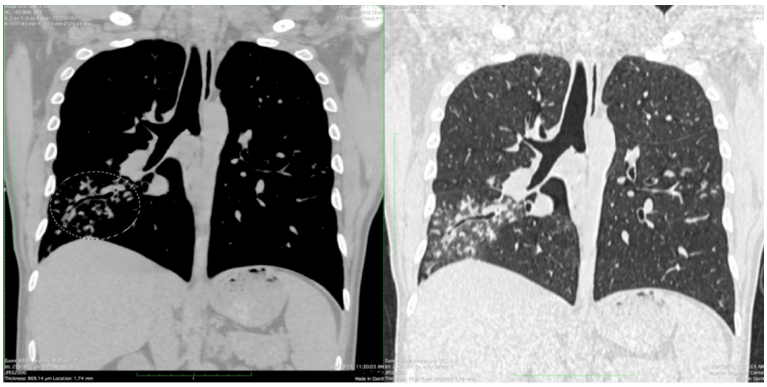

DOI: 10.4329/wjr.v14.i6.114

Figure 6 Endobronchial spread of tuberculosis. Coronal computed tomography images in mediastinal and lung windows; demonstrative of multiple discrete and confluent centrilobular nodules in the lateral basal segment of right lower lobe, some of which show V-Y branching pattern ("tree in bud appearance"- circled area). Enlarged mediastinal lymph nodes are also observed in the subcarinal region. Images courtesy Dr. Joshi A, Prof & Head (Department of Radiology), LTMMC & LTMGH, Mumbai.

abscesses and pleural effusions can easily be seen (Figure 8C). This may resolve on therapy or can undergo calcification. Myocardial TB is rare and in the presence of a myocardial mass lesion, can frequently be misdiagnosed as a neoplasm. The presence of associated diffuse or non-contiguous pericarditis in the presence of myocardial masses is a good pointer to TB etiology of the cardiac masses: The 'Myocarditis - Pericarditis Complex' sign[61] (Figure 9). In a case series of 11 Cardiac TB cases imaged on a 3 Tesla MRI scanner, myocardial lesions were seen in 6 cases (55%) and all of them had concomitant (either diffuse or non-contiguous) pericardial involvement[61]. This is in keeping with the etiopathogenesis of myopericarditis in Cardiac TB. Greater awareness about the "Myopericarditis-Pericarditis Complex" sign/when added to Cardiac AI diagnostic protocols/algorithms, can save the patient from unnecessary invasive tests / cardiac biopsies.

Additionally, novel modalities, such as MR spectroscopy (MRS), chemical exchange saturation transfer (CEST) contrast, Amide Proton transfer imaging and dynamic contrast-enhanced imaging can detect physiological or metabolic changes without the need of exogenous agents. In animal models, these novel MRI capabilities differentiated bacterial infections from sterile inflammation or oncological processes[62,63].

Low-field MRI: Though currently still under development, low-field-strength (and lower-cost) MRI (0.5 T *vs* 1.5 or 3 T for typical scanners), coupled with state-of-the-art hardware, is being evaluated for high-quality imaging lungs and heart[64].

MR spectroscopy: MR spectroscopy (MRS) allows imaging of biochemical processes using endogenous metabolites (*e.g.*, choline, creatine, lactate) or substances labelled with exogenous nuclei such as 19F and 13C. MRS can be performed with most clinical MRI scanners, but multi-voxel MRS scanners are preferred for their greater coverage and resolution. Morales *et al*[65] reported that a singlet peak at ~3.8 parts-per-million (ppm) is present in most tuberculomas and absent in most malignant tumors, allowing

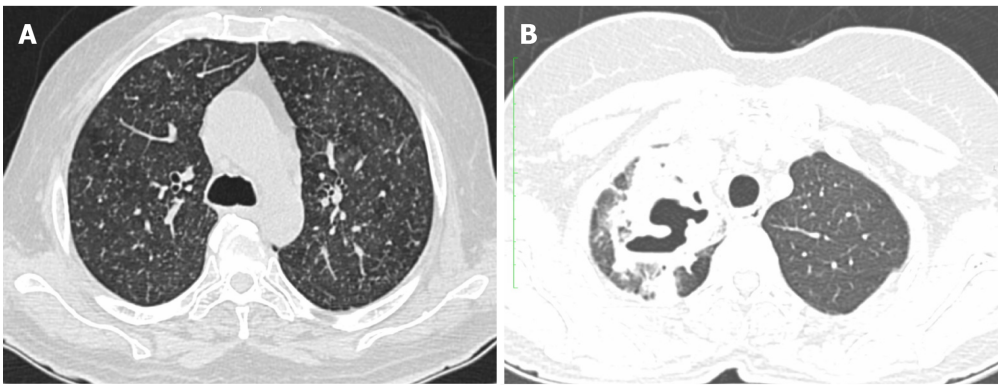

DOI: 10.4329/wjr.v14.i6.114

Figure 7 Tuberculosis sagittal computed tomography. A: Miliary tuberculosis: Axial high-resolution computed tomography (HRCT) image in lung window demonstrates miliary nodules scattered in both lungs; B: Tuberculous cavity: Axial HRCT image in lung window showing a thick-walled cavity in the apical segment of the right upper lobe. Images courtesy Dr. Joshi A, Prof & Head (Department of Radiology), LTMMC & LTMGH, Mumbai.

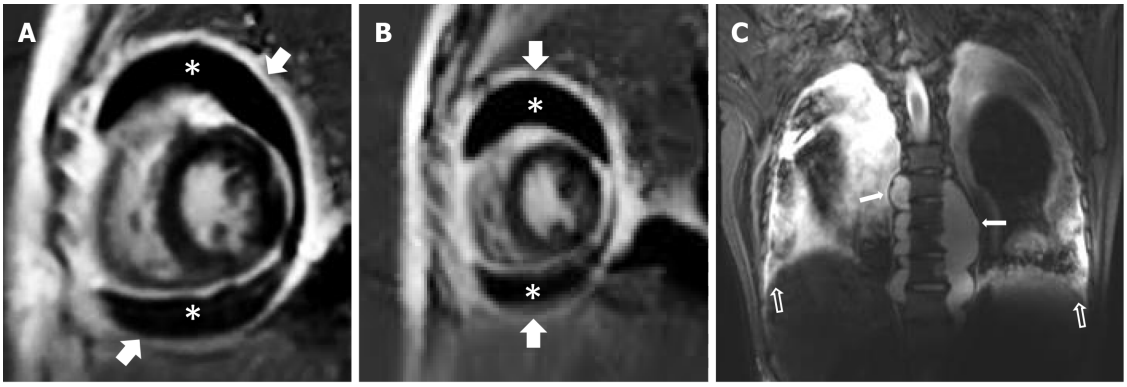

DOI: 10.4329/wjr.v14.i6.114

Figure 8 Tuberculous pericarditis and pericardial effusion: 3 Tesla Cardiac magnetic resonance imaging. A and B: PSIR (short axis view) images shows enhancing pericardial thickening (arrow) and moderate distension of pericardial space with hypointense fluid (asterisk); C: Coronal STIR dorsal spine: Paraspinal abscesses (white arrow -filled) with concomitant pleural effusions (white arrow- unfilled).

differentiation between these lesions.

CEST contrast MRI: CEST contrast MRI uses compounds containing exchangeable protons or molecules in concentrations too low to be visualized using standard MR imaging, with gadolinium substituted by alternative metals, such as manganese, lanthanides, or iron-based agents[66,67]. CEST agents can be diamagnetic or paramagnetic[68]. *Diamagnetic* agents create relatively small chemical shift differences (within 5 ppm of the water signal) that limit the observed effect per injected agent dose. *Paramagnetic* (PARACEST) ions induce much larger shifts, up to a few hundred ppm, thus allowing much shorter proton lifetimes. PARACEST can be single metal-containing chelates (*e.g.*, lanthanides), dendrimers, supramolecules, and liposomes.

Amide proton transfer: Building on the principles of CEST and Magnetization Transfer (MT), amide proton transfer (APT) imaging generates tissue contrast as a function of the mobile amide protons in the tissue's native peptides and intracellular proteins (Figure 10). Tuberculomas demonstrate lower MT ratios (MTR_{asym}) compared to High Grade Gliomas, reflective of a relative paucity of mobile amide protons in the ambient microenvironment. Elevated MTR_{asym} values in the perilesional parenchyma of tuberculomas are a unique observation that may be a clue to the inflammatory milieu[69].

MR elastography: Rapid progress has been noted in the utilisation of MR elastography (MRE), which includes the evaluation of alternatives to the expensive and invasive 'liver biopsy option' for assessing liver fibrosis in patients. Hepatic fibrosis is a known complication of TB medications (ATT) (Figure 11) [70]. Imajo *et al*[71] reported that MRE and US shear wave elastography (2D-SWE) demonstrated excellent diagnostic accuracy in detecting liver fibrosis in patients. They reported that MRE demonstrated the highest diagnostic accuracy for stage 4 fibrosis detection and intra - and inter-observer reproducibility[71]. MRE has the potential to be applied to detection of TB fibrosis in other

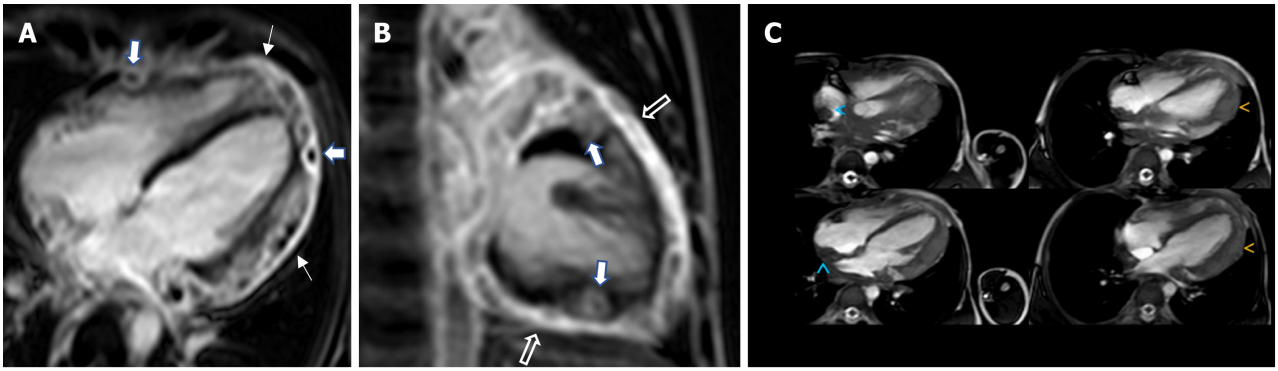

DOI: 10.4329/wjr.v14.i6.114

Figure 9 Cardiac tuberculous myo-pericarditis - 'the myocarditis-pericarditis complex - a sign of cardiac tuberculosis': 3 tesla cardiac magnetic resonance imaging. A: PSIR (4 chamber view -4CH) images shows enhancing pericardial thickening (thin arrow) and peripherally enhancing nodules in the subepicardial myocardium (thick arrow); B: PSIR (VLA view) - Thickened enhancing pericardium (unfilled arrow) with multiple nodular lesions (filled arrow) involving the myo-pericardium; C: Cine 4CH view: Diffuse pericardial thickening (<). In addition, nodular wall thickening (<) of the atria, and the interatrial septum is noted. (The patient was 10-year-old boy with a 2-mo h/o fever and chest pain and responded to anti-tuberculosis medications- regression of the lesions noted).

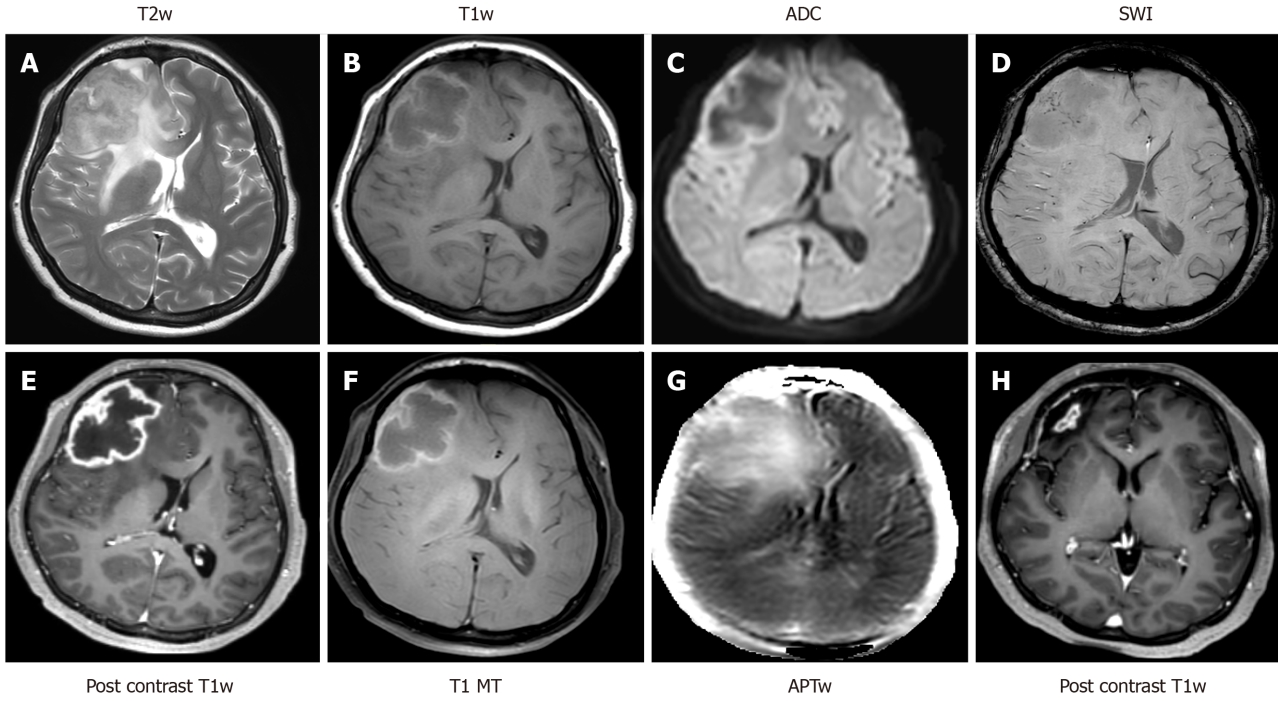

DOI: 10.4329/wjr.v14.i6.114

Figure 10 Magnetic resonance imaging - tuberculoma. A: Axial T2-weighted imaging shows a variable T2 hypointense circumscribed mass lesion in the right anterior frontal region, with surrounding perilesional edema; B: T1 weighted imaging shows a peripheral T1 hyperintense rim; C: Apparent diffusion co-efficient map shows restriction of diffusion; D: Susceptibility weighted imaging demonstrates fine punctate intralesional foci of blooming; E Post contrast T1 weighted imaging showing slightly irregular peripheral rim enhancement; F: T1 magnetization transfer images; G: Amide proton transfer weighted images show elevated magnetization transfer asymmetry in the periphery of the lesion; H: T1 post contrast imaging after completion of anti-tuberculosis treatment reveals significant reduction in the size of the previously seen ring enhancing lesion. APT: Amide proton transfer. Images courtesy Dr. Saini J, Professor, Neuroimaging & IVR, NIMHANS, Bangalore.

organs too, *e.g.* kidney: Including for treatment-response assessment and monitoring of sequelae, as fibrosis is a common manifestation in TB, including during healing[38]. This could be extremely vital in TB ureteric strictures which need to be stented, as they will heal by fibrosis (with treatment); and could result in serious damage/function loss of the affected kidney, if left unstented.

Advances in MR hardware and software: The development of sequences, arrays of coils, k-space strategies, stochastic imaging, and machine learning (ML)-based image analysis procedures will provide numerous opportunities to improve image contrast in MRI[72,73]. MRI sequences and post-processing techniques may replace or decrease the use of contrast agents (for example 4D MRI instead of MRA and CEST imaging); hybrid technologies such as positron emission tomography (PET)/MR may rely on

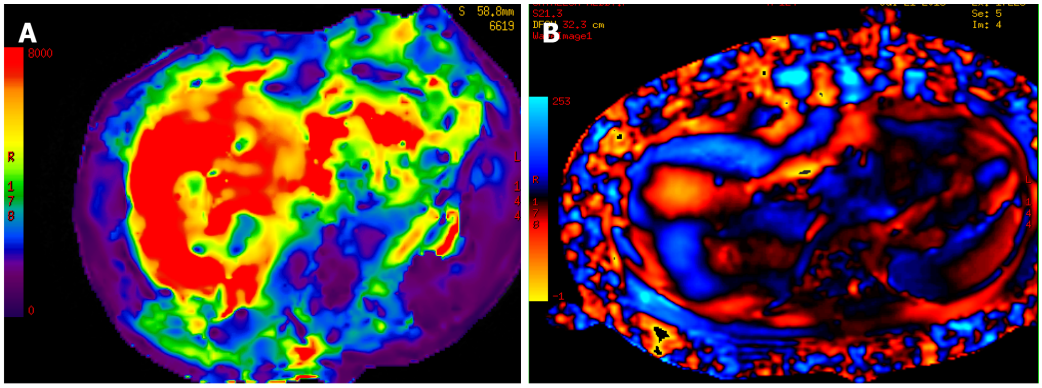

DOI: 10.4329/wjr.v14.i6.114

Figure 11 Post tuberculosis medication liver fibrosis on magnetic resonance elastography. A: Color elastogram of liver with a 0-8kPa scale shows the stiffness distribution in organs for qualitative evaluation. Red or orange regions have higher stiffness values, whereas blue and purple regions are depictive of lower stiffness values. Severe Liver fibrosis is noted - 8.1kPa; B: Wave image of liver shows excellent wave propagation anteriorly and laterally. Low amplitude waves with wave distortion observed in segment VII and II of liver. Images courtesy Dr. Bhaskar N, Vista Imaging Centre, Bangalore.

radiotracers in lieu of MR contrast agents[74].

Nuclear imaging, fusion imaging and miscellaneous

Nuclear imaging detects gamma-radiation produced by radioactive molecules administered non-invasively in micromolar quantities. If such molecules also have biological functions, one visualizes biological processes *in vivo* through functional **images** (at the cost of poorer anatomical resolution compared to CT/MRI/High-res US). Well-established for cancer management, molecular imaging may soon have potential for infectious disease[75].

PET: PET uses radionuclides that decay *via* positron emission relatively quickly (*e.g.*, 18-Fluorine and 11-Carbon have half-lives of 110 and 20 min) and require an on-site cyclotron to make the radionuclides on demand before they decay. Single-photon emission computed tomography (SPECT) uses longer-lived radionuclides (99-metastable-Technetium and 123-Iodine have half-lives of 6 and 13.2 h). In either case, gamma radiation is converted by semiconductor detectors into electrical signals which are then reconstructed as 3D tomographic images.

Pathogen-specific PET imaging agents: Pathogen-specific PET imaging agents currently in development, could provide more accurate data on bacterial burden and other longitudinal information on infection dynamics and treatment responses[76,77].

Fusion imaging: PET CT (Figure 12A and B) and PET MR (Figure 12C) combines functional imaging (PET, SPECT) for pharmacokinetic/ metabolic information with anatomic imaging (CT, MRI) for structural detail. This permits repeated studies in the same subject over time, a fundamental advantage over traditional techniques. Data thus obtained can be supplied to mathematical models of disease progression, which represents a major advance for the field that has primarily relied on snapshots to understand TB[75]. A small study in adults with MDR-TB, 18F-Fluoro-deoxyglucose (18-FDG) PET plus CT showed quantitative changes in computed abnormal volumes at 2 mo into the treatment that predicted long-term treatment success more sensitively than conventional sputum microbiology, suggesting the potential of imaging scans as possible surrogate endpoints in clinical trials of new TB drug regimens[78]. TB reactivation risk in animal models and human subjects has been accurately identified through 18F-FDG PET/CT[79-81].

Explorer total-body PET: This device's increased sensitivity (× 40) allows PET scans at extremely low radiation doses while improving the scan speed (potentially in less than a minute) and can track radiopharmaceuticals for longer periods after injection[82]. Although MDR-TB poses mortality risks comparable to those of many common cancers, radiopharmaceutical imaging, while accepted for cancer workup, is oddly avoided for infectious diseases[83]. Explorer total-body PET could allow increased PET use in both pediatric and adult patients with infectious diseases and would be very useful for assessing the extent of TB, especially when involving multiple sites, including the response to treatment [84-86].

SPECT: A rotating gamma camera captures energies from labelled molecules, which decay *via* the emission of single gamma rays. Most cameras produce 2D images, although some can perform tomographic 3D reconstructions. Foss *et al*[87] have designed a monoclonal antibody mAb 3d29 that can be used to detect and localize areas of infection with M. tuberculosis non-invasively, on SPECT, 24 h

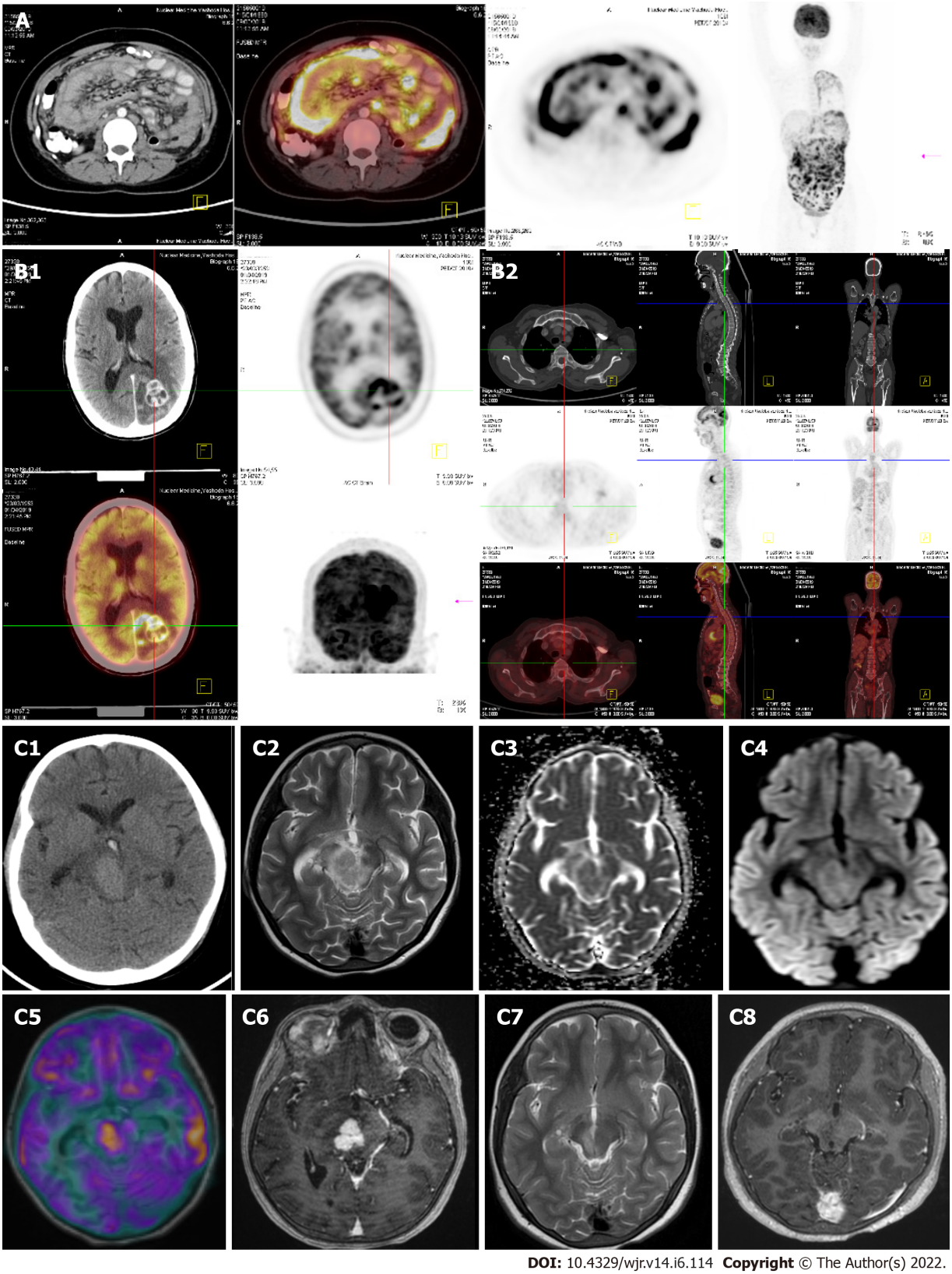

DOI: 10.4329/wjr.v14.i6.114

Figure 12 Fusion imaging. A: Fluoro-deoxyglucose (FDG) positron emission tomography (PET)/computed tomography (CT) Abdominal tuberculosis: 55-year F - h/o loss of weight with mild abdominal pain on and off gradually increasing (for 4 mo). Low grade evening rise of fever. Whole body PET CT showing irregular peritoneal thickening with nodularities and cocoon formation. PET and fused PET-CT images showing significant amount of uptake with SUV max of 12.3; B: Whole body FDG-PET/CT - Brain Tuberculomas:45 years male - h/o seizures for 5 mo, gradually increasing in frequency. PET-CT advised for the possibility of metastases; B1: Whole body FDG-PET/CT done showing irregular ring enhancing lesions in the brain with peri-lesional edema. PET and fused PET-CT images showing significant amount of uptake with SUV max of 14.8; B2: There is no other abnormal uptake in the entire body. (Normal myocardial uptake and left axillary vessel uptake is noted); C: Fusion imaging (MR-PET): Tuberculoma with Rubral tremor. 12-year-old girl presented with right 3rd and 4th cranial nerve palsy along with rhythmic to and fro left 'shoulder joint tremor' which worsened with movement; C1: Axial non-contrast CT image demonstrates a well circumscribed hyperdense mass

lesion within the right half of the midbrain; C2: T2-weighted imaging shows variable T2 hypo intensity within the lesion; C3 and C4: Diffusion weighted imaging and apparent diffusion co-efficient maps reveal restricted diffusion within the lesion; C5: Fusion imaging (T1W and PET) demonstrates avid glucose uptake within the lesion; C6: Post contrast T1 weighted imaging with fat saturation, reveals intense nodular enhancement. Stereotactic biopsy of the lesion revealed granulomatous inflammatory pathology; C7 and C8: After completion of anti-tuberculosis treatment, resolution of the granulomatous lesion with residual gliosis was observed on T2 weighted and Post contrast fat saturated T1w images. Images (A & B) courtesy Dr. Sikander Shaikh, Consultant radiologist, Yashodha Hospital, Hyderabad & Image (C) courtesy Dr. Saini J, Professor, Neuroimaging & IVR, NIMHANS, Bangalore.

after radiotracer injection.

Optical imaging: Optical Imaging provides high-resolution (*e.g.*, single-cell resolution) live imaging in small animal models and has provided very valuable insights into various biological processes (*e.g.*, TB granuloma formation)[32,88]. It is performed with highly sensitive fluorescent or bioluminescent agents. However, the use of low-energy photons means that the depth of penetration is limited to only a few centimetres. These could be used for superficial pathologies *e.g.*, cervical lymph nodes, including their complications (TB lymphadenitis, including collar-stud abscess *etc.*).

Advances in ex vivo molecular imaging and microscopy

Including autoradiography, fluorescence microscopy, fluorescence life-time imaging microscopy (FLIM), matrix assisted laser desorption/ ionization mass spectroscopy imaging (MALDI/MSI): Visualization of molecules based on mass detection. MALDI/MSI can simultaneously detect multiple compounds and provides high spatial resolution. Quantum Microscopy (improving the speed and sensitivity of Raman Scatter Microscopy (SRS); visualizing structures that would otherwise be impossible to see.

The molecular imaging techniques discussed below offer potential for cutting-edge research into the cellular mechanisms of TB. While autoradiography and Fluorescence Microscopy are long-established molecular imaging methods, the newer techniques use different modalities and/or extended study in living tissue.

FLIM: Performed *in vivo* with highly sensitive fluorescent or bioluminescent agents provides high-resolution (*e.g.*, single-cell resolution) in small animal models, allowing visualization of various biological processes (*e.g.*, TB granuloma formation)[32,88,89]. However, the use of low-energy photons limits the depth of penetration to a few centimeters. These could be used for superficial pathologies *e.g.*, cervical lymph nodes, including their complications (TB lymphadenitis, including collar-stud abscess, *etc.*).

Multiphoton intravital microscopy: Multiphoton intravital microscopy (MP-IVM) is based on the simultaneous absorption of two or more (near-) infrared photons. It allows visualization at single-cell resolution within a depth of a few millimeters. Murooka *et al*[90] used MP-IVM to monitor lymphocyte motility in lymph nodes of mice.

Matrix assisted laser desorption/ ionization mass spectroscopy imaging: This visualizes molecules based on mass detection. MALDI/MSI can simultaneously detect multiple compounds with high spatial resolution. It has been used to localize mycobacterial biomarkers and TB drugs in infected tissue[89]. MALDI-MSI can localize multiple molecules (*e.g.*, drugs, metabolites, lipids, proteins) simultaneously, overlaying them onto histologically stained sections to reveal the spatial distribution of each molecule with subcellular resolution[89,90]. MALDI-MSI can also be applied to archived tissue blocks dating back decades[91]. This would be a great boon for research, including retrospective studies.

The transition from anatomical imaging to functional/molecular imaging now allows integration of imaging data with various levels of "omics" data (genomics, metabolomics, proteomics, and pharmacogenomics). This may open new avenues for predictive, preventive, and personalized medicines[58].

Quantum microscopy: Quantum Microscopy has been utilized for improving the speed and sensitivity of SRS microscopy; visualizing structures that would otherwise be impossible to see. Casacio applied squeezed states of light in SRS, developing a quantum-enhanced-microscope[92]. This enhancement allowed for resolution of the cell membrane which could not be seen on a conventional microscope and sub-micron spatial resolution and the improved image contrast and reduced imaging time surpassed the current state-of-the-art Raman microscopes, while avoiding photodamage in the sample.

MOLECULAR MECHANISMS IN TB

Role of vitamin D

Another addition worth considering is the humble Vitamin D, which was used to treat TB in the pre-

antibiotic era[93]. Serum levels of 25-hydroxy-cholecalciferol (25-OH-D3) in TB patients have been shown to be lower than in healthy controls[94]. The vitamin D-cathelicidin pathway regulates the autophagy machinery, protective immune defenses, and inflammation; and contributes to immune cooperation between innate and adaptive immunity[95]. Vitamin D activates macrophages and restricts MTB's intracellular growth[96]. In monocytes and macrophages, MTB lipoprotein binds to the TLR2/TLR1 heterodimer (TLR = Toll-like receptor): this increases vitamin D receptor expression and processing of the pro-vitamin D precursor, which in turn increases production of a mycobactericidal peptide[94]. Vitamin D supplementation during TB treatment accelerates sputum smear conversion and hastens resolution of inflammatory responses[97].

A systematic review (Sutaria *et al*[98]) evaluated 21 randomized, controlled trials and concluded that: (1) TB patients had lower vitamin D status (lower serum levels of 25-OH-D3than healthy, age-matched, and sex-matched controls) [99]; (2) People with certain Vitamin D receptor polymorphisms (BsmI and FokI) had increased susceptibility to TB; and (3) TB patients receiving vitamin D supplementation had improved outcomes in most studies, including shortening treatment duration[98,100]. Vitamin D deficiency may adversely influence TB re-activation/ re-infection: lowered 25-OH-D3 Level leads to a fall in cell-mediated immune defenses, which can activate latent tuberculosis[101]. Hence, it would be worth checking and restoring 25-OH-D3 Levels in malnourished TB patients[102].

Epigenetics perspective

Epigenetics refers to heritable changes in DNA function caused by environmental factors, without altering the DNA sequence, through mechanisms such as DNA (de)methylation (methylation typically deactivates genes) and histone modification (DNA is inactive when tightly bound to histone proteins.) MTB is known to cause histone changes in immune cells that inactivate the defensive IL-2V gene (IL=interleukin), improving MTB's survival chances[103]. Gauba *et al*[104] review various MTB-induced epigenetic mechanisms. In their review, they have unravelled the numerous ways by which MTB re-shapes the host epigenetic landscape as a strategy to overpower the host immune system, for its survival and persistence.

The degree of methylation of key genes in the vitamin D metabolic pathway influence risk and prognosis of tuberculosis[105]. Here's where Vit D supplementation can play a vital role in protecting against TB and in complimenting Anti TB therapies. Understanding the inter-talk between MTB and epigenetic mechanisms will also play a vital role in controlling/ eliminating the scourge of TB[106]. Analysing epigenetic changes offers great potential in the diagnosis, prevention, and treatment strategies for a wide range of diseases, including TB. CRISPR interference (CRISPRi) has been utilized in mycobacteria to identify novel drug targets by the demonstration of gene essentiality. Faulkner *et al*[107] used CRISPRi to study genes involved in mycobacterial antibiotic resistance, restoring Rifampicin sensitivity in M. smegmatis with CRISPR. This offers hope for the future - for the creation of epigenetically modified Anti -TB drugs to treat MDR and XDR TB.

ADVANCES IN COMPUTING

We discuss these advances under two broad categories, software (*e.g.*, Artificial Intelligence, Augmented and Virtual Reality) as well as Hardware Innovations.

Artificial intelligence applications in TB

Increasing Internet bandwidth, coupled with transparent data security, has advanced telemedicine, so that remote diagnosis is now routine. Diagnosis can be assisted by Artificial Intelligence (AI). An important AI sub-field, ML, uses statistical techniques, rather than explicitly encoded insight from human experts, to detect patterns in (often considerable) volumes of data. ML allows classification (*e.g.*, diagnosis) or making predictions. A rapidly progressing branch of ML, called multilayer neural networks or "Deep Learning" (DL), can increase speed and accuracy of onsite and remote diagnosis. DL algorithms have already been used to detect features consistent with pulmonary TB in CXR and CT scans[108].

However, "Artificial Intelligence needs Real Intelligence to guide it!" To maximize AI applications' accuracy and utility in medical diagnosis and treatment modalities, AI must incorporate experiential wisdom accumulated over decades of clinical and radiological experience time, namely time-tested key medical 'teaching' and/or key 'clinical' parameters, including prognostic indicators.

TB is no exception. Take childhood (< 15 years) pulmonary TB, which represents 12% of new cases, but 16% of the estimated 1.4 million deaths[109]. This higher mortality highlights the urgent need to improve case detection, and to identify children without TB disease eligible for preventive treatment. One strategy is systematic screening for tuberculosis in high-risk groups[109]. Early diagnosis and prompt treatment will prevent spread to other children at school or in community settings, especially in resource-limited settings[109]. Imaging algorithms can thus play an important role in screening strategies.

The TB Primary Complex (Ghon's focus, draining lymphatics and hilar node/s) is very common in developing countries. However, inexperienced radiologists find it challenging to identify it in children on CXR, partly because the relatively prominent pulmonary arteries obscure the hila. However, co-occurrence of pleural effusion simplifies identification, because "classical" pleural effusions, especially of the lamellar type (tracking along the pleura, mimicking pleural thickening) (Figure 1) are relatively uncommon in children due to non-TB causes. A Childhood TB diagnosis algorithm using this information would gain in specificity. Similar considerations apply to Adult TB. Patients with "Open Kochs" (lung cavities or smear positive) (Figure 7B) are far more contagious and require isolation: including these factors in analysis/algorithms enables more effective screening/control/management [27].

While DL excels at recognizing individual patterns (most artificial-vision applications use it), higher-level knowledge of key imaging and clinical signs allows integrating the individual patterns into a diagnosis. Such "Holistic" algorithms that integrate all the available information-not just on a single patient, but also molecular and epidemiologic knowledge-can significantly improve not only early detection of TB, including MDR-TB, but more effective management and significant improvement in healthcare outcomes.

Augmented reality and Virtual reality

Virtual reality creates entirely synthesized 3-D environments, while augmented reality (which is technically simpler to create and often more practical) superimposes synthesized content on existing environments, typically under user control. Both are potentially valuable for teaching/simulation and in clinical practice/patient education, by providing novel visualizations. Clinicians/radiologists could walk the patient through their own body to explain the disease, intended intervention, and anticipated post-intervention changes. Such immersive experiences could likely ensure greater compliance with the treatment regimen.

Distributed computing

We introduce distributed computing (DC) because many AI problems, such as would address TB, require computing power that single computing units cannot provide; including data housed in computers at diverse geographical locations. In DC, a computational problem is tackled by multiple, communicating, computing units. It has the following characteristics: (1) The units may lie within a single organization (connected by a local area network) or be distributed geographically (connected by the Internet); (2) Typically, a subset of units (often, just one "central" unit) may operate as either "coordinators" that control/direct other "peripheral" units, or provide resources (*e.g.*, data, computing services) to them; (3) The central units typically have far more CPU power and storage capacity than the peripheral units. In the extreme case, the peripherals may be devices like smartphones, or even single-purpose sensors (*e.g.*, for continuous glucose or EKG monitoring); (4) The central units' upkeep requires skilled/expensive personnel. In Cloud Computing, the units' housing/maintenance are outsourced to a "cloud vendor" (Amazon, Microsoft, Google, *etc.*). The available services can be scaled up or down in each billing cycle based on the customer's requirements. The term "cloud" indicates that the central unit is "out there", its physical location transparent to customers: location may even change; and (5) A single central unit can pose a bottleneck if thousands of small devices connect to it, especially over a sluggish Internet. Edge Computing enhances cloud computing by interposing intermediary units between the peripherals and central units[110]. The Edge units are physically close to the peripherals at a given geographic location (*i.e.*, at the "Edge" of a network diagram). They prevent overwhelming of the central unit, reduce overall network traffic by aggregating inputs from the peripherals and also provide some computing resources.

Federated ML: ML in general, and DL specifically, need lots of data (as well as diverse data from multiple geographic locales) to achieve the desired accuracy. "Big-data" solutions naturally suggest themselves. However, the obvious solution, physical pooling of data, faces the following barriers: (1) Data privacy - which is less of an issue with all forms of digital imaging, where DICOM metadata containing identifiable information can be removed; and (2) Mistrust - a formidable hurdle when academic or commercial consortia bring rivals together.

The technique of *Federated Learning* (FL), originally pioneered by Google as an application of their well-known MapReduce algorithm allows iteratively training an ML model across geographically separated hardware: the ML algorithm is distributed, while data remains local[111,112]. It can be employed for both statistical and deep learning.

Typically, a central server coordinates computations across multiple distributed clients. At start-up, the server sends the clients initialization information. The clients commence computation. When each client is done, it sends only aggregate results back to the server, not detailed or identifiable data elements. The server collates all clients' results and sends updates to each client, which then computes again. The process continues until the ML training completes convergence.

Ng *et al*[113] provide a detailed technology overview. Sheller *et al*[114] use FL to replicate prior analysis of a 10-institution brain-tumor-image-dataset derived from The Cancer Genome Atlas (TCGA). Navia-Vasquez *et al*[115] describe an approach for Federated Logistic Regression.

Most important, many AI algorithms can run in FL mode, making them more accurate because they are based on more voluminous and diverse data. This increases the scope for Multi- Institutional/Multi-city collaborations. Dashboards augmented with these algorithms' can aid key organizational decision-makers to identify trends (including epidemiological), communicate vital information and monitor performance against strategic goals. Better information through technology-assisted developments would aid WHO, UNICEF and other such organizations counter/eliminate the scourge of TB worldwide. While FL works around institutional barriers, one pays a cost in computational speed, which is limited by Internet bandwidth. In almost all cases, this tradeoff is worthwhile.

Quantum technology

"Quantum" technology refers to a highly diverse set of technologies that leverage "quantum mechanics", the physics of sub-atomic particles. Some of these are established, such as scanning tunneling microscopy and photoionization, while others are still largely theoretical, or in the prototype stage[116]. Quantum Computers and Quantum microscopes, new quantum repeaters enabling a scalable super secure Quantum Internet (distance will no longer be a hindrance, not just IOT but 'Intelligent Edge' devices commonplace); will give a quantum boost to Medical Imaging/other health-care Algorithms/strategies, including in other related fields, improving healthcare in ways beyond the realm of dreams[117].

Quantum entanglement microscopy: Quantum entanglement (QE) occurs when a group of particles are generated and interact with each other so that each particle's sub-atomic (*i.e.*, quantum) state cannot be described independently of the others' state. Originally postulated in 1935 by Einstein, Podolsky, and Rosen, it led to seemingly bizarre predictions if true. For example, if one particle encountered an object (*e.g.*, a bacterium), the other particles would reflect this interaction instantaneously - even if the particles were at opposite ends of the universe, violating General Relativity's prediction that faster-than-light interactions are impossible. Such predictions led Einstein to believe that Quantum Theory was erroneous: However, QE was demonstrated experimentally almost eight decades later.

With QE using confocal "differential interference contrast," standard microscopy wavelengths, *e.g.*, visible light or ultraviolet (UV), provides much higher resolution than without QE, demonstrated by Ono *et al*[118]. QE achieves such detail using much less light (useful for light-sensitive micro-organisms or living tissues when UV is employed). A quantum optical counterpart has been developed to the classical Fourier-transform infrared spectrometer[119]. "Quantum ghost imaging" produced the world's first 2D image captured and reconstructed using asynchronous detection. Ghost imaging is well suited to biological and medical applications, in which light-sensitive cell samples can be observed over a long period because the new processes use less light[120]. QE microscopy may thus impact TB research and diagnosis.

Quantum computing: Quantum computing (QC) relies on the possibility of keeping a collection of "qubits" (quantum bits) stable long enough to perform computations with. While a bit (the smallest unit of information in a traditional computer, 1 Byte = 8 bits) can be either 1 or 0, a qubit can be both 1 and 0 simultaneously: thus, 32 qubits can represent 2^{32}approximately equal to 4 billion possibilities. Conceived by Nobelist Richard Feynman, QC's theoretical foundations were strengthened after Peter Shor's work ("Shor's[121] Algorithm) showed that QC could achieve exponential speedup for extremely compute-intensive problems like factorizing the product of two large prime numbers, the basis of RSA (= Rivest, Shamir, Adelman) encryption. Building a practical Quantum Computer, however, is challenging. Qubits are most stable at very low temperatures (*e.g.*, 0.025 Kelvin), and most Qubits in a computer perform error correction rather than computation. However, QC is showing remarkable progress - entangling qubits that could improve error correction in quantum computing, creation of a third state to qubits, to create 'qutrits' that allow more information to be encoded in a single element and decrease readout errors significantly, development of a high-performance source of "squeezed light" used to transmit information in optical quantum computing; all signify a quantum leap in the technology; with the last being a paradigm shift[122-124]. Optical Quantum computers can now be expected to run at room temperature, without the expensive cooling equipment needed for other quantum computers that use superconductors.

A recent simulated quantum algorithm by Case Western Reserve University and Microsoft scientists (it would have required a quantum computer with 1 million computing qubits) addressed Magnetic Resonance Fingerprinting (MRF)[125]. MRF goes beyond MRI in identifying signatures from individual tissues simultaneously.

If QC's hardware challenges are solved (there is no clear-cut timeline for this) the impact on general computing, including AI-deep learning, under the hood, performing mathematical optimization-could be extraordinary. Almost all aspects of healthcare would benefit: TB diagnosis and disease modeling would definitely be a part of it. As quantum computers are also ideally suited for solving complex optimization tasks and performing fast searches of unsorted data, this could be relevant for many applications in healthcare related to TB; medical imaging, epidemiological simulations, dashboard creation, holistic algorithm creation, targeted policy making, to a host of other applications; including the realm of Quantum Artificial Intelligence, which offers unlimited possibilities, including many

presently undreamable/unthinkable ones. Researchers have now suggested that neuromorphic or brain like computers built using memristors (these resemble neuronal synapsis) would perform well at running neural networks[126]. Scientists in Austria and Italy have already developed a quantum version of the memristor that they suggest could lead to 'quantum neuromorphic computers', which in turn could lead to an exponential growth in performance, in an ML approach known as 'reservoir computing 'that excels at learning quickly; and may have a quantum advantage over classical reservoir computing, due to the fact that the memristor, unlike any other quantum component has memory[127].

Thus, the Future looks great for QC (including QC based AI) contributing phenomenally to Medical Imaging and overall Healthcare as well. We can merely speculate at the potential applications of this yet 'Work in Progress' technology. The spectacular jump in overall computing power will enable hitherto unimaginable tasks to be done in a 'jiffy' and thus enable more complex tasks to be thought of. Quantum Artificial Intelligence Algorithms and the like will be something to look forward to. As and when QC evolves the Metaverse will give a more immersive experience both for teaching/simulation and during actual interactions; by giving visualizations/viewpoints that would otherwise not have been possible; with Augmented Reality/Virtual reality (especially for teaching/simulations *etc*.) offering tremendous potential for Medical Imaging in TB, community involvement, amongst other applications; to enable better compliance of TB guidelines and norms (refer the Augmented Reality &/Virtual Reality sectionabove).

CONCLUSION

While we have discussed numerous technologies, which operate at scales ranging from the subatomic to human populations, the primary challenge for employing these to eliminate the scourge of TB is integrating them into a holistic approach. For example, AI cannot operate in a vacuum; it needs large volumes of data at the patient and population level: incorporating data also from novel imaging modalities, or from translational applications of bench-science research (*e.g*., detection of resistance mutations through PCR, augmented optionally by CRISPR), will make it much more useful. The integration must be guided by policies developed by the coordinated actions of international consortia (including bodies like WHO, Big Pharma, national health ministries, philanthropists, *etc*.) that make use of diverse expertise around the globe, including those available through leading-edge technologies.

Below, we provide an outline for the implementation of such policies.

Prevention: In addition to current standard practices (besides the usual methods, nutrition, social norms *etc*.

Screening of vulnerable contacts/populations.

Screening for, and correction of nutritional deficiencies, including vitamin D.

Early diagnosis utilizing newer techniques/technological developments: *e.g*., Gene-Xpert, TB QUICK *etc*., for both 'regular TB' and MDR/XDR TB, including extrapulmonary samples.

Effective treatment, especially for MDR/XDR TB [including addition of recent drugs, shorter duration regimen (for better compliance)] + vitamin D for better healing as well as complimenting the action of various anti-TB drugs.

Effective monitoring including long term follow up coupled with development of large epidemiological data banks and dashboards that summarize the data therein to facilitate timely decision-making.

Enhanced Computing Infrastructure to facilitate all the above, from optimized data gathering, to more sophisticated algorithms, to more powerful hardware architectures.

The following is a useful acronym for the strategies we believe are vital to help us achieve the various targets set by the international health community for elimination of TB.

TB – REVISITED: Regular Screening / Remote patient monitoring; Early Diagnosis; Vitamin D levels/supplementation; Imaging and Investigations; Set up a Holistic Approach (Clinical/Imaging/Bacteriological); Intelligent comprehensive Holistic AI algorithms (+ wisdom *vs* knowledge); Technology – CBNAAT (GenXpert *etc*.)/National - Global Dashboards; Ensure a Global approach/Edge Computing; Do not delay the diagnosis of MDR-TB.

We believe that effective strategy implementation can help alleviate the suffering of millions of underprivileged citizens of the world.

ACKNOWLEDGEMENTS

We wish to thank Merchant N, MD, Diagnostic Radiologist, The Joint Department of Medical Imaging - Lecturer, Faculty of Medicine, University of Toronto, for assistance in preparing this manuscript.

FOOTNOTES

Author contributions: Merchant SA conceptualized the article; all authors wrote, read and approved the final manuscript.

Conflict-of-interest statement: All authors declare no conflict of interests for this article.

Country/Territory of origin: India

ORCID number: Suleman Adam Merchant 0000-0001-6513-450X; Mohd Javed Saifullah Shaikh 0000-0002-5615-4813; Prakash Nadkarni 0000-0002-9628-4700.

S-Editor: Wang LL
L-Editor: A
P-Editor: Wang LL

REFERENCES

1 **WHO**. Global tuberculosis report 2020. [cited 20 January 2022]. Available from: https://www.who.int/publications/i/item/9789240013131
2 **WHO**. Global Tuberculosis Report 2021. [cited 20 January 2022]. Available from: https://www.who.int/publications/i/item/9789240037021
3 **Centers for Disease C and Prevention**. Emergence of Mycobacterium tuberculosis with extensive resistance to second-line drugs-worldwide, 2000-2004. *MMWR Morb Mortal Wkly Rep* 2006; **55**: 301-305 [PMID: 16557213]
4 **Salazar-Austin N**, Ordonez AA, Hsu AJ. Extensively drug-resistant tuberculosis in a young child after travel to India. *Lancet Infect Dis* 2015; **15**: 1485-1491 [PMID: 26607130 DOI: 10.1016/S1473-3099(15)00356-4]
5 **Kanabus A**. TB Statistics - 2020 - deaths, case notifications. [cited 20 January 2022]. Available from: https://tbfacts.org/tb-statistics/(2021)
6 **United States AID**. [cited 20 January 2022]. Available from: https://blog.usaid.gov/2017/
7 **WHO**. Global strategy and targets for tuberculosis prevention, care and control after 2015. Sixty seventh World health Assembly: WORLD HEALTH ORGANISATION. [cited 20 January 2022]. Available from: https://apps.who.int/gb/ebwha/pdf_files/WHA67/A67_R1-en.pdf
8 **Dye C**, Glaziou P, Floyd K. Prospects for tuberculosis elimination. *Annu Rev Public Health* 2013; **34**: 271-286 [PMID: 23244049 DOI: 10.1146/annurev-publhealth-031912-114431]
9 **Lee JH**, Ammerman NC, Nolan S. Prospects for tuberculosis elimination. *Nat Commun* 2012; **3**: 753-753 [PMID: 22434196 DOI: 10.1038/ncomms1724]
10 **Comas I**, Borrell S, Roetzer A. Whole-genome sequencing of rifampicin-resistant Mycobacterium tuberculosis strains identifies compensatory mutations in RNA polymerase genes. *Nat Genet* 2011; **44**: 106-110 [PMID: 22179134 DOI: 10.1038/ng.1038]
11 **Jaleta KN**, Gizachew M, Gelaw B. Rifampicin-resistant Mycobacterium tuberculosis among tuberculosis-presumptive cases at University of Gondar Hospital, northwest Ethiopia. *Infect Drug Resist* 2017; **10**: 185-192 [PMID: 28652786 DOI: 10.2147/IDR.S135935]
12 **Piatek AS**, Van Cleeff M, Alexander H. GeneXpert for TB diagnosis: planned and purposeful implementation. *Glob Health Sci Pract* 2013; **1**: 18-23 [PMID: 25276513 DOI: 10.9745/GHSP-D-12-00004]
13 **WHO**. The shorter mdr-tb regimen. [cited 20 January 2022]. Available from: https://apps.who.int/iris/bitstream/handle/10665/250125/9789241549639-eng.pdf
14 **Mirzayev F**, Viney K, Linh NN, Gonzalez-Angulo L, Gegia M, Jaramillo E, Zignol M, Kasaeva T. World Health Organization recommendations on the treatment of drug-resistant tuberculosis, 2020 update. *Eur Respir J* 2021; **57** [PMID: 33243847 DOI: 10.1183/13993003.03300-2020]
15 **Ogwang S**, Mubiri P, Bark CM, Joloba ML, Boom WH, Johnson JL. Incubation time of Mycobacterium tuberculosis complex sputum cultures in BACTEC MGIT 960: 4weeks of negative culture is enough for physicians to consider alternative diagnoses. *Diagn Microbiol Infect Dis* 2015; **83**: 162-164 [PMID: 26239846 DOI: 10.1016/j.diagmicrobio.2015.07.002]
16 **Chavez Pachas AM**, Blank R, Smith Fawzi MC, Bayona J, Becerra MC, Mitnick CD. Identifying early treatment failure on category I therapy for pulmonary tuberculosis in Lima Ciudad, Peru. *Int J Tuberc Lung Dis* 2004; **8**: 52-58 [PMID: 14974746]
17 **Satti H**, McLaughlin MM, Seung KJ, Becerra MC, Keshavjee S. High risk of drug-resistant tuberculosis when first-line therapy fails in a high HIV prevalence setting. *Int J Tuberc Lung Dis* 2013; **17**: 100-106 [PMID: 23232009 DOI: 10.5588/ijtld.12.0344]
18 **WHO**. Multidrug and extensively drug-resistant TB (M/XDR-TB). 2010. [cited 20 January 2022]. Available from:

http://apps.who.int/iris/bitstream/handle/10665/44286/9789241599191_eng.pdf?sequence=1

19 **Osei Sekyere J**, Maphalala N, Malinga LA, Mbelle NM, Maningi NE. A Comparative Evaluation of the New Genexpert MTB/RIF Ultra and other Rapid Diagnostic Assays for Detecting Tuberculosis in Pulmonary and Extra Pulmonary Specimens. *Sci Rep* 2019; **9**: 16587 [PMID: 31719625 DOI: 10.1038/s41598-019-53086-5]

20 **Helb D**, Jones M, Story E, Boehme C, Wallace E, Ho K, Kop J, Owens MR, Rodgers R, Banada P, Safi H, Blakemore R, Lan NT, Jones-López EC, Levi M, Burday M, Ayakaka I, Mugerwa RD, McMillan B, Winn-Deen E, Christel L, Dailey P, Perkins MD, Persing DH, Alland D. Rapid detection of Mycobacterium tuberculosis and rifampin resistance by use of on-demand, near-patient technology. *J Clin Microbiol* 2010; **48**: 229-237 [PMID: 19864480 DOI: 10.1128/JCM.01463-09]

21 **Perez-Risco D**, Rodriguez-Temporal D, Valledor-Sanchez I, Alcaide F. Evaluation of the Xpert MTB/RIF Ultra Assay for Direct Detection of Mycobacterium tuberculosis Complex in Smear-Negative Extrapulmonary Samples. *J Clin Microbiol* 2018; **56** [PMID: 29950333 DOI: 10.1128/JCM.00659-18]

22 **Dorman SE**, Schumacher SG, Alland D, Nabeta P, Armstrong DT, King B, Hall SL, Chakravorty S, Cirillo DM, Tukvadze N, Bablishvili N, Stevens W, Scott L, Rodrigues C, Kazi MI, Joloba M, Nakiyingi L, Nicol MP, Ghebrekristos Y, Anyango I, Murithi W, Dietze R, Lyrio Peres R, Skrahina A, Auchynka V, Chopra KK, Hanif M, Liu X, Yuan X, Boehme CC, Ellner JJ, Denkinger CM; study team. Xpert MTB/RIF Ultra for detection of Mycobacterium tuberculosis and rifampicin resistance: a prospective multicentre diagnostic accuracy study. *Lancet Infect Dis* 2018; **18**: 76-84 [PMID: 29198911 DOI: 10.1016/S1473-3099(17)30691-6]

23 **Mechal Y**, Benaissa E, El Mrimar N, Benlahlou Y, Bssaibis F, Zegmout A, Chadli M, Malik YS, Touil N, Abid A, Maleb A, Elouennass M. Evaluation of GeneXpert MTB/RIF system performances in the diagnosis of extrapulmonary tuberculosis. *BMC Infect Dis* 2019; **19**: 1069 [PMID: 31856744 DOI: 10.1186/s12879-019-4687-7]

24 **Sam IK**, Chen YY, Ma J, Li SY, Ying RY, Li LX, Ji P, Wang SJ, Xu J, Bao YJ, Zhao GP, Zheng HJ, Wang J, Sha W, Wang Y. TB-QUICK: CRISPR-Cas12b-assisted rapid and sensitive detection of Mycobacterium tuberculosis. *J Infect* 2021; **83**: 54-60 [PMID: 33951419 DOI: 10.1016/j.jinf.2021.04.032]

25 **Churchyard GJ**, Mametja LD, Mvusi L, Ndjeka N, Hesseling AC, Reid A, Babatunde S, Pillay Y. Tuberculosis control in South Africa: successes, challenges and recommendations. *S Afr Med J* 2014; **104**: 244-248 [PMID: 24893501 DOI: 10.7196/samj.7689]

26 **Noertjojo K**, Tam CM, Chan SL, Tan J, Chan-Yeung M. Contact examination for tuberculosis in Hong Kong is useful. *Int J Tuberc Lung Dis* 2002; **6**: 19-24 [PMID: 11931396]

27 **Lee MS**, Leung CC, Kam KM, Wong MY, Leung MC, Tam CM, Leung EC. Early and late tuberculosis risks among close contacts in Hong Kong. *Int J Tuberc Lung Dis* 2008; **12**: 281-287 [PMID: 18284833]

28 **Leung EC**, Leung CC, Kam KM, Yew WW, Chang KC, Leung WM, Tam CM. Transmission of multidrug-resistant and extensively drug-resistant tuberculosis in a metropolitan city. *Eur Respir J* 2013; **41**: 901-908 [PMID: 22878878 DOI: 10.1183/09031936.00071212]

29 **Dye C**, Williams BG. Eliminating human tuberculosis in the twenty-first century. *J R Soc Interface* 2008; **5**: 653-662 [PMID: 17690054 DOI: 10.1098/rsif.2007.1138]

30 **Harisinghani MG**, McLoud TC, Shepard JA, Ko JP, Shroff MM, Mueller PR. Tuberculosis from head to toe. *Radiographics* 2000; **20**: 449-70; quiz 528 [PMID: 10715343 DOI: 10.1148/radiographics.20.2.g00mc12449]

31 **Bomanji JB**, Gupta N, Gulati P, Das CJ. Imaging in tuberculosis. *Cold Spring Harb Perspect Med* 2015; **5** [PMID: 25605754 DOI: 10.1101/cshperspect.a017814]

32 **Ordonez AA**, Tucker EW, Anderson CJ, Carter CL, Ganatra S, Kaushal D, Kramnik I, Lin PL, Madigan CA, Mendez S, Rao J, Savic RM, Tobin DM, Walzl G, Wilkinson RJ, Lacourciere KA, Via LE, Jain SK. Visualizing the dynamics of tuberculosis pathology using molecular imaging. *J Clin Invest* 2021; **131** [PMID: 33645551 DOI: 10.1172/JCI145107]

33 **WHO**. Chest radiography in tuberculosis detection. [cited 20 January 2022]. Available from: https://apps.who.int/iris/handle/10665/252424

34 **Sharma M**, Sandhu MS, Gorsi U, Gupta D, Khandelwal N. Role of digital tomosynthesis and dual energy subtraction digital radiography in detection of parenchymal lesions in active pulmonary tuberculosis. *Eur J Radiol* 2015; **84**: 1820-1827 [PMID: 26071244 DOI: 10.1016/j.ejrad.2015.05.031]

35 **Yu TZ**, Zhang Y, Zhang WZ, Yang GY. Role of ultrasound in the diagnosis of cervical tuberculous lymphadenitis in children. *World J Pediatr* 2021; **17**: 544-550 [PMID: 34472036 DOI: 10.1007/s12519-021-00453-w]

36 **Navani N**, Molyneaux PL, Breen RA, Connell DW, Jepson A, Nankivell M, Brown JM, Morris-Jones S, Ng B, Wickremasinghe M, Lalvani A, Rintoul RC, Santis G, Kon OM, Janes SM. Utility of endobronchial ultrasound-guided transbronchial needle aspiration in patients with tuberculous intrathoracic lymphadenopathy: a multicentre study. *Thorax* 2011; **66**: 889-893 [PMID: 21813622 DOI: 10.1136/thoraxjnl-2011-200063]

37 **Wang B**, Guo Q, Wang JY, Yu Y, Yi AJ, Cui XW, Dietrich CF. Ultrasound Elastography for the Evaluation of Lymph Nodes. *Front Oncol* 2021; **11**: 714660 [PMID: 34485150 DOI: 10.3389/fonc.2021.714660]

38 **Merchant S**, Bharati A, Merchant N. Tuberculosis of the genitourinary system-Urinary tract tuberculosis: Renal tuberculosis-Part II. *Indian J Radiol Imaging* 2013; **23**: 64-77 [PMID: 23986619 DOI: 10.4103/0971-3026.113617]

39 **Chaubal N**, Bam A & Khatdare K. Elastography of Lymph Nodes. In: Richard. G Barr (Ed) Elastography - A Practical Approach. First ed. New York - Stuttgart: Thieme, 2017: 100-114

40 **Dietrich CF**, Jenssen C, Arcidiacono PG, Cui XW, Giovannini M, Hocke M, Iglesias-Garcia J, Saftoiu A, Sun S, Chiorean L. Endoscopic ultrasound: Elastographic lymph node evaluation. *Endosc Ultrasound* 2015; **4**: 176-190 [PMID: 26374575 DOI: 10.4103/2303-9027.162995]

41 **Kanagaraju V**, Rakshith AVB, Devanand B, Rajakumar R. Utility of Ultrasound Elastography to Differentiate Benign from Malignant Cervical Lymph Nodes. *J Med Ultrasound* 2020; **28**: 92-98 [PMID: 32874867 DOI: 10.4103/JMU.JMU_72_19]

42 **Özel D**, Özel BD. Evaluating the role of strain ratio elastography in determining malignancy potential and calculating objective BIRADS US scores using ultrasonography and elastography features. *Pol J Radiol* 2018; **83**: e268-e274 [PMID: 30627246 DOI: 10.5114/pjr.2018.76790]

43 **Shehata RMA**, El-Sharkawy MAM, Mahmoud OM. Qualitative and quantitative strain and shear wave elastography paradigm in differentiation of breast lesions. [cited 20 January 2022]. Available from: https://ejrnm.springeropen.com/articles/10.1186/s43055-022-00697-0

44 **Wang Z**, Yang T, Wu Z, Tang S, Liang X, Qin A, Ouyang T, Liu P, Liu J. Correlation between elastography score and strain rate ratio in breast small tumor. *Zhongnan Daxue Xuebao Yixueban* 2010; **35**: 928-932 [PMID: 20871156 DOI: 10.3969/j.issn.1672-7347.2010.09.005]

45 **Chu J**, Zhang Y, Zhang W, Zhao D, Xu J, Yu T, Yang G. The value of multimodal ultrasonography in differential diagnosis of tuberculous and non-tuberculous superficial lymphadenitis. *BMC Surg* 2021; **21**: 416 [PMID: 34906107 DOI: 10.1186/s12893-021-01418-6]

46 **Lammers T**, Aime S, Hennink WE, Storm G, Kiessling F. Theranostic nanomedicine. *Acc Chem Res* 2011; **44**: 1029-1038 [PMID: 21545096 DOI: 10.1021/ar200019c]

47 **Martin KH**, Dayton PA. Current status and prospects for microbubbles in ultrasound theranostics. *Wiley Interdiscip Rev Nanomed Nanobiotechnol* 2013; **5**: 329-345 [PMID: 23504911 DOI: 10.1002/wnan.1219]

48 **Ma J**, Martin K, Dayton PA, Jiang X. A preliminary engineering design of intravascular dual-frequency transducers for contrast-enhanced acoustic angiography and molecular imaging. *IEEE Trans Ultrason Ferroelectr Freq Control* 2014; **61**: 870-880 [PMID: 24801226 DOI: 10.1109/TUFFC.2014.6805699]

49 **Duran C**, Beltrán VP, González A, Gómez C, Riego JD. Contrast-enhanced Voiding Urosonography for Vesicoureteral Reflux Diagnosis in Children. *Radiographics* 2017; **37**: 1854-1869 [PMID: 29019761 DOI: 10.1148/rg.2017170024]

50 **Kiessling F**, Fokong S, Bzyl J, Lederle W, Palmowski M, Lammers T. Recent advances in molecular, multimodal and theranostic ultrasound imaging. *Adv Drug Deliv Rev* 2014; **72**: 15-27 [PMID: 24316070 DOI: 10.1016/j.addr.2013.11.013]

51 **Palmowski M**, Morgenstern B, Hauff P, Reinhardt M, Huppert J, Maurer M, Woenne EC, Doerk S, Ladewig G, Jenne JW, Delorme S, Grenacher L, Hallscheidt P, Kauffmann GW, Semmler W, Kiessling F. Pharmacodynamics of streptavidin-coated cyanoacrylate microbubbles designed for molecular ultrasound imaging. *Invest Radiol* 2008; **43**: 162-169 [PMID: 18301312 DOI: 10.1097/RLI.0b013e31815a251b]

52 **Fei C**, Chiu CT, Chen X, Chen Z, Ma J, Zhu B, Shung KK, Zhou Q. Ultrahigh Frequency (100 MHz-300 MHz) Ultrasonic Transducers for Optical Resolution Medical Imagining. *Sci Rep* 2016; **6**: 28360 [PMID: 27329379 DOI: 10.1038/srep28360]

53 **Willer K**, Fingerle AA, Gromann LB, De Marco F, Herzen J, Achterhold K, Gleich B, Muenzel D, Scherer K, Renz M, Renger B, Kopp F, Kriner F, Fischer F, Braun C, Auweter S, Hellbach K, Reiser MF, Schroeter T, Mohr J, Yaroshenko A, Maack HI, Pralow T, van der Heijden H, Proksa R, Koehler T, Wieberneit N, Rindt K, Rummeny EJ, Pfeiffer F, Noël PB. X-ray dark-field imaging of the human lung-A feasibility study on a deceased body. *PLoS One* 2018; **13**: e0204565 [PMID: 30261038 DOI: 10.1371/journal.pone.0204565]

54 **Bech M**, Tapfer A, Velroyen A, Yaroshenko A, Pauwels B, Hostens J, Bruyndonckx P, Sasov A, Pfeiffer F. In-vivo dark-field and phase-contrast x-ray imaging. *Sci Rep* 2013; **3**: 3209 [PMID: 24220606 DOI: 10.1038/srep03209]

55 **Schleede S**, Meinel FG, Bech M, Herzen J, Achterhold K, Potdevin G, Malecki A, Adam-Neumair S, Thieme SF, Bamberg F, Nikolaou K, Bohla A, Yildirim AÖ, Loewen R, Gifford M, Ruth R, Eickelberg O, Reiser M, Pfeiffer F. Emphysema diagnosis using X-ray dark-field imaging at a laser-driven compact synchrotron light source. *Proc Natl Acad Sci U S A* 2012; **109**: 17880-17885 [PMID: 23074250 DOI: 10.1073/pnas.1206684109]

56 **Bhalla AS**, Goyal A, Guleria R, Gupta AK. Chest tuberculosis: Radiological review and imaging recommendations. *Indian J Radiol Imaging* 2015; **25**: 213-225 [PMID: 26288514]

57 **Khan AU**, Khanduri S, Tarin Z, Abbas SZ, Husain M, Singh A, Yadav P, Jain S. Dual-Energy Computed Tomography Lung in patients of Pulmonary Tuberculosis. *J Clin Imaging Sci* 2020; **10**: 39 [PMID: 32754374 DOI: 10.25259/JCIS_78_2020]

58 **Huang HM**, Shih YY. Pushing CT and MR imaging to the molecular level for studying the "omics": current challenges and advancements. *Biomed Res Int* 2014; **2014**: 365812 [PMID: 24738056 DOI: 10.1155/2014/365812]

59 **Peprah KO**, Andronikou S, Goussard P. Characteristic magnetic resonance imaging low T2 signal intensity of necrotic lung parenchyma in children with pulmonary tuberculosis. *J Thorac Imaging* 2012; **27**: 171-174 [PMID: 21516045 DOI: 10.1097/RTI.0b013e318211abfb]

60 **Sodhi KS**, Khandelwal N, Saxena AK, Singh M, Agarwal R, Bhatia A, Lee EY. Rapid lung MRI in children with pulmonary infections: Time to change our diagnostic algorithms. *J Magn Reson Imaging* 2016; **43**: 1196-1206 [PMID: 26546472 DOI: 10.1002/jmri.25082]

61 **Bharati A**, Merchant S, Nagesh C. The 'Myocarditis-Pericarditis' Complex - A CMR Sign of Cardiac Tuberculosis and The Spectrum of imaging findings of Cardiac Tuberculosis on CMR. RSNA Annual Conference. Chicago: Radiological Society of North America, 2013. [cited 20 January 2022]. Available from: https://archive.rsna.org/2013/13012394.html

62 **Liu J**, Bai R, Li Y, Staedtke V, Zhang S, van Zijl PCM, Liu G. MRI detection of bacterial brain abscesses and monitoring of antibiotic treatment using bacCEST. *Magn Reson Med* 2018; **80**: 662-671 [PMID: 29577382 DOI: 10.1002/mrm.27180]

63 **Goldenberg JM**, Berthusen AJ, Cárdenas-Rodríguez J, Pagel MD. Differentiation of Myositis-Induced Models of Bacterial Infection and Inflammation with T_2-Weighted, CEST, and DCE-MRI. *Tomography* 2019; **5**: 283-291 [PMID: 31572789 DOI: 10.18383/j.tom.2019.00009]

64 **Campbell-Washburn AE**, Ramasawmy R, Restivo MC, Bhattacharya I, Basar B, Herzka DA, Hansen MS, Rogers T, Bandettini WP, McGuirt DR, Mancini C, Grodzki D, Schneider R, Majeed W, Bhat H, Xue H, Moss J, Malayeri AA, Jones EC, Koretsky AP, Kellman P, Chen MY, Lederman RJ, Balaban RS. Opportunities in Interventional and Diagnostic Imaging by Using High-Performance Low-Field-Strength MRI. *Radiology* 2019; **293**: 384-393 [PMID: 31573398 DOI: 10.1148/radiol.2019190452]

65 **Morales H**, Alfaro D, Martinot C, Fayed N, Gaskill-Shipley M. MR spectroscopy of intracranial tuberculomas: A singlet peak at 3.8 ppm as potential marker to differentiate them from malignant tumors. *Neuroradiol J* 2015; **28**: 294-302 [PMID: 26246099 DOI: 10.1177/1971400915592077]

66 **van Zijl PC**, Yadav NN. Chemical exchange saturation transfer (CEST): what is in a name and what isn't? *Magn Reson*

Med 2011; **65**: 927-948 [PMID: 21337419 DOI: 10.1002/mrm.22761]
67 **Minton LE**, Pandit R, Willoughby WR, Porter KK. The Future of Magnetic Resonance Imaging Contrast Agents. *Appl Radiol* 2022; **51**: 7-11 [cited 20 January 2022]. Available from: https://appliedradiology.com/articles/the-future-of-magnetic-resonance-imaging-contrast-agents
68 **Hancu I**, Dixon WT, Woods M, Vinogradov E, Sherry AD, Lenkinski RE. CEST and PARACEST MR contrast agents. *Acta Radiol* 2010; **51**: 910-923 [PMID: 20828299 DOI: 10.3109/02841851.2010.502126]
69 **Kulanthaivelu K**, Jabeen S, Saini J, Raju S, Nalini A, Sadashiva N, Hegde S, Rolla NK, Saha I, M N, Vengalil S, Swaroop S, Rao S. Amide proton transfer imaging for differentiation of tuberculomas from high-grade gliomas: Preliminary experience. *Neuroradiol J* 2021; **34**: 440-448 [PMID: 33823712 DOI: 10.1177/19714009211002766]
70 **Biswas A**, Santra S, Bishnu D, Dhali GK, Chowdhury A, Santra A. Isoniazid and Rifampicin Produce Hepatic Fibrosis through an Oxidative Stress-Dependent Mechanism. *Int J Hepatol* 2020; **2020**: 6987295 [PMID: 32373368 DOI: 10.1155/2020/6987295]
71 **Imajo K**, Honda Y, Kobayashi T, Nagai K, Ozaki A, Iwaki M, Kessoku T, Ogawa Y, Takahashi H, Saigusa Y, Yoneda M, Kirikoshi H, Utsunomiya D, Aishima S, Saito S, Nakajima A. Direct Comparison of US and MR Elastography for Staging Liver Fibrosis in Patients With Nonalcoholic Fatty Liver Disease. *Clin Gastroenterol Hepatol* 2022; **20**: 908-917.e11 [PMID: 33340780]
72 **Xu C**, Howey J, Ohorodnyk P, Roth M, Zhang H, Li S. Segmentation and quantification of infarction without contrast agents *via* spatiotemporal generative adversarial learning. *Med Image Anal* 2020; **59**: 101568 [PMID: 31622838 DOI: 10.1016/j.media.2019.101568]
73 **de Figueiredo EH**, Borgonovi AF, Doring TM. Basic concepts of MR imaging, diffusion MR imaging, and diffusion tensor imaging. *Magn Reson Imaging Clin N Am* 2011; **19**: 1-22 [PMID: 21129633 DOI: 10.1016/j.mric.2010.10.005]
74 **Jadvar H**, Colletti PM. Competitive advantage of PET/MRI. *Eur J Radiol* 2014; **83**: 84-94 [PMID: 23791129 DOI: 10.1016/j.ejrad.2013.05.028]
75 **Ordonez AA**, Sellmyer MA, Gowrishankar G, Ruiz-Bedoya CA, Tucker EW, Palestro CJ, Hammoud DA, Jain SK. Molecular imaging of bacterial infections: Overcoming the barriers to clinical translation. *Sci Transl Med* 2019; **11** [PMID: 31484790 DOI: 10.1126/scitranslmed.aax8251]
76 **Ordonez AA**, Weinstein EA, Bambarger LE, Saini V, Chang YS, DeMarco VP, Klunk MH, Urbanowski ME, Moulton KL, Murawski AM, Pokkali S, Kalinda AS, Jain SK. A Systematic Approach for Developing Bacteria-Specific Imaging Tracers. *J Nucl Med* 2017; **58**: 144-150 [PMID: 27635025 DOI: 10.2967/jnumed.116.181792]
77 **Sly LM**, Hingley-Wilson SM, Reiner NE, McMaster WR. Survival of Mycobacterium tuberculosis in host macrophages involves resistance to apoptosis dependent upon induction of antiapoptotic Bcl-2 family member Mcl-1. *J Immunol* 2003; **170**: 430-437 [PMID: 12496428 DOI: 10.4049/jimmunol.170.1.430]
78 **Chen RY**, Dodd LE, Lee M, Paripati P, Hammoud DA, Mountz JM, Jeon D, Zia N, Zahiri H, Coleman MT, Carroll MW, Lee JD, Jeong YJ, Herscovitch P, Lahouar S, Tartakovsky M, Rosenthal A, Somaiyya S, Lee S, Goldfeder LC, Cai Y, Via LE, Park SK, Cho SN, Barry CE 3rd. PET/CT imaging correlates with treatment outcome in patients with multidrug-resistant tuberculosis. *Sci Transl Med* 2014; **6**: 265ra166 [PMID: 25473034 DOI: 10.1126/scitranslmed.3009501]
79 **Davis SL**, Nuermberger EL, Um PK, Vidal C, Jedynak B, Pomper MG, Bishai WR, Jain SK. Noninvasive pulmonary [18F]-2-fluoro-deoxy-D-glucose positron emission tomography correlates with bactericidal activity of tuberculosis drug treatment. *Antimicrob Agents Chemother* 2009; **53**: 4879-4884 [PMID: 19738022 DOI: 10.1128/AAC.00789-09]
80 **Lin PL**, Maiello P, Gideon HP, Coleman MT, Cadena AM, Rodgers MA, Gregg R, O'Malley M, Tomko J, Fillmore D, Frye LJ, Rutledge T, DiFazio RM, Janssen C, Klein E, Andersen PL, Fortune SM, Flynn JL. PET CT Identifies Reactivation Risk in Cynomolgus Macaques with Latent M. tuberculosis. *PLoS Pathog* 2016; **12**: e1005739 [PMID: 27379816 DOI: 10.1371/journal.ppat.1005739]
81 **Esmail H**, Lai RP, Lesosky M, Wilkinson KA, Graham CM, Coussens AK, Oni T, Warwick JM, Said-Hartley Q, Koegelenberg CF, Walzl G, Flynn JL, Young DB, Barry Iii CE, O'Garra A, Wilkinson RJ. Characterization of progressive HIV-associated tuberculosis using 2-deoxy-2-[^{18}F]fluoro-D-glucose positron emission and computed tomography. *Nat Med* 2016; **22**: 1090-1093 [PMID: 27595321 DOI: 10.1038/nm.4161]
82 **Cherry SR**, Jones T, Karp JS, Qi J, Moses WW, Badawi RD. Total-Body PET: Maximizing Sensitivity to Create New Opportunities for Clinical Research and Patient Care. *J Nucl Med* 2018; **59**: 3-12 [PMID: 28935835 DOI: 10.2967/jnumed.116.184028]
83 **Jain SK**. The Promise of Molecular Imaging in the Study and Treatment of Infectious Diseases. *Mol Imaging Biol* 2017; **19**: 341-347 [PMID: 28155078 DOI: 10.1007/s11307-017-1055-0]
84 **Cherry SR**, Badawi RD, Karp JS, Moses WW, Price P, Jones T. Total-body imaging: Transforming the role of positron emission tomography. *Sci Transl Med* 2017; **9** [PMID: 28298419 DOI: 10.1126/scitranslmed.aaf6169]
85 **Badawi RD**, Shi H, Hu P, Chen S, Xu T, Price PM, Ding Y, Spencer BA, Nardo L, Liu W, Bao J, Jones T, Li H, Cherry SR. First Human Imaging Studies with the EXPLORER Total-Body PET Scanner. *J Nucl Med* 2019; **60**: 299-303 [PMID: 30733314 DOI: 10.2967/jnumed.119.226498]
86 **Lv Y**, Lv X, Liu W, Judenhofer MS, Zwingenberger A, Wisner E, Berg E, McKenney S, Leung E, Spencer BA, Cherry SR, Badawi RD. Mini EXPLORER II: a prototype high-sensitivity PET/CT scanner for companion animal whole body and human brain scanning. *Phys Med Biol* 2019; **64**: 075004 [PMID: 30620929 DOI: 10.1088/1361-6560/aafc6c]
87 **Foss CA**, Kulik L, Ordonez AA, Jain SK, Michael Holers V, Thurman JM, Pomper MG. SPECT/CT Imaging of Mycobacterium tuberculosis Infection with [^{125}I]anti-C3d mAb. *Mol Imaging Biol* 2019; **21**: 473-481 [PMID: 29998399 DOI: 10.1007/s11307-018-1228-5]
88 **Murooka TT**, Mempel TR. Multiphoton intravital microscopy to study lymphocyte motility in lymph nodes. *Methods Mol Biol* 2012; **757**: 247-257 [PMID: 21909917 DOI: 10.1007/978-1-61779-166-6_16]
89 **Blanc L**, Lenaerts A, Dartois V, Prideaux B. Visualization of Mycobacterial Biomarkers and Tuberculosis Drugs in Infected Tissue by MALDI-MS Imaging. *Anal Chem* 2018; **90**: 6275-6282 [PMID: 29668262 DOI: 10.1021/acs.analchem.8b00985]
90 **Niehaus M**, Soltwisch J, Belov ME, Dreisewerd K. Transmission-mode MALDI-2 mass spectrometry imaging of cells

and tissues at subcellular resolution. *Nat Methods* 2019; **16**: 925-931 [PMID: 31451764 DOI: 10.1038/s41592-019-0536-2]

91 **Paine MRL**, Ellis SR, Maloney D, Heeren RMA, Verhaert PDEM. Digestion-Free Analysis of Peptides from 30-year-old Formalin-Fixed, Paraffin-Embedded Tissue by Mass Spectrometry Imaging. *Anal Chem* 2018; **90**: 9272-9280 [PMID: 29975508 DOI: 10.1021/acs.analchem.8b01838]

92 **Casacio**, Catxere and Andrade. Quantum enhanced microscopy. A thesis submitted for the degree of Doctor of Philosophy - The University of Queensland, Australia, 2020. [cited 20 January 2022]. Available from: https://espace.library.uq.edu.au/

93 **Martineau AR**, Honecker FU, Wilkinson RJ, Griffiths CJ. Vitamin D in the treatment of pulmonary tuberculosis. *J Steroid Biochem Mol Biol* 2007; **103**: 793-798 [PMID: 17223549 DOI: 10.1016/j.jsbmb.2006.12.052]

94 **Nnoaham KE**, Clarke A. Low serum vitamin D levels and tuberculosis: a systematic review and meta-analysis. *Int J Epidemiol* 2008; **37**: 113-119 [PMID: 18245055 DOI: 10.1093/ije/dym247]

95 **Chung C**, Silwal P, Kim I, Modlin RL, Jo EK. Vitamin D-Cathelicidin Axis: at the Crossroads between Protective Immunity and Pathological Inflammation during Infection. *Immune Netw* 2020; **20**: e12 [PMID: 32395364 DOI: 10.4110/in.2020.20.e12]

96 **Arora VK**, Jaiswal AK. Vitamin D receptor polymorphism and active tuberculosis. [cited 20 January 2022]. Available from: http://tbassnindia.org/images/TB_October_2013_issue.pdf

97 **Coussens AK**, Wilkinson RJ, Hanifa Y, Nikolayevskyy V, Elkington PT, Islam K, Timms PM, Venton TR, Bothamley GH, Packe GE, Darmalingam M, Davidson RN, Milburn HJ, Baker LV, Barker RD, Mein CA, Bhaw-Rosun L, Nuamah R, Young DB, Drobniewski FA, Griffiths CJ, Martineau AR. Vitamin D accelerates resolution of inflammatory responses during tuberculosis treatment. *Proc Natl Acad Sci U S A* 2012; **109**: 15449-15454 [PMID: 22949664 DOI: 10.1073/pnas.1200072109]

98 **Sutaria N**, Liu CT, Chen TC. Vitamin D Status, Receptor Gene Polymorphisms, and Supplementation on Tuberculosis: A Systematic Review of Case-Control Studies and Randomized Controlled Trials. *J Clin Transl Endocrinol* 2014; **1**: 151-160 [PMID: 25599020 DOI: 10.1016/j.jcte.2014.08.001]

99 **Lips P**. Vitamin D deficiency and secondary hyperparathyroidism in the elderly: consequences for bone loss and fractures and therapeutic implications. *Endocr Rev* 2001; **22**: 477-501 [PMID: 11493580 DOI: 10.1210/edrv.22.4.0437]

100 **Junaid K**, Rehman A. Impact of vitamin D on infectious disease-tuberculosis-a Review. [cited 20 January 2022]. Available from: https://www.clinicalnutritionopenscience.com/article/S2352-9393(19)30017-X/pdf

101 **Davies PD**. The role of vitamin D in tuberculosis. *Am Rev Respir Dis* 1989; **139**: 1571 [PMID: 2729764 DOI: 10.1164/ajrccm/139.6.1571]

102 **Merchant S**, Bharati A, Merchant N. Tuberculosis of the genitourinary system-Urinary tract tuberculosis: Renal tuberculosis-Part I. *Indian J Radiol Imaging* 2013; **23**: 46-63 [PMID: 23986618 DOI: 10.4103/0971-3026.113615]

103 **Kathirvel M**, Mahadevan S. The role of epigenetics in tuberculosis infection. *Epigenomics* 2016; **8**: 537-549 [PMID: 27035266 DOI: 10.2217/epi.16.1]

104 **Gauba K**, Gupta S, Shekhawat J, Sharma P, Yadav D, Banerjee M. Immunomodulation by epigenome alterations in Mycobacterium tuberculosis infection. *Tuberculosis (Edinb)* 2021; **128**: 102077 [PMID: 33812175 DOI: 10.1016/j.tube.2021.102077]

105 **Wang M**, Kong W, He B, Li Z, Song H, Shi P, Wang J. Vitamin D and the promoter methylation of its metabolic pathway genes in association with the risk and prognosis of tuberculosis. *Clin Epigenetics* 2018; **10**: 118 [PMID: 30208925 DOI: 10.1186/s13148-018-0552-6]

106 **Tarashi S**, Badi SA, Moshiri A, Ebrahimzadeh N, Fateh A, Vaziri F, Aazami H, Siadat SD, Fuso A. The inter-talk between *Mycobacterium tuberculosis* and the epigenetic mechanisms. *Epigenomics* 2020; **12**: 455-469 [PMID: 32267165 DOI: 10.2217/epi-2019-0187]

107 **Faulkner V**, Cox AA, Goh S, van Bohemen A, Gibson AJ, Liebster O, Wren BW, Willcocks S, Kendall SL. Re-sensitization of *Mycobacterium smegmatis* to Rifampicin Using CRISPR Interference Demonstrates Its Utility for the Study of Non-essential Drug Resistance Traits. *Front Microbiol* 2020; **11**: 619427 [PMID: 33597931 DOI: 10.3389/fmicb.2020.619427]

108 **Lakhani P**, Sundaram B. Deep Learning at Chest Radiography: Automated Classification of Pulmonary Tuberculosis by Using Convolutional Neural Networks. *Radiology* 2017; **284**: 574-582 [PMID: 28436741 DOI: 10.1148/radiol.2017162326]

109 **Vonasek B**, Ness T, Takwoingi Y, Kay AW, van Wyk SS, Ouellette L, Marais BJ, Steingart KR, Mandalakas AM. Screening tests for active pulmonary tuberculosis in children. *Cochrane Database Syst Rev* 2021; **6**: CD013693 [PMID: 34180536 DOI: 10.1002/14651858.CD013693.pub2]

110 **Shivam A**. Edge Computing vs Cloud Computing: What are the Differences. [cited 20 January 2022]. Available from: https://www.simplilearn.com/edge-computing-vs-cloud-computing-article

111 **McMahan B**, Ramage D. Federated Learning: Collaborative Machine Learning without Centralized Training Data. Google AI Blog [Internet]. Google, 2017. Introducing an additional approach: Federated Learning. [cited 20 January 2022]. Available from: https://ai.googleblog.com/2017/04/federated-learning-collaborative.html

112 **Dean JG**, Ghemawat S. MapReduce: Simplified Data Processing on Large Clusters. Sixth Symposium on Operating System Design and Implementation. San Francisco: Google Inc, 2004. [cited 20 January 2022]. Available from: https://static.googleusercontent.com/media/research.google.com/en//archive/mapreduce-osdi04.pdf

113 **Ng D**, Lan X, Yao MM, Chan WP, Feng M. Federated learning: a collaborative effort to achieve better medical imaging models for individual sites that have small labelled datasets. *Quant Imaging Med Surg* 2021; **11**: 852-857 [PMID: 33532283 DOI: 10.21037/qims-20-595]

114 **Sheller MJ**, Edwards B, Reina GA, Martin J, Pati S, Kotrotsou A, Milchenko M, Xu W, Marcus D, Colen RR, Bakas S. Federated learning in medicine: facilitating multi-institutional collaborations without sharing patient data. *Sci Rep* 2020; **10**: 12598 [PMID: 32724046 DOI: 10.1038/s41598-020-69250-1]

115 **Navia-Vazquez A**, Vazquez-Lopez M, and Cid-Sueiro J. Double Confidential Federated Machine Learning Logistic

Regression for Industrial Data Platforms. In: 37th International Conference on Machine Learning Vienna 2020, Vienna. [cited 20 January 2022]. Available from: https://www.tsc.uc3m.es/~navia/FL-ICML2020/DCFML-FL_ICML2020-A_Navia_Vazquez_et_al.pdf

116 **Wikipedia**. Quantum Microsocpy. [cited 20 January 2022]. Available from: https://en.wikipedia.org/wiki/Quantum_microscopy

117 **Studio TB**. [cited 20 January 2022]. Available from: https://techcrunch.com/sponsor/qualcomm/the-future-is-not-the-internet-of-things-it-is-the-connected-intelligent-edge/

118 **Ono T**, Okamoto R, Takeuchi S. An entanglement-enhanced microscope. *Nat Commun* 2013; **4**: 2426 [PMID: 24026165]

119 **Optics**. org. Project QUILT reveals far-reaching potential of quantum optics and imaging. [cited 20 January 2022]. Available from: https://optics.org/news/13/1/4 (2022)

120 **Fraenhofer-Gesellschaft**. Quantum imaging: Pushing the boundaries of optics. [cited 20 January 2022]. Available from: https://phys.org/news/2022-01-quantum-imaging-boundaries-optics.html

121 **Shor PW**. Algorithms for quantum computation: discrete logarithms and factoring. In: Proceedings 35th Annual Symposium on Foundations of Computer Science 1994: 124-134 [cited 20 January 2022]. Available from: https://ieeexplore.ieee.org/document/365700

122 **Sharma M**. There's been another huge quantum computing breakthrough. [cited 20 January 2022]. Available from: https://www.mckinsey.com/business-functions/mckinsey-digital/our-insights/quantum-computing-use-cases-are-getting-real-what-you-need-to-know

123 **Tung L**. Quantum computing: Forget about qubits, here come qutrits. [cited 20 January 2022]. Available from: https://www.zdnet.com/article/quantum-computing-now-rigetti-explores-qutrits-as-well-as-qubits/

124 **Oikawa A**, Ota A. Quantum computing: Japan takes step toward light-based technology. [cited 20 January 2022]. Available from: https://asia.nikkei.com/Business/Technology/Quantum-computing-Japan-takes-step-toward-light-based-technology

125 **Kahn J**. Microsoft Quantum Algorithm Boosts Medical Imaging. [cited 20 January 2022]. Available from: https://fortune.com/2019/07/15/microsoft-quantum-algorithm-boosts-medical-imaging

126 **Charles Q**, Choi AI. Fuses With Quantum Computing in Promising New Memristor Quantum device points the way toward an exponential boost in "smart" computing capabilities. [cited 20 January 2022]. Available from: https://spectrum.ieee.org/quantum-memristor

127 **Spagnolo M**, Morris J, Piacentini S. Experimental photonic quantum memristor. *Nature Photonics* 2022; **16**: 318-323 [cited 20 January 2022]. Available from: https://www.nature.com/articles/s41566

World Journal of Radiology

Submit a Manuscript: https://www.f6publishing.com

World J Radiol 2022 June 28; 14(6): 137-150

DOI: 10.4329/wjr.v14.i6.137

ISSN 1949-8470 (online)

MINIREVIEWS

Recent advances in imaging techniques of renal masses

Ankita Aggarwal, Chandan J Das, Sanjay Sharma

Specialty type: Radiology, nuclear medicine and medical imaging

Provenance and peer review: Invited article; Externally peer reviewed.

Peer-review model: Single blind

Peer-review report's scientific quality classification

Grade A (Excellent): 0
Grade B (Very good): 0
Grade C (Good): C
Grade D (Fair): D
Grade E (Poor): 0

P-Reviewer: Quartuccio N, Italy; Yang L, China
A-Editor: Liu X, China

Received: December 21, 2021
Peer-review started: December 21, 2021
First decision: February 21, 2022
Revised: March 4, 2022
Accepted: June 16, 2022
Article in press: June 16, 2022
Published online: June 28, 2022

Ankita Aggarwal, Department of Radiology, Vardhman Mahavir Medical College& Safdarjung Hospital, Delhi 110029, India

Chandan J Das, Department of Radiodiagnosis and Interventional Radiology, All India Institute of Medical Sciences, Delhi 110029, India

Sanjay Sharma, Department of Radiology (RPC), All India Institute of Medical Sciences, New Delhi 110029, India

Corresponding author: Chandan J Das, MD, Additional Professor, Department of Radiodiagnosis and Interventional Radiology, All India Institute of Medical Sciences, Ansari Nagar, Delhi, Delhi 110029, India. dascj@yahoo.com

Abstract

Multiphasic multidetector computed tomography (CT) forms the mainstay for the characterization of renal masses whereas magnetic resonance imaging (MRI) acts as a problem-solving tool in some cases. However, a few of the renal masses remain indeterminate even after evaluation by conventional imaging methods. To overcome the deficiency in current imaging techniques, advanced imaging methods have been devised and are being tested. This review will cover the role of contrast-enhanced ultrasonography, shear wave elastography, dual-energy CT, perfusion CT, MR perfusion, diffusion-weighted MRI, blood oxygen level-dependent MRI, MR spectroscopy, positron emission tomography (PET)/prostate-specific membrane antigen-PET in the characterization of renal masses.

Key Words: Advanced imaging techniques; Renal mass; Contrast-enhanced ultrasonography renal; Shear wave elastography

Core Tip: To overcome the deficiency in the existing imaging techniques for adequate characterization of renal masses, newer/advanced imaging methods have been devised and are being tested. This review will cover contrast-enhanced ultrasonography, shear wave elastography, dual-energy computed tomography (CT), perfusion CT, diffusion-weighted magnetic resonance imaging (MRI), MR perfusion, blood oxygen level-dependent MRI, MR spectroscopy, and positron emission tomography (PET)/prostate-specific membrane antigen-PET.

Citation: Aggarwal A, Das CJ, Sharma S. Recent advances in imaging techniques of renal masses. *World J Radiol* 2022; 14(6): 137-150
URL: https://www.wjgnet.com/1949-8470/full/v14/i6/137.htm
DOI: https://dx.doi.org/10.4329/wjr.v14.i6.137

INTRODUCTION

Precise characterization of any renal mass is of paramount importance for clinicians to decide the most appropriate treatment and thereby improve the survival outcome. Being safe, cost-effective, and non-invasive, ultrasound is the current screening modality for the evaluation of renal masses for malignancy with a sensitivity of 82%-83% and specificity of 98%-99%[1-3]. However, the sensitivity is low for masses less than 3cm in size[4]. Multidetector computed tomography (MDCT) forms the mainstay for diagnosis and is the imaging modality of choice for characterization of renal masses[5]. In this technique, a non-contrast scan is performed, followed by a corticomedullary phase at 25-70 s, a nephrographic phase at 80-180 s, and an excretory phase at 4-8 min[5]. A non-contrast scan is essential to detect any hemorrhage or calcification within the mass. Identification of pseudotumor is best done in the corticomedullary phase. A nephrographic phase is ideal for the detection of renal tumors. An excretory phase is acquired to detect pelvicalyceal system involvement. Conventional and dynamic contrast-enhanced magnetic resonance imaging (MRI) serves as a problem-solving tool[6]. MRI can also be done in cases when contrast-enhanced computed tomography (CT) is contraindicated.

Current imaging methods for the evaluation of renal tumors suffer from a few major drawbacks. As multiphasic MDCT involves the acquisition of multiple scans at different time intervals for the characterization of renal tumors, the risk of radiation is high with this repeated and multiple scanning. Contrast administered for CT or MRI can lead to various allergic reactions as well as impairment of renal function. Even after all these investigations, no conclusive diagnosis can be established in a few lesions like Bosniak 3 lesions and indeterminate renal masses. Masses like oncocytoma or lipopenic angiomyolipoma cannot be confidently diagnosed as they have no specific imaging criterion. Ruling out malignancy in pseudolesions at times becomes difficult. Focal pyelonephritis and evolving or resolving abscess may sometimes simulate malignancy; hence, more advanced imaging techniques are required for a definitive answer as the management would significantly differ in these groups.

To overcome the deficiency in imaging techniques, newer/advanced imaging methods have been devised and are being tested. This review will cover contrast-enhanced ultrasonography (CEUS), shear wave elastography (SWE), dual-energy CT (DECT), CT perfusion, MR perfusion, diffusion-weighted MRI, blood oxygen level-dependent (BOLD) MRI, MR spectroscopy (MRS), and positron emission tomography (PET)/prostate-specific membrane antigen (PSMA)-PET.

ADVANCED IMAGING TECHNIQUES

Contrast-enhanced ultrasound

CEUS has recently gained popularity in the last decade as it has become a problem-solving tool in many areas including renal diseases. The European Federation of Societies for Ultrasound in Medicine and Biology (EFSUMB) has incorporated renal applications of CEUS in 2012[7] and updated the recommendations in a paper published in 2017[8]. Being safe and quick, it has augmented the sensitivity and specificity of ultrasound in the characterization of renal masses. It can fairly differentiate small isoechoic or small solid lesions, better characterize complex cystic lesions, and differentiate tumors *vs* pseudotumors and renal cell carcinoma (RCC) *vs* angiomyolipoma, and can be utilized for detection and follow-up of renal infections.

Ultrasound contrast agents (USCA) are made up of microbubbles surrounded by a shell. This shell is composed of lipid, protein, or polymer. As these microbubbles are very fragile, the shell provides them with stability[9]. Two principles play a role in CEUS, one is enhancing the echogenicity of the lesion that is imaged and the other is the suppression of the background signal. Contrast agents markedly increase the backscatter due to a large difference in acoustic impedance at gas fluid/tissue surface interface. The second effect of background suppression is achieved by a technique called pulse inversion. For this, two similar signals with opposite phases which are mirror images of each other are sent through the same scan line and echoes from both are collected and added by the transducer. Normal tissues which act like linear reflectors produce no net signal due to the cancellation of echoes whereas the ones having microbubbles act like non-linear reflectors that produce some net signal which stands out against a dark background. When ultrasound waves strike these molecules (tissues with microbubbles), they strongly backscatter and increase the echoes by a factor of 500-1000, thus resulting in enhancement. Microvascular flow rate can also be calculated by calculating the rate at which microbubbles are in the imaging plane.

USCA evaluates both the macrovascular and microvascular systems. As soon as the contrast agent is injected, there is an avid and rapid enhancement of the kidney. Initially, the main renal artery and its branches are enhanced, followed by segmental, interlobular, arcuate, and intralobular branches. This is followed by enhancement of the cortex, then the outer medulla, and finally the pyramids. Only two phases are seen, cortical from 15 to 30s and parenchymal from 25 s to 4 min[10]. The point to note is that there will be no excretory phase as the contrast agents are not excreted in the kidneys, thus allowing it to use safely in patients with deranged renal function[8]. Current applications of CEUS in renal mass is as follows.

Differentiating renal tumors from pseudolesions: B-mode ultrasound and Doppler ultrasound fail to differentiate the solid renal tumors from pseudolesions. CEUS can make an apt and confident differential between the two, especially in patients with chronic kidney disease (CKD). Pseudolesions will show the same enhancement pattern as the normal renal parenchyma, whereas renal tumors will show different enhancement patterns in at least one of the phases[11]. In 5% of the cases when the tumor is isoenhancing, renal vascular anatomy should be studied in the early arterial phase which will show normal arteries passing through pseudolesions and aberrant deviation of arteries by the renal tumor[8].

Evaluation of renal cystic lesions: Several studies have shown CEUS to be better than CT in detecting any solid component, septa, and thickening in the wall within the cystic renal mass and thus can classify it according to Bosniak classification[12-16](Figure 1). Follow-up of complex renal cysts can be easily and quickly done by CEUS instead of expensive and high radiation exposure modalities like CT.

Characterization of indeterminate renal tumors: CEUS proves useful in determining even minimal vascularity in hypovascularized tumors to differentiate complex renal lesions from solid mass, which are indeterminate on cross-sectional imaging[12,17,18]. This is especially advantageous in CKD patients where both complex cysts and tumors have a high incidence[19].

Renal vein invasion: Renal vein invasion by tumor thrombus can be reliably detected by CEUS in which an enhancing thrombus can be seen within the renal vein and a diagnosis of malignancy can thus be confidently made[20].

Renal infections: Early detection of renal abscesses in a case of acute pyelonephritis can be done by CEUS which shows avascular areas in renal parenchyma in the parenchymal phase. Also, follow-up can be done by CEUS to look for progression or resolution of the disease[21].

The major advantages of CEUS are that it is extremely safe with no radiation exposure and can be done in CKD or patients with contrast allergy. It is quick and inexpensive. Major limitations are its operator dependence and poor visualization at times due to bowel gas or ribs.

SWE

SWE is a quantitative elastography technique that evaluates the stiffness of the tissue. The EFSUMB laid down guidelines and recommendations for its use in non-hepatic areas in the year 2013 and has updated it in 2018[8]. In the kidney, its use is limited to assess stiffness in CKD or transplant cases. The EFSUMB recommends its use as an additional tool for the diagnosis of chronic allograft nephropathy and does not recommend its use in native kidneys[8] as they are deep-seated and beyond 40mm depth which is usually the depth of the region of interest (ROI) box at which measurements are done. Only a few studies are available which have tried to differentiate benign from malignant renal masses based on their stiffness[22].

Shear wave propagation speed in tissues varies depending upon the tissue stiffness. Acoustic radiation force impulse transmits longitudinal forces which result in deformation of the tissue and generation of transverse waves called the shear waves. These are then captured by the transducer and their propagation speed is calculated. A color-coded, real-time SWE map is generated which shows local tissue stiffness in kilopascals (quantitative assessment). ROI is selected and values for maximum, minimum, mean stiffness, and standard deviation are produced. Less than ten studies have been published which have tried to differentiate benign from malignant renal mass based on elasticity. Amongst these, several have done strain elastography[23,24] and several shear wave elastography[22,25]. No standardized values have been obtained yet. One of the studies postulates elasticity values in the range of 4.5-4.7 ± 1.5-1.7 kPa of the normal renal cortex[22]. A study by Aydin *et al*[25] evaluated 40 renal masses and found the highest elasticity value in the malignant and benign groups to be 27.27 ± 25.66 kPa and 16.13 ± 8.89 kPa, respectively. However, more studies with a larger number of patients are required to authenticate these findings and establish a nomogram and cut-off for elasticity values of benign and malignant lesions. Figure 2 depicts a case of RCC having greater stiffness as compared to normal renal parenchyma.

This is a rapid, non-invasive, radiation-free, repeatable, and inexpensive technique that has no major side effects[22]. The only caution is advised in sensitive areas and fetuses as it can increase local temperature like Doppler ultrasound.

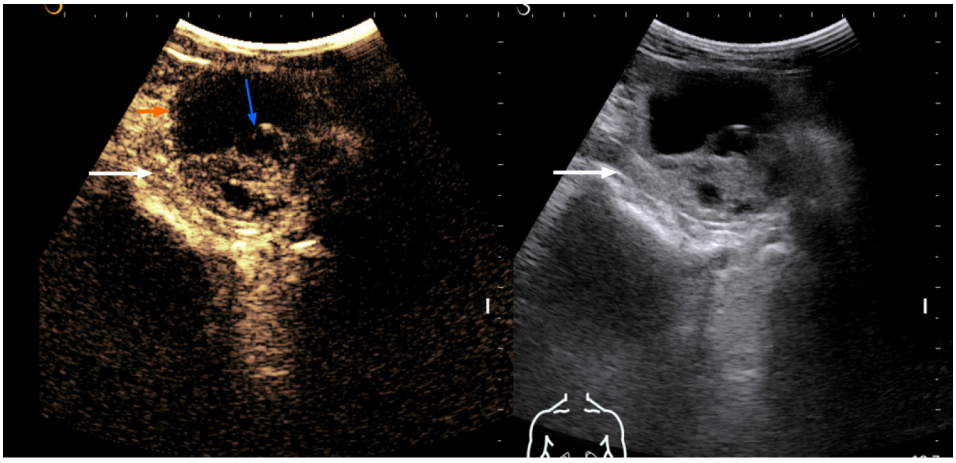

DOI: 10.4329/wjr.v14.i6.137

Figure 1 Contrast-enhanced ultrasonography images of a solid-cystic lesion in the left kidney showing thick nodular septal enhancement (blue arrow) and enhancement of solid component (long arrow). Consistent with Bosniak category 4 lesion/malignant lesion. The lesion was resected and histology revealed clear cell renal cell carcinoma.

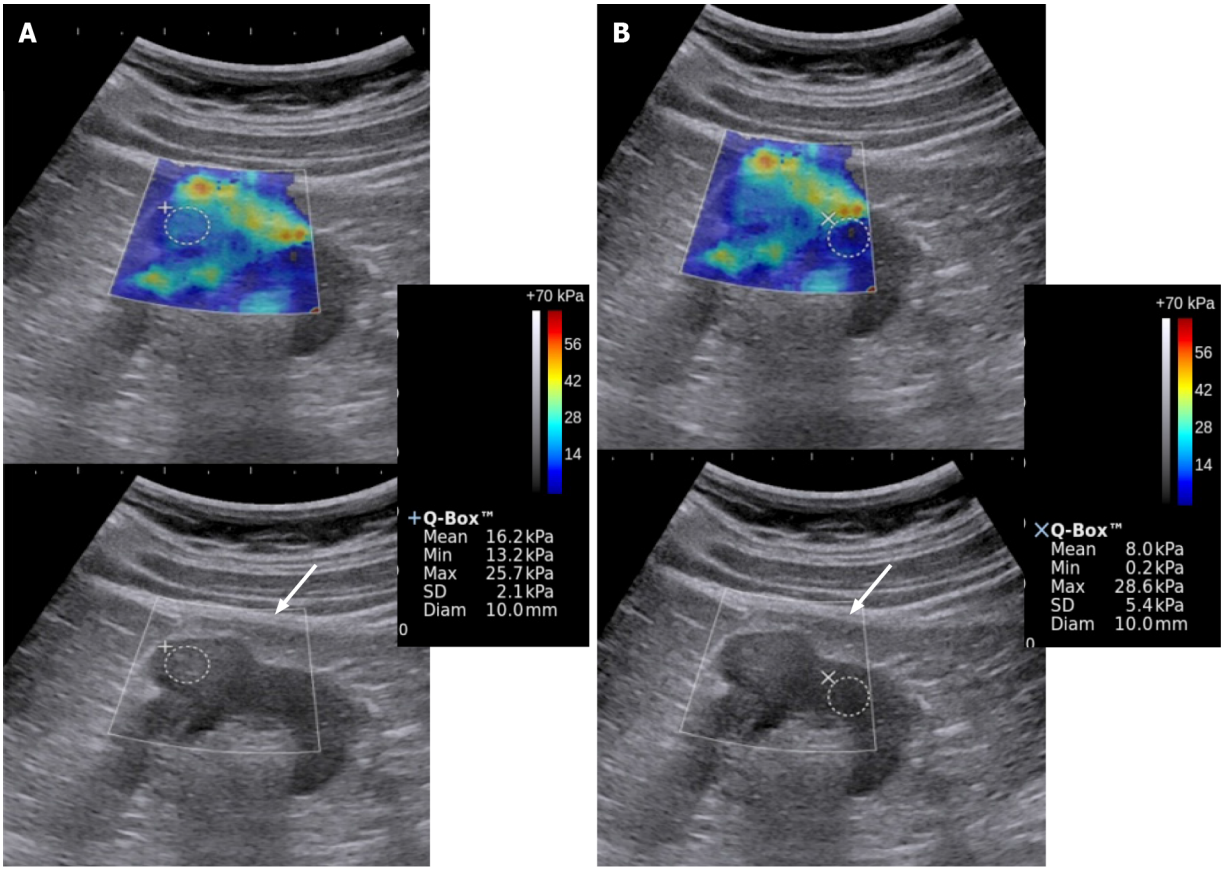

DOI: 10.4329/wjr.v14.i6.137

Figure 2 Elastography & gray-scale images of the renal mass (A) and the normal kidney (B). The mass showed greater stiffness relative to the surrounding kidney. Biopsy showed high-grade renal cell carcinoma.

DECT

DECT works on the principle of differences in absorption of photons at different photon energies which also varies with differences in material composition. Dual energy is produced either by two tubes with different peak voltages (dual-source scanner) or using a single tube with alternating peak voltage (single source)[26]. Atoms with large atomic number, like iodine, shows attenuation differences at two different peak voltages. Post-processing software is available which can subtract iodine from all images, resulting in the generation of virtual non-contrast images. Iodine overly maps can be generated which can

precisely determine areas of iodine uptake[27]. Hence, many masses which are termed indeterminate on CECT of the abdomen can be classified based on iodine uptake.

Non-contrast scans are not routinely included in abdominal CT protocol[26]. As most of the renal masses are incidentally detected, it becomes very difficult at times to detect post-contrast enhancement, hence many times the masses are labeled as indeterminate and advised for further imaging, either by multiphasic CT or MRI. If DECT is routinely done, virtual non-contrast scans can be generated and any iodine uptake can be confidently identified[28]. This will preclude the need for additional scans, thereby resulting in radiation dose reduction. Also, the cost and time of doing additional investigations can be markedly cut down.

Iodine quantification can also be done with iodine maps generated by DECT, which is given in milligram/milliliter (mg/mL). This is an indirect measure of the vascularity of the region of interest. Several studies have shown values greater than 0.5 mg/mL in tissue are indicative of enhancement[29,30]. Measurement of iodine concentration within a lesion (instead of attenuation value) solves the problem of pseudo enhancement of cysts and differentiating hyperdense cysts from hypovascular tumours[31] (Figure 3). Obtaining iodine levels from a single ROI is another advantage as it avoids the error of keeping ROI in multiple scans which can vary in position due to respiration or motion artifact [32]. Also, when the mass is large and heterogeneous, fallacious attenuation values can come if a hemorrhagic or necrotic component is included within the ROI. Measuring net total iodine concentration will not vary if such areas get included in the ROI. Hence, a large ROI covering the entire mass can be kept[33]. According to a systematic analysis and meta-analysis by Salameh, the pooled sensitivity and specificity of DECT were to be 96.6% and 95.1%, respectively, in renal masses using quantitative iodine concentration[34].

CT perfusion

CT perfusion imaging detects the temporal changes in tissue attenuation after iodinated contrast is administered intravenously. It can detect changes at the molecular level and assess tissue perfusion and vascular permeability. Both qualitative and quantitative measurements can be done. Blood flow (BF) and blood volume (BV) can be obtained from the initial intravascular phase and vascular permeability (PMB) from the second phase.

Perfusion studies are an indirect predictor of neoangiogenesis. In renal cell carcinoma, which is a highly vascular tumor, multiple factors like vascular endothelial growth factor and tyrosine kinase are recruited, which result in neoangiogenesis. This neoangiogenesis is responsible for the growth of the tumor and metastasis. Targeted chemotherapy stops the proliferation of new vessels and reduces the perfusion parameters; hence, the response to treatment can be assessed. As the size of the mass decreases much later than the reduction in vascular parameters, early response evaluation is possible with perfusion technique[35] (Figures 4 and 5).

MR perfusion

MR perfusion is the technique developed to measure perfusion or vascularity of tissue after injection of a contrast medium. Multiphasic MRI is routinely done to assess the enhancement of the tissue. However, quantitative parameters can be derived only with MR perfusion. In this signal intensity, curves are generated which are placed against time and many post-processing techniques are done to obtain perfusion parameters[36]. Tissue perfusion can also be measured without administering a contrast medium through arterial spin labeling technique[37-40]. In this technique, the red blood cells (RBCs) behave as endogenous contrast agents. They are labeled non-invasively with MR gradient and radiofrequency. Tissue perfusion is calculated by estimating the inflow of the labeled RBCs to the tissue of interest. The major advantage of non-contrast MR perfusion is as endogenous contrast is used, erroneous calculation due to vascular permeability is not problematic here. Second, it can be done in patients where MR contrast medium is contraindicated. But it has a low sensitivity in hypovascular masses.

Tumor grading of RCC is also possible by perfusion studies. Higher grade RCC shows higher perfusion values than low-grade RCC. One of the studies by Palmowski obtained mean perfusion values of high-grade RCC to be 1.59 ± 0.44 (mL/g/min) *vs* low-grade RCC 1.08 ± 0.38 (mL/g/min)[41]. Another advantage of MR perfusion is in the evaluation of antiangiogenic drug therapy commonly administered for metastatic RCC. Changes in vascularity occur much before the change in the size of the mass. Hence, for early response assessment, several studies[42-44] have demonstrated the potential role of this technique.

Diffusion-weighted imaging

Diffusion-weighted imaging (DWI) is a type of functional MR technique that quantitatively assesses the free Brownian motion of water molecules and thus derives the image contrast based on the restriction of this free motion. This in turn is dependent on the tissue cellularity, organization, cell membrane integrity, and extracellular space tortuosity[45,46]. Abundant work is available in establishing its usefulness in the central nervous system. Many studies have also come forth evaluating its role in the kidneys in the last two decades. DWI has shown promise in differentiating benign *vs* malignant renal

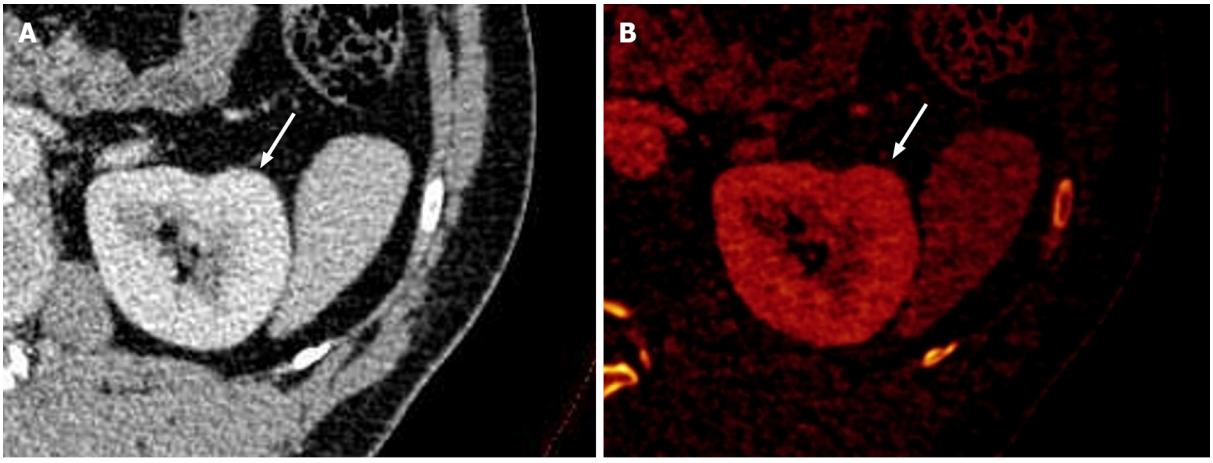

DOI: 10.4329/wjr.v14.i6.137

Figure 3 Dual-energy computed tomography images. A: Contrast-enhanced axial dual-energy computed tomography image showing contour bulge from the lateral cortex of the interpolar region of the left kidney, enhanced similar to background parenchyma; B: Iodine overlay image confirming the absence of any differential iodine distribution, suggesting the lesion to be a dromedary hump.

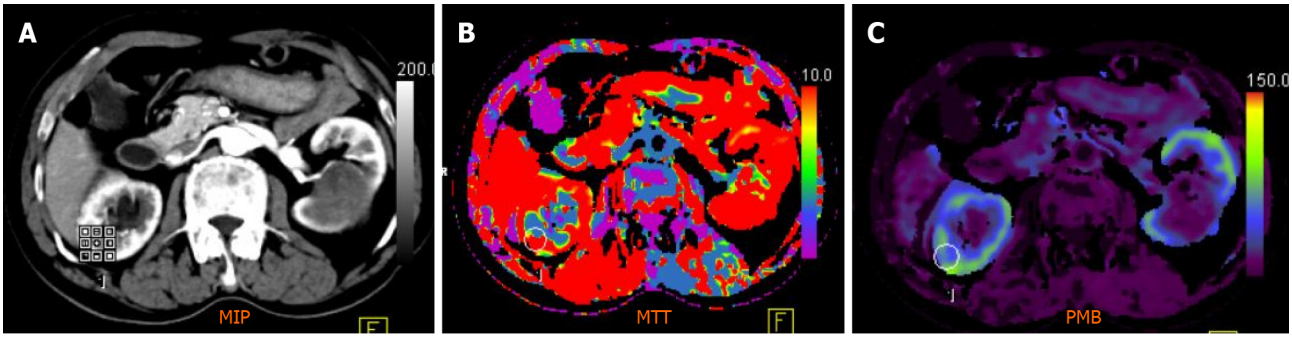

DOI: 10.4329/wjr.v14.i6.137

Figure 4 Computed tomography perfusion images (A-C) reveal a significant difference in permeability and mean transit time values between normal renal cortex and malignant lesions. Mean transit time (MTT) and permeability (PMB) in normal renal cortex were 10.48 s and 55.56 mL/100 mL/min, respectively, which were significantly different from those of renal cell carcinoma (RCC) (MTT: 9.06 s; PMB: 237.09 mL/100 mL/min). A cut-off of 2.5 mL/100 g/min yielded a 100% sensitivity and 95.92% accuracy to predict RCC.

lesions, in differentiating clear *vs* non-clear cell carcinoma, and in further subtyping the grade of RCCs [47-53].

Benign masses show higher apparent diffusion coefficient (ADC) than malignant lesions. According to a study by Sandrasegaran *et al*[53], the mean ADC of benign lesions is [mean (Standard deviation) 2.76 (0.32) × 10^{-3} mm^2/s] *vs* malignant lesions [2.02 × 10^{-3} mm^2/s]. Amongst the malignant masses, clear cell RCCs show signi-ficantly higher ADC values than papillary and chromophobe RCCs, which have a better prognosis than clear cell RCCs. Low-grade clear cell RCCs have significantly higher ADC values than high-grade RCC, *i.e.*, an inverse relation is seen, the higher the grade, the lower the ADC[46]. According to a study by Agnello *et al*[54], mean ADC was significantly different between RCC (1.2 ± 0.01 mm^2/s), angiomyolipoma(1.07 ± 0.3 mm^2/s), metastases (1.25 ± 0.04 mm^2/s), and oncocytomas (1.56 ± 0.08 mm^2/s; $P < 0.05$).

DWI is particularly helpful in patients with contrast allergy or renal impairment when the iodinated control is contraindicated. In such situations, diffusion enhances the confidence of making the distinction between benign and malignant masses on a plain scan.

As the treatment of focal renal lesions could be variable ranging from ablative procedures to complete or partial nephrectomy and radiological follow-up to chemotherapy depending upon the aggressiveness of the lesion, clear demarcation and characterization of renal mass are of utmost importance, which can be optimally done by DWI. Besides, diffusion is also done in renal parenchymal disease and renal infections. It is especially helpful in assessing the response to treatment and in follow-up scans to look for any recurrence (Figure 6). In postoperative scans due to marked post-operative/chemo inflammatory changes, it is hard to detect early recurrence in plain scans.

The main advantage of this sequence is that it is a quick sequence without much extending the total span of MRI examination and hence has been routinely incorporated in standard abdominal MRI. No

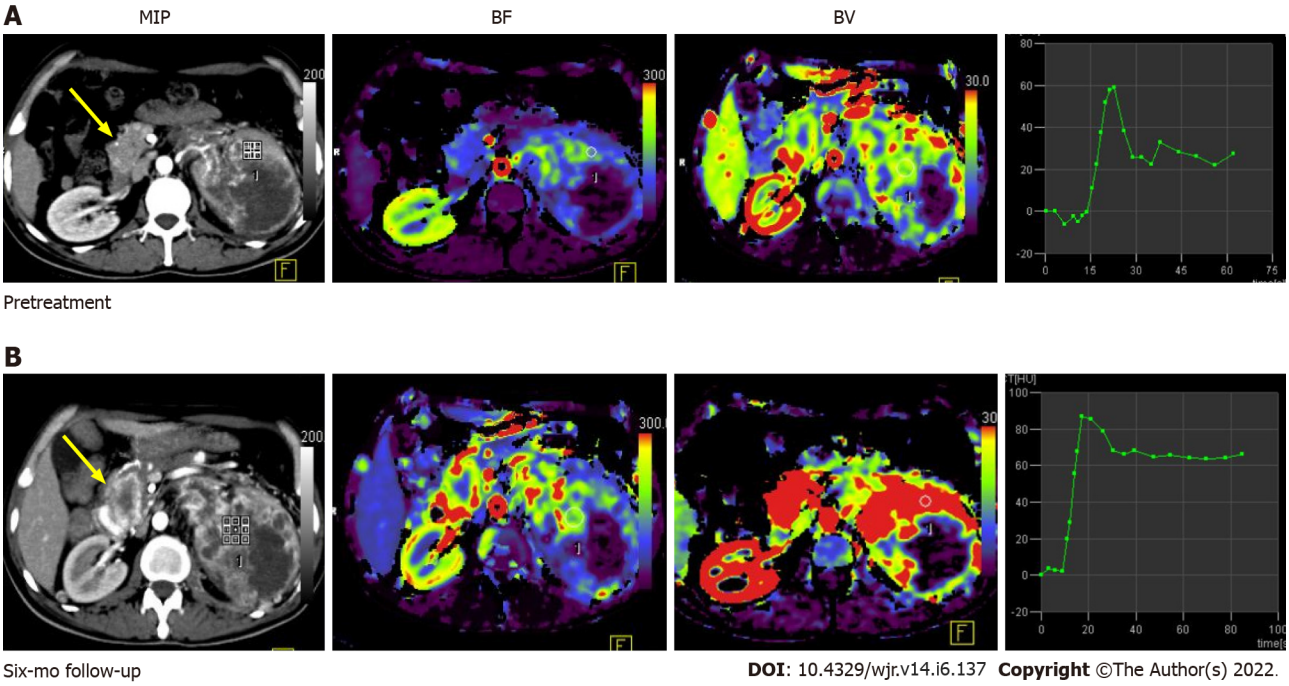

DOI: 10.4329/wjr.v14.i6.137

Figure 5 Pre-treatment (A) and post-treatment (B) computed tomography perfusion images in a case of large left renal cell carcinoma with metastasis to the uncinate process of the pancreas (yellow arrow). Comparison of perfusion parameters at the 6-mo follow-up after anti-angiogenic therapy showed that there was an increase in BF and BV, which was suggestive of progressive disease. No significant change in lesion size would have qualified this case as a stable disease as per size criteria.

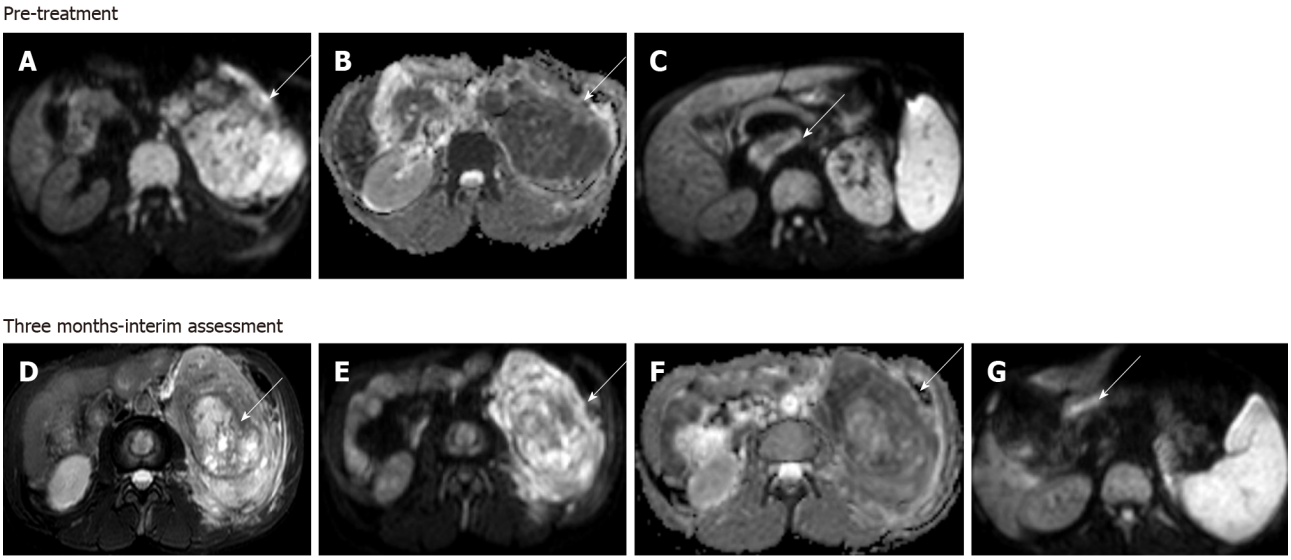

DOI: 10.4329/wjr.v14.i6.137

Figure 6 Magnetic resonance images. Diffusion-weighted imaging (DWI) at b = 800 s/mm^2 (A) and apparent diffusion coefficient (ADC) map (B) showed large clear cell renal cell carcinoma replacing the left kidney showing markedly restricted diffusion; DWI image (C) showing a malignant thrombus extending to the inferior vena cava (arrow) Axial T2W FS image (D) showing that 3 mo after treatment with sorafenib (a tyrosine kinase inhibitor), there was no significant change in the size of the lesion; however, there was increased necrosis in the mass; Resultant increase in ADC value on the corresponding DWI at b = 800 s/mm^2 (E) and ADC map (F); DWI (G) also revealed partial recanalization of the malignant thrombus (arrow)—overall features suggestive of partial response.

contrast administration is required. It is quite specific and has proved more specific when evaluated along with basic MRI than CT or MRI alone. However, caution needs to be taken with regard to the area from which the values are calculated. If ROI is kept over the hemorrhagic or necrotic component of the mass, the values can be misleading. The scanner needs to be optimized and appropriate b values (400-800) should be used to improve the accuracy of results.

Many researchers are showing interest in evaluating the role of intravoxel incoherent motion (IVIM) and diffusion kurtosis in differentiating benign from malignant renal masses and also in the grading of

renal cell carcinoma. IVIM is a biexponential model which includes both true and pseudo diffusion, which is predominantly driven by perfusion[55]. Parameters like diffusivity (D), pseudo diffusion coefficient (D*), and perfusion index (F) can be calculated. Jenson *et al*[56] in the year 2005 gave the concept of diffusion kurtosis which follows non-Gaussian diffusion, and parameters like mean diffusivity, mean kurtosis, kurtosis anisotropy, and radial kurtosis can be measured. A significant difference in Diffusion kurtosis parameters is seen in different subtypes and grades of RCC. A study by Ding *et al*[57] obtained superior results with IVIM in differentiating benign from malignant renal masses than diffusion or kurtosis parameters.

BOLD

BOLD is a quick MRI sequence that non-invasively evaluates deoxyhemoglobin levels in the kidney. In most human organs, oxygen tension is relatively constant and varies with the regional blood flow. The kidney is one of the organs where the oxygen tension varies both with the blood flow and the need for filtration. As tubular filtration is an active process requiring energy, this results in a variation of oxygen tension. The cortex of the kidney is well perfused and high in oxygen whereas the medulla is relatively less perfused with and low in oxygen tension. The medulla also has a counter-current arrangement of vessels which further contributes to lower oxygen tension in this region. This results in higher production of deoxyhemoglobin. Deoxyhaemoglobin has a paramagnetic effect and results in the rapid dephasing of protons. A higher amount of deoxyhemoglobin leads to a decrease in T2* relaxation time [58].

BOLD MRI has wide applications in the brain[59-62]. Many studies are being done on the kidneys, justifying their utility in renal pathologies. The echo-planar imaging (EPI) sequence or more sequences are used. The multiple gradient-recalled echo sequence is better than the EPI sequence in terms of SNI, spatial distortion, and spatial resolution. It calculates 1/R2* and generates various maps. After the excitation pulse, multiple gradient echoes are acquired. The higher the strength of the magnetic field, the better the results obtained. BOLD MRI proves useful in the detection of ischemia in the kidneys as in renal artery stenosis, renal artery occlusion, *etc*. as proven by a few studies[63-65]. Early initiation of treatment results in a better outcome. It is also useful in diabetics, hypertension, allograft rejection, *etc.* As various renal lesions would result in a change in perfusion of the kidney, this can be a reliable tool to differentiate benign from malignant renal lesion (Figures 7 and 8).

Proton spectroscopy

Proton spectroscopy (H1MRS) is an advanced MR technique that studies the variation in chemical metabolites in determining various pathologies. It is a powerful, non-invasive tool to quantitatively study the chemical compositions and metabolic processes *in vivo*.

Whenever there is an application of magnetic field, there is a generation of small magnetic fields by the circulating protons which interact with the main magnetic field and bring about a change in Larmor frequency. This change in frequency due to differing chemical composition is called "chemical shift [66]". Proctor and Yu, for the first time, proposed the concept of chemical shift in 1951, and the first *in vivo* proton MR spectrum was published in 1985[67].

Proton MR spectroscopy has well-known applications in the central nervous system, breast, and prostate. Its role in renal masses is the current area of interest. Promising results of a few *in vitro* and *in vivo* studies are available in the differentiation of different renal masses[68].

The first *in vivo* study was conducted by Kim *et al*[69] who recruited five patients with biopsy-proven cases of RCC and found the difference of metabolite lipid and choline as per the grade of the tumour (Figure 9).

MRS is limited by the complexity of its acquisition, processing, and data interpretation[70]. It suffers from a low sensitivity and poor spatial resolution. It can only act as a complementary tool that supplements the results of basic MRI examination.

PET scan: Fluorodeoxyglucose and PSMA PET

Fluorodeoxyglucose (FDG) PET scan plays a limited role in primary RCC due to low sensitivity[71] but can be useful in case of aggressive or advanced RCC[72], recurrent disease[73], and metastatic RCC[74], and for post-treatment evaluation[75]. As FDG is excreted by the kidneys, FDG PET is not suitable for local staging of primary RCC. However, it has a crucial role in overall staging of the disease, differentiating malignant *vs* bland thrombosis in the renal vein/inferior vena cava, detecting metastasis to distant sites, detecting recurrent/residual disease in postoperative/chemotherapy evaluation, monitoring response to therapy, and restaging of the disease. Quantitative measurement of maximum standardized uptake values(SUVs) can be done for objective assessment. The higher the SUV, the more dismal the prognosis. A cut-off of 3 is seen to be optimal to differentiate low grade *vs* high-grade RCC [75].

Although FDG is the most common tracer to be used for PET, other new tracers like ^{68}Ga-PSMA, ^{18}F-fluoroethylcholine, ^{11}C-acetate, ^{18}F-fluoromisonidazole, and ^{18}F-fluorothymidine are being investigated [76]. Prostate-specific membrane antigen (PSMA) is a molecule that is expressed in prostatic cells and has established application in the prostatic tumor. Further research showed its expression on neovasculature of renal cancer cells and hence its potential role in RCC has been explored by researchers with

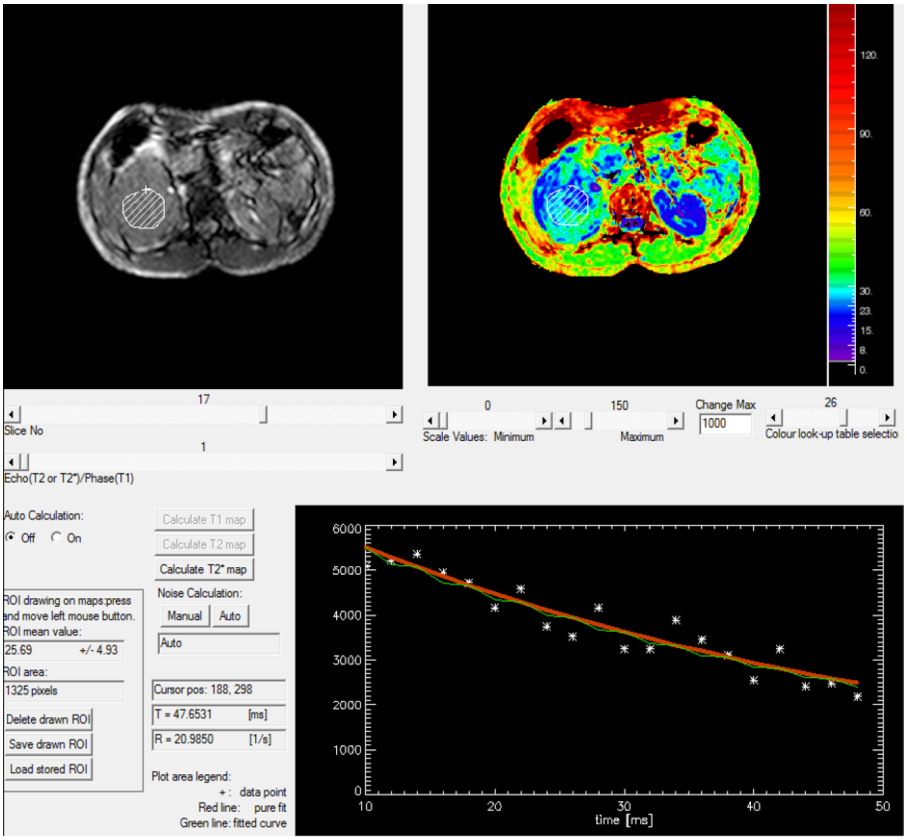

DOI: 10.4329/wjr.v14.i6.137

Figure 7 Rate of spin dephasing (R2* map) showing R2* value of right renal cell carcinoma (20.9/s), which was lower than that of a normal kidney (25.5/s).

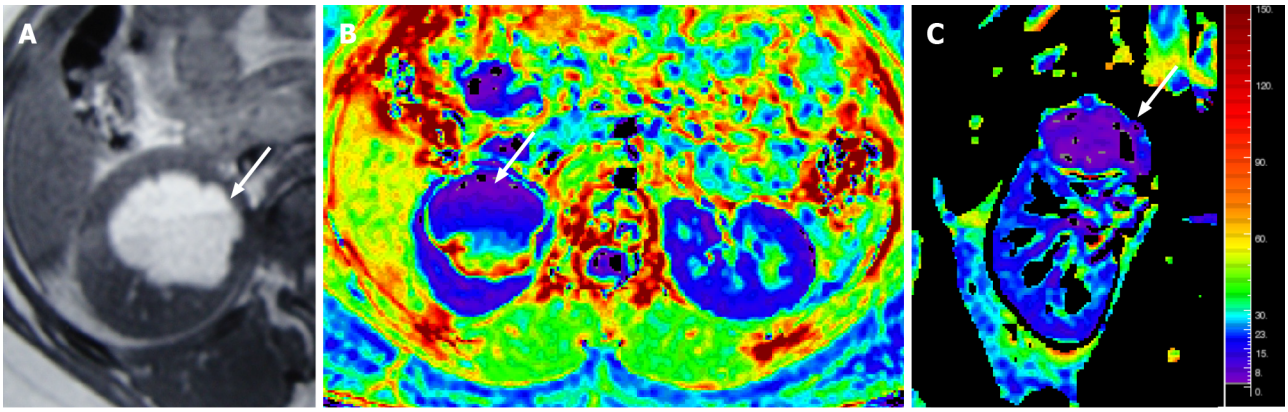

DOI: 10.4329/wjr.v14.i6.137

Figure 8 Magnetic resonance images. T1W axial MR image (A) showing a hyperintense lesion in the upper pole of the right kidney, with fluid-fluid level, suggestive of a hemorrhagic cyst; Axial & coronal R2* maps (B and C) showing an R2* value of 6.1/s.

encouraging results[77]. Several studies have shown a change in the management of RCC when gallium PSMA PET was used for primary staging compared with CECT scan due to detection of small areas of metastasis and synchronous malignancies[78]. Gallium PSMA PET is proven to be better than FDG PET for oligometastatic RCC[79].

CONCLUSION

Sonography serves as the screening modality whereas multiphasic CECT acts as the workhorse in the assessment of renal masses. MRI with DWI is a potential problem-solving adjunct technique. CEUS and

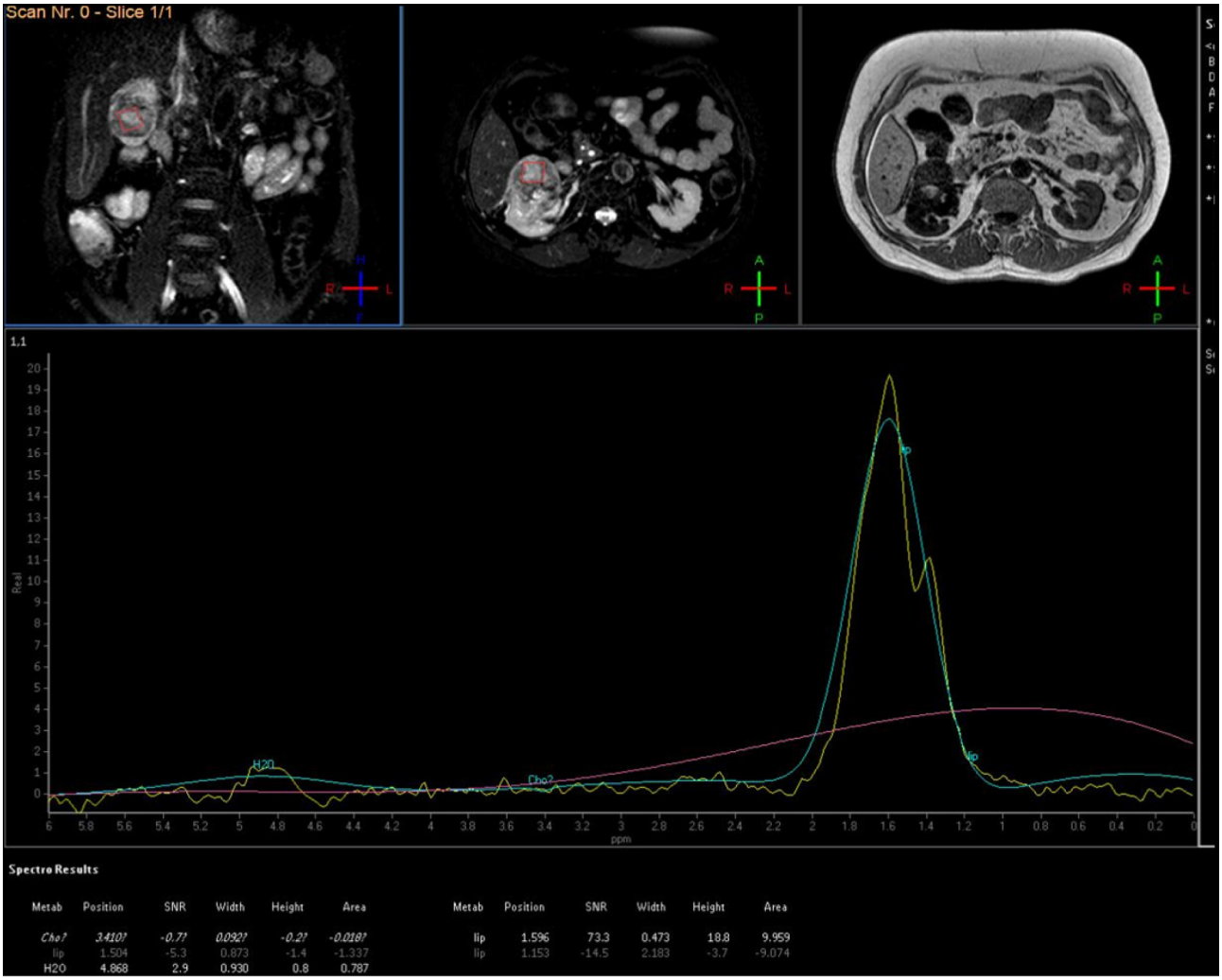

DOI: 10.4329/wjr.v14.i6.137

Figure 9 MR spectroscopy of low-grade renal cell carcinoma showed increased lipid-lactate peak.

SWE, an extension of ultrasound, provide comparable results with no added risk of nephrotoxicity or radiation-related injuries. DECT, perfusion imaging, BOLD MRI, and MR spectroscopy can be helpful in indeterminate cases. PET-CT using FDG or gallium PSMA is also finding gradual applications. The constant advancements in imaging techniques allow confident diagnosis and superior characterization of renal masses. They also serve as potential biomarkers and aid in prognostication & response assessment after chemotherapy/ablative procedures.

FOOTNOTES

Author contributions: Aggarwal A contributed to manuscript writing and original drafting; Das CJ contributed to conceptualization, and manuscript writing and editing; Sharma S contributed to supervision.

Conflict-of-interest statement: All the authors declare that they have no conflict of interest to disclose.

Country/Territory of origin: India

ORCID number: Ankita Aggarwal 0000-0003-4793-6124; Chandan J Das 0000-0001-6505-5940; Sanjay Sharma 0000-0003-0607-1611.

S-Editor: Liu JH
L-Editor: Wang TQ
P-Editor: Liu JH

REFERENCES

1 **Rossi SH**, Klatte T, Usher-Smith J, Stewart GD. Epidemiology and screening for renal cancer. *World J Urol* 2018; **36**: 1341-1353 [PMID: 29610964 DOI: 10.1007/s00345-018-2286-7]
2 **Mizuma Y**, Watanabe Y, Ozasa K, Hayashi K, Kawai K. Validity of sonographic screening for the detection of abdominal cancers. *J Clin Ultrasound* 2002; **30**: 408-415 [PMID: 12210458 DOI: 10.1002/jcu.10089]
3 **Filipas D**, Spix C, Schulz-Lampel D, Michaelis J, Hohenfellner R, Roth S, Thüroff JW. Screening for renal cell carcinoma using ultrasonography: a feasibility study. *BJU Int* 2003; **91**: 595-599 [PMID: 12699466 DOI: 10.1046/j.1464-410x.2003.04175.x]
4 **Amenta PS**, Ghobrial GM, Krespan K, Nguyen P, Ali M, Harrop JS. Cervical spondylotic myelopathy in the young adult: a review of the literature and clinical diagnostic criteria in an uncommon demographic. *Clin Neurol Neurosurg* 2014; **120**: 68-72 [PMID: 24731579 DOI: 10.1016/j.clineuro.2014.02.019]
5 **Tsili AC**, Argyropoulou MI. Advances of multidetector computed tomography in the characterization and staging of renal cell carcinoma. *World J Radiol* 2015; **7**: 110-127 [PMID: 26120380 DOI: 10.4329/wjr.v7.i6.110]
6 **Haddad MC**, Bulbul MA. Current imaging of solid renal masses. *J Med Liban* 2005; **53**: 72-79 [PMID: 16604991]
7 **Piscaglia F**, Nolsøe C, Dietrich CF, Cosgrove DO, Gilja OH, Bachmann Nielsen M, Albrecht T, Barozzi L, Bertolotto M, Catalano O, Claudon M, Clevert DA, Correas JM, D'Onofrio M, Drudi FM, Eyding J, Giovannini M, Hocke M, Ignee A, Jung EM, Klauser AS, Lassau N, Leen E, Mathis G, Saftoiu A, Seidel G, Sidhu PS, terHaar G, Timmerman D, Weskott HP. The EFSUMB Guidelines and Recommendations on the Clinical Practice of Contrast Enhanced Ultrasound (CEUS): update 2011 on non-hepatic applications. *Ultraschall Med* 2012; **33**: 33-59 [PMID: 21874631 DOI: 10.1055/s-0031-1281676]
8 **Sidhu PS**, Cantisani V, Dietrich CF, Gilja OH, Saftoiu A, Bartels E, Bertolotto M, Calliada F, Clevert DA, Cosgrove D, Deganello A, D'Onofrio M, Drudi FM, Freeman S, Harvey C, Jenssen C, Jung EM, Klauser AS, Lassau N, Meloni MF, Leen E, Nicolau C, Nolsoe C, Piscaglia F, Prada F, Prosch H, Radzina M, Savelli L, Weskott HP, Wijkstra H. The EFSUMB Guidelines and Recommendations for the Clinical Practice of Contrast-Enhanced Ultrasound (CEUS) in Non-Hepatic Applications: Update 2017 (Long Version). *Ultraschall Med* 2018; **39**: e2-e44 [PMID: 29510439 DOI: 10.1055/a-0586-1107]
9 **Cokkinos DD**, Antypa EG, Skilakaki M, Kriketou D, Tavernaraki E, Piperopoulos PN. Contrast enhanced ultrasound of the kidneys: what is it capable of? *Biomed Res Int* 2013; **2013**: 595873 [PMID: 24455707 DOI: 10.1155/2013/595873]
10 **Correas JM**, Claudon M, Tranquart F, Hélénon AO. The kidney: imaging with microbubble contrast agents. *Ultrasound Q* 2006; **22**: 53-66 [PMID: 16641794]
11 **Mazziotti S**, Zimbaro F, Pandolfo A, Racchiusa S, Settineri N, Ascenti G. Usefulness of contrast-enhanced ultrasonography in the diagnosis of renal pseudotumors. *Abdom Imaging* 2010; **35**: 241-245 [PMID: 19194642 DOI: 10.1007/s00261-008-9499-y]
12 **Barr RG**, Peterson C, Hindi A. Evaluation of indeterminate renal masses with contrast-enhanced US: a diagnostic performance study. *Radiology* 2014; **271**: 133-142 [PMID: 24475802 DOI: 10.1148/radiol.13130161]
13 **Quaia E**, Bertolotto M, Cioffi V, Rossi A, Baratella E, Pizzolato R, Cov MA. Comparison of contrast-enhanced sonography with unenhanced sonography and contrast-enhanced CT in the diagnosis of malignancy in complex cystic renal masses. *AJR Am J Roentgenol* 2008; **191**: 1239-1249 [PMID: 18806171 DOI: 10.2214/AJR.07.3546]
14 **Clevert DA**, Minaifar N, Weckbach S, Jung EM, Stock K, Reiser M, Staehler M. Multislice computed tomography versus contrast-enhanced ultrasound in evaluation of complex cystic renal masses using the Bosniak classification system. *Clin HemorheolMicrocirc* 2008; **39**: 171-178 [PMID: 18503122]
15 **Park BK**, Kim B, Kim SH, Ko K, Lee HM, Choi HY. Assessment of cystic renal masses based on Bosniak classification: comparison of CT and contrast-enhanced US. *Eur J Radiol* 2007; **61**: 310-314 [PMID: 17097844 DOI: 10.1016/j.ejrad.2006.10.004]
16 **Ascenti G**, Mazziotti S, Zimbaro G, Settineri N, Magno C, Melloni D, Caruso R, Scribano E. Complex cystic renal masses: characterization with contrast-enhanced US. *Radiology* 2007; **243**: 158-165 [PMID: 17392251 DOI: 10.1148/radiol.2431051924]
17 **Bertolotto M**, Cicero C, Perrone R, Degrassi F, Cacciato F, Cova MA. Renal Masses With Equivocal Enhancement at CT: Characterization With Contrast-Enhanced Ultrasound. *AJR Am J Roentgenol* 2015; **204**: W557-W565 [PMID: 25905962 DOI: 10.2214/AJR.14.13375]
18 **Granata A**, Zanoli L, Insalaco M, Valentino M, Pavlica P, Di Nicolò PP, Scuderi M, Fiorini F, Fatuzzo P, Bertolotto M. Contrast-enhanced ultrasound (CEUS) in nephrology: Has the time come for its widespread use? *Clin Exp Nephrol* 2015; **19**: 606-615 [PMID: 25351822 DOI: 10.1007/s10157-014-1040-8]
19 **Tickoo SK**, dePeralta-Venturina MN, Harik LR, Worcester HD, Salama ME, Young AN, Moch H, Amin MB. Spectrum of epithelial neoplasms in end-stage renal disease: an experience from 66 tumor-bearing kidneys with emphasis on histologic patterns distinct from those in sporadic adult renal neoplasia. *Am J Surg Pathol* 2006; **30**: 141-153 [PMID: 16434887 DOI: 10.1097/01.pas.0000185382.80844.b1]
20 **Ignee A**, Straub B, Brix D, Schuessler G, Ott M, Dietrich CF. The value of contrast enhanced ultrasound (CEUS) in the characterisation of patients with renal masses. *Clin HemorheolMicrocirc* 2010; **46**: 275-290 [PMID: 21187576 DOI: 10.3233/CH-2010-1352]
21 **Fontanilla T**, Minaya J, Cortés C, Hernando CG, Arangüena RP, Arriaga J, Carmona MS, Alcolado A. Acute complicated pyelonephritis: contrast-enhanced ultrasound. *Abdom Imaging* 2012; **37**: 639-646 [PMID: 21792579 DOI:

10.1007/s00261-011-9781-2]
22 **Cai Y**, Li F, Li Z, Du L, Wu R. Diagnostic Performance of Ultrasound Shear Wave Elastography in Solid Small (≤4 cm) Renal Parenchymal Masses. *Ultrasound Med Biol* 2019; **45**: 2328-2337 [PMID: 31196747 DOI: 10.1016/j.ultrasmedbio.2019.05.010]
23 **Onur MR**, Poyraz AK, Bozgeyik Z, Onur AR, Orhan I. Utility of semiquantitative strain elastography for differentiation between benign and malignant solid renal masses. *J Ultrasound Med* 2015; **34**: 639-647 [PMID: 25792579 DOI: 10.7863/ultra.34.4.639]
24 **Keskin S**, Güven S, Keskin Z, Özbiner H, Kerimoğlu Ü, Yeşildağ A. Strain elastography in the characterization of renal cell carcinoma and angiomyolipoma. *Can Urol Assoc J* 2015; **9**: e67-e71 [PMID: 25737764 DOI: 10.5489/cuaj.2349]
25 **Aydin S**, Yildiz S, Turkmen I, Sharifov R, Uysal O, Gucin Z, Armagan A, Kocakoc E. Value of Shear Wave Elastography for differentiating benign and malignant renal lesions. *Med Ultrason* 2018; **1**: 21-26 [PMID: 29400363 DOI: 10.11152/mu-1161]
26 **Graser A**, Johnson TR, Hecht EM, Becker CR, Leidecker C, Staehler M, Stief CG, Hildebrandt H, Godoy MC, Finn ME, Stepansky F, Reiser MF, Macari M. Dual-energy CT in patients suspected of having renal masses: can virtual nonenhanced images replace true nonenhanced images? *Radiology* 2009; **252**: 433-440 [PMID: 19487466 DOI: 10.1148/radiol.2522080557]
27 **Ascenti G**, Mazziotti S, Mileto A, Racchiusa S, Donato R, Settineri N, Gaeta M. Dual-source dual-energy CT evaluation of complex cystic renal masses. *AJR Am J Roentgenol* 2012; **199**: 1026-1034 [PMID: 23096175 DOI: 10.2214/AJR.11.7711]
28 **Salameh JP**, McInnes MDF, McGrath TA, Salameh G, Schieda N. Diagnostic Accuracy of Dual-Energy CT for Evaluation of Renal Masses: Systematic Review and Meta-Analysis. *AJR Am J Roentgenol* 2019; **212**: W100-W105 [PMID: 30714831 DOI: 10.2214/AJR.18.20527]
29 **Chandarana H**, Megibow AJ, Cohen BA, Srinivasan R, Kim D, Leidecker C, Macari M. Iodine quantification with dual-energy CT: phantom study and preliminary experience with renal masses. *AJR Am J Roentgenol* 2011; **196**: W693-W700 [PMID: 21606256 DOI: 10.2214/AJR.10.5541]
30 **Ascenti G**, Mileto A, Krauss B, Gaeta M, Blandino A, Scribano E, Settineri N, Mazziotti S. Distinguishing enhancing from nonenhancing renal masses with dual-source dual-energy CT: iodine quantification versus standard enhancement measurements. *EurRadiol* 2013; **23**: 2288-2295 [PMID: 23479222 DOI: 10.1007/s00330-013-2811-4]
31 **Kaza RK**, Ananthakrishnan L, Kambadakone A, Platt JF. Update of Dual-Energy CT Applications in the Genitourinary Tract. *AJR Am J Roentgenol* 2017; **208**: 1185-1192 [PMID: 28301210 DOI: 10.2214/AJR.16.17742]
32 **Mileto A**, Nelson RC, Paulson EK, Marin D. Dual-Energy MDCT for Imaging the Renal Mass. *AJR Am J Roentgenol* 2015; **204**: W640-W647 [PMID: 25730444 DOI: 10.2214/AJR.14.14094]
33 **Mileto A**, Marin D, Nelson RC, Ascenti G, Boll DT. Dual energy MDCT assessment of renal lesions: an overview. *EurRadiol* 2014; **24**: 353-362 [PMID: 24092045 DOI: 10.1007/s00330-013-3030-8]
34 **Salameh JP**, McInnes MDF, McGrath TA, Salameh G, Schieda N. Diagnostic Accuracy of Dual-Energy CT for Evaluation of Renal Masses: Systematic Review and Meta-Analysis. *AJR Am J Roentgenol* 2019; **212**: W100-W105 [PMID: 30714831 DOI: 10.2214/AJR.18.20527]
35 **Das CJ**, Thingujam U, Panda A, Sharma S, Gupta AK. Perfusion computed tomography in renal cell carcinoma. *World J Radiol* 2015; **7**: 170-179 [PMID: 26217456 DOI: 10.4329/wjr.v7.i7.170]
36 **Gilet AG**, Kang SK, Kim D, Chandarana H. Advanced renal mass imaging: diffusion and perfusion MRI. *CurrUrol Rep* 2012; **13**: 93-98 [PMID: 22081252 DOI: 10.1007/s11934-011-0227-8]
37 **Alsop DC**, Detre JA. Multisection cerebral blood flow MR imaging with continuous arterial spin labeling. *Radiology* 1998; **208**: 410-416 [PMID: 9680569 DOI: 10.1148/radiology.208.2.9680569]
38 **Martirosian P**, Klose U, Mader I, Schick F. FAIR true-FISP perfusion imaging of the kidneys. *MagnReson Med* 2004; **51**: 353-361 [PMID: 14755661 DOI: 10.1002/mrm.10709]
39 **Fenchel M**, Martirosian P, Langanke J, Giersch J, Miller S, Stauder NI, Kramer U, Claussen CD, Schick F. Perfusion MR imaging with FAIR true FISP spin labeling in patients with and without renal artery stenosis: initial experience. *Radiology* 2006; **238**: 1013-1021 [PMID: 16439565 DOI: 10.1148/radiol.2382041623]
40 **Lanzman RS**, Wittsack HJ, Martirosian P, Zgoura P, Bilk P, Kröpil P, Schick F, Voiculescu A, Blondin D. Quantification of renal allograft perfusion using arterial spin labeling MRI: initial results. *EurRadiol* 2010; **20**: 1485-1491 [PMID: 19949799 DOI: 10.1007/s00330-009-1675-0]
41 **Palmowski M**, Schifferdecker I, Zwick S, Macher-Goeppinger S, Laue H, Haferkamp A, Kauczor HU, Kiessling F, Hallscheidt P. Tumor perfusion assessed by dynamic contrast-enhanced MRI correlates to the grading of renal cell carcinoma: initial results. *Eur J Radiol* 2010; **74**: e176-e180 [PMID: 19540690 DOI: 10.1016/j.ejrad.2009.05.042]
42 **Hillman GG**, Singh-Gupta V, Al-Bashir AK, Zhang H, Yunker CK, Patel AD, Sethi S, Abrams J, Haacke EM. Dynamic contrast-enhanced magnetic resonance imaging of sunitinib-induced vascular changes to schedule chemotherapy in renal cell carcinoma xenograft tumors. *Transl Oncol* 2010; **3**: 293-306 [PMID: 20885892 DOI: 10.1593/tlo.10136]
43 **Galbraith SM**, Maxwell RJ, Lodge MA, Tozer GM, Wilson J, Taylor NJ, Stirling JJ, Sena L, Padhani AR, Rustin GJ. Combretastatin A4 phosphate has tumor antivascular activity in rat and man as demonstrated by dynamic magnetic resonance imaging. *J Clin Oncol* 2003; **21**: 2831-2842 [PMID: 12807936 DOI: 10.1200/JCO.2003.05.187]
44 **Flaherty KT**, Rosen MA, Heitjan DF, Gallagher ML, Schwartz B, Schnall MD, O'Dwyer PJ. Pilot study of DCE-MRI to predict progression-free survival with sorafenib therapy in renal cell carcinoma. *Cancer Biol Ther* 2008; **7**: 496-501 [PMID: 18219225 DOI: 10.4161/cbt.7.4.5624]
45 **Padhani AR**, Liu G, Koh DM, Chenevert TL, Thoeny HC, Takahara T, Dzik-Jurasz A, Ross BD, Van Cauteren M, Collins D, Hammoud DA, Rustin GJ, Taouli B, Choyke PL. Diffusion-weighted magnetic resonance imaging as a cancer biomarker: consensus and recommendations. *Neoplasia* 2009; **11**: 102-125 [PMID: 19186405 DOI: 10.1258/ar.2011.110415]
46 **Goyal A**, Sharma R, Bhalla AS, Gamanagatti S, Seth A, Iyer VK, Das P. Diffusion-weighted MRI in renal cell carcinoma: a surrogate marker for predicting nuclear grade and histological subtype. *Acta Radiol* 2012; **53**: 349-358 [PMID: 22496427 DOI: 10.1258/ar.2011.110415]

47 **Squillaci E**, Manenti G, Di Stefano F, Miano R, Strigari L, Simonetti G. Diffusion-weighted MR imaging in the evaluation of renal tumours. *J Exp Clin Cancer Res* 2004; **23**: 39-45 [PMID: 15149149]

48 **Cova M**, Squillaci E, Stacul F, Manenti G, Gava S, Simonetti G, Pozzi-Mucelli R. Diffusion-weighted MRI in the evaluation of renal lesions: preliminary results. *Br J Radiol* 2004; **77**: 851-857 [PMID: 15482997 DOI: 10.1259/bjr/26525081]

49 **Yoshikawa T**, Kawamitsu H, Mitchell DG, Ohno Y, Ku Y, Seo Y, Fujii M, Sugimura K. ADC measurement of abdominal organs and lesions using parallel imaging technique. *AJR Am J Roentgenol* 2006; **187**: 1521-1530 [PMID: 17114546 DOI: 10.2214/AJR.05.0778]

50 **Zhang J**, Tehrani YM, Wang L, Ishill NM, Schwartz LH, Hricak H. Renal masses: characterization with diffusion-weighted MR imaging--a preliminary experience. *Radiology* 2008; **247**: 458-464 [PMID: 18430878 DOI: 10.1148/radiol.2472070823]

51 **Taouli B**, Thakur RK, Mannelli L, Babb JS, Kim S, Hecht EM, Lee VS, Israel GM. Renal lesions: characterization with diffusion-weighted imaging versus contrast-enhanced MR imaging. *Radiology* 2009; **251**: 398-407 [PMID: 19276322 DOI: 10.1148/radiol.2512080880]

52 **Kilickesmez O**, Inci E, Atilla S, Tasdelen N, Yetimoğlu B, Yencilek F, Gurmen N. Diffusion-weighted imaging of the renal and adrenal lesions. *J Comput Assist Tomogr* 2009; **33**: 828-833 [PMID: 19940645 DOI: 10.1097/RCT.0b013e31819f1b83]

53 **Sandrasegaran K**, Sundaram CP, Ramaswamy R, Akisik FM, Rydberg MP, Lin C, Aisen AM. Usefulness of diffusion-weighted imaging in the evaluation of renal masses. *AJR Am J Roentgenol* 2010; **194**: 438-445 [PMID: 20093607 DOI: 10.2214/AJR.09.3024]

54 **Agnello F**, Roy C, Bazille G, Galia M, Midiri M, Charles T, Lang H. Small solid renal masses: characterization by diffusion-weighted MRI at 3 T. *Clin Radiol* 2013; **68**: e301-e308 [PMID: 23452876 DOI: 10.1016/j.crad.2013.01.002]

55 **Le Bihan D**, Breton E, Lallemand D, Grenier P, Cabanis E, Laval-Jeantet M. MR imaging of intravoxel incoherent motions: application to diffusion and perfusion in neurologic disorders. *Radiology* 1986; **161**: 401-407 [PMID: 3763909 DOI: 10.1148/radiology.161.2.3763909]

56 **Jensen JH**, Helpern JA, Ramani A, Lu H, Kaczynski K. Diffusional kurtosis imaging: the quantification of non-gaussian water diffusion by means of magnetic resonance imaging. *MagnReson Med* 2005; **53**: 1432-1440 [PMID: 15906300 DOI: 10.1002/mrm.20508]

57 **Ding Y**, Tan Q, Mao W, Dai C, Hu X, Hou J, Zeng M, Zhou J. Differentiating between malignant and benign renal tumors: do IVIM and diffusion kurtosis imaging perform better than DWI? *EurRadiol* 2019; **29**: 6930-6939 [PMID: 31161315 DOI: 10.1007/s00330-019-06240-6]

58 **Li LP**, Halter S, Prasad PV. Blood oxygen level-dependent MR imaging of the kidneys. *MagnReson Imaging Clin N Am* 2008; **16**: 613-625, viii [PMID: 18926426 DOI: 10.1016/j.mric.2008.07.008]

59 **Blatow M**, Nennig E, Durst A, Sartor K, Stippich C. fMRI reflects functional connectivity of human somatosensory cortex. *Neuroimage* 2007; **37**: 927-936 [PMID: 17629500 DOI: 10.1016/j.neuroimage.2007.05.038]

60 **Shen Q**, Ren H, Duong TQ. CBF, BOLD, CBV, and CMRO(2) fMRI signal temporal dynamics at 500-msec resolution. *J MagnReson Imaging* 2008; **27**: 599-606 [PMID: 18219630 DOI: 10.1002/jmri.21203]

61 **Fukunaga M**, Horovitz SG, de Zwart JA, van Gelderen P, Balkin TJ, Braun AR, Duyn JH. Metabolic origin of BOLD signal fluctuations in the absence of stimuli. *J Cereb Blood Flow Metab* 2008; **28**: 1377-1387 [PMID: 18382468 DOI: 10.1038/jcbfm.2008.25]

62 **Herrmann CS**, Debener S. Simultaneous recording of EEG and BOLD responses: a historical perspective. *Int J Psychophysiol* 2008; **67**: 161-168 [PMID: 17719112 DOI: 10.1016/j.ijpsycho.2007.06.006]

63 **Textor SC**, Glockner JF, Lerman LO, Misra S, McKusick MA, Riederer SJ, Grande JP, Gomez SI, Romero JC. The use of magnetic resonance to evaluate tissue oxygenation in renal artery stenosis. *J Am Soc Nephrol* 2008; **19**: 780-788 [PMID: 18287564 DOI: 10.1681/ASN.2007040420]

64 **Alford SK**, Sadowski EA, Unal O, Polzin JA, Consigny DW, Korosec FR, Grist TM. Detection of acute renal ischemia in swine using blood oxygen level-dependent magnetic resonance imaging. *J MagnReson Imaging* 2005; **22**: 347-353 [PMID: 16104014 DOI: 10.1002/jmri.20389]

65 **Juillard L**, Lerman LO, Kruger DG, Haas JA, Rucker BC, Polzin JA, Riederer SJ, Romero JC. Blood oxygen level-dependent measurement of acute intra-renal ischemia. *Kidney Int* 2004; **65**: 944-950 [PMID: 14871414 DOI: 10.1111/j.1523-1755.2004.00469.x]

66 **Castillo M**, Kwock L, Mukherji SK. Clinical applications of proton MR spectroscopy. *AJNR Am J Neuroradiol* 1996; **17**: 1-15 [PMID: 8770242]

67 **Bottomley PA**, Edelstein WA, Foster TH, Adams WA. In vivo solvent-suppressed localized hydrogen nuclear magnetic resonance spectroscopy: a window to metabolism? *Proc Natl Acad Sci U S A* 1985; **82**: 2148-2152 [PMID: 3856889 DOI: 10.1073/pnas.82.7.2148]

68 **Nurenberg P**, Sartoni-D'Ambrosia G, Szczepaniak LS. Magnetic resonance spectroscopy of renal and other retroperitoneal tumors. *CurrOpinUrol* 2002; **12**: 375-380 [PMID: 12172423 DOI: 10.1097/00042307-200209000-00002]

69 **Kim DY**, Kim KB, Kim OD, Kim JK. Localized in vivo proton spectroscopy of renal cell carcinoma in human kidney. *J Korean Med Sci* 1998; **13**: 49-53 [PMID: 9539319 DOI: 10.3346/jkms.1998.13.1.49]

70 **Cecil KM**. Proton magnetic resonance spectroscopy: technique for the neuroradiologist. *Neuroimaging Clin N Am* 2013; **23**: 381-392 [PMID: 23928195 DOI: 10.1016/j.nic.2012.10.003]

71 **Caldarella C**, Muoio B, Isgrò MA, Porfiri E, Treglia G, Giovanella L. The role of fluorine-18-fluorodeoxyglucose positron emission tomography in evaluating the response to tyrosine-kinase inhibitors in patients with metastatic primary renal cell carcinoma. *Radiol Oncol* 2014; **48**: 219-227 [PMID: 25177235 DOI: 10.2478/raon-2013-0067]

72 **Smaldone MC**, Uzzo RG. Balancing process and risk: standardizing posttreatment surveillance for renal cell carcinoma. *J Urol* 2013; **190**: 417-418 [PMID: 23688642 DOI: 10.1016/j.juro.2013.05.033]

73 **Alongi P**, Picchio M, Zattoni F, Spallino M, Gianolli L, Saladini G, Evangelista L. Recurrent renal cell carcinoma: clinical and prognostic value of FDG PET/CT. *Eur J Nucl Med Mol Imaging* 2016; **43**: 464-473 [PMID: 26268680 DOI:

10.1007/s00259-015-3159-6]
74 **Kang DE**, White RL Jr, Zuger JH, Sasser HC, Teigland CM. Clinical use of fluorodeoxyglucose F 18 positron emission tomography for detection of renal cell carcinoma. *J Urol* 2004; **171**: 1806-1809 [PMID: 15076281 DOI: 10.1097/01.ju.0000120241.50061.e4]
75 **Takahashi M**, Kume H, Koyama K, Nakagawa T, Fujimura T, Morikawa T, Fukayama M, Homma Y, Ohtomo K, Momose T. Preoperative evaluation of renal cell carcinoma by using 18F-FDG PET/CT. *Clin Nucl Med* 2015; **40**: 936-940 [PMID: 26164183 DOI: 10.1097/RLU.0000000000000875]
76 **Jena R**, Narain TA, Singh UP, Srivastava A. Role of positron emission tomography/computed tomography in the evaluation of renal cell carcinoma. *Indian J Urol* 2021; **37**: 125-132 [PMID: 34103794 DOI: 10.4103/iju.IJU_268_20]
77 **Evangelista L**, Zattoni F, Alongi P. ^{68}Ga-dotatoc *vs.* ^{18}F-FDG *vs.*radiolabelled PSMA PET/CT in renal cancer patients. *Ann Transl Med* 2019; **7**: S150 [PMID: 31576357 DOI: 10.21037/atm.2019.06.28]
78 **Raveenthiran S**, Esler R, Yaxley J, Kyle S. The use of ^{68}Ga-PET/CT PSMA in the staging of primary and suspected recurrent renal cell carcinoma. *Eur J Nucl Med Mol Imaging* 2019; **46**: 2280-2288 [PMID: 31332498 DOI: 10.1007/s00259-019-04432-2]
79 **Siva S**, Callahan J, Pryor D, Martin J, Lawrentschuk N, Hofman MS. Utility of ^{68} Ga prostate specific membrane antigen - positron emission tomography in diagnosis and response assessment of recurrent renal cell carcinoma. *J Med Imaging Radiat Oncol* 2017; **61**: 372-378 [PMID: 28116853 DOI: 10.1111/1754-9485.12590]

World Journal of Radiology

Submit a Manuscript: https://www.f6publishing.com

World J Radiol 2022 June 28; 14(6): 151-154

DOI: 10.4329/wjr.v14.i6.151

ISSN 1949-8470 (online)

MINIREVIEWS

Artificial intelligence technologies in nuclear medicine

Muge Oner Tamam, Muhlis Can Tamam

Specialty type: Radiology, nuclear medicine and medical imaging

Provenance and peer review: Invited article; Externally peer reviewed.

Peer-review model: Single blind

Peer-review report's scientific quality classification

Grade A (Excellent): 0
Grade B (Very good): B
Grade C (Good): C
Grade D (Fair): D
Grade E (Poor): 0

P-Reviewer: Liu J, China; Morilla I, France; Tanabe S, Japan
A-Editor: Yao QG, China

Received: January 31, 2022
Peer-review started: January 31, 2022
First decision: April 8, 2022
Revised: April 20, 2022
Accepted: June 13, 2022
Article in press: June 13, 2022
Published online: June 28, 2022

Muge Oner Tamam, Department of Nuclear Medicine, Prof. Dr. Cemil Tascioglu City Hospital, İstanbul 34381, Turkey

Muhlis Can Tamam, High School, Uskudar American Academy, İstanbul 34145, Turkey

Corresponding author: Muge Oner Tamam, MD, Associate Professor, Department of Nuclear Medicine, Prof. Dr. Cemil Tascioglu City Hospital, Darulaceze cad., İstanbul 34381, Turkey. mugeoner@yahoo.com

Abstract

The use of artificial intelligence plays a crucial role in developing precision medicine in nuclear medicine. Artificial intelligence refers to a field of computer science aimed at imitating the performance of tasks typically requiring human intelligence. From machine learning to generative adversarial networks, artificial intelligence automized the workflow of medical imaging. In this mini-review, we encapsulate artificial intelligence models and their use in nuclear medicine imaging workflow.

Key Words: Artificial intelligence; Machine learning; Deep learning; Artificial neural networks; Convolutional neural networks; Generative adversarial networks

Core Tip: Artificial intelligence is a distinguished tool for creating tailor-made medicine. Artificial intelligence (AI) consists of machine learning, deep learning, artificial neural networks, convolutional neural networks, and generative adversarial networks. These AI applications affect all phases of a routine medical imaging workflow in nuclear medicine: planning, image acquisition, and interpretation. The integration of AI into clinical workflow and protocols of medical imaging will provide the opportunity to decrease the error rate of physicians and eventually lead to improved patient management.

Citation: Tamam MO, Tamam MC. Artificial intelligence technologies in nuclear medicine. *World J Radiol* 2022; 14(6): 151-154
URL: https://www.wjgnet.com/1949-8470/full/v14/i6/151.htm
DOI: https://dx.doi.org/10.4329/wjr.v14.i6.151

INTRODUCTION

Personalized medicine (precision medicine) is a developing medical practice that develops tailor-made approaches for individual patients, leading to increased reliability and a significant impact on preventative, diagnostic, and therapeutic pathways[1]. Artificial intelligence (AI) integration plays a significant role in achieving precision medicine in nuclear medicine[2]. It refers to a field of computer science aimed at imitating the performance of tasks typically requiring human intelligence[3]. Advancements in AI have allowed for precision medicine models to be developed for individual patients (Figure 1, Table 1). The advancements in AI have been in the order of machine learning (ML), deep learning (DL), artificial neural networks (ANNs), convolutional neural networks (CNNs), and generative adversarial networks (GANs)[4,5].

AI MODELS

Machine learning is not a singular algorithm, but a subset of AI. It processes a set of training data and constructs a model that carries the associations among the variables that are relevant to a particular outcome. It usually needs handcrafted features, requiring more human intervention, for data extraction and filtration[2]. There are many ML methods, some of which are supervised learning, unsupervised learning, semi-supervised learning, and reinforcement machine learning[5,6]. DL is a subset of ML, automating many parts of input extraction, enabling less human intervention. In contrast, ML requires more human intervention for data extraction and filtration[2,5,6].

Artificial Neural Networks are a subfield of DL. ANNs are connected nodes with weighted paths. Each node has parent nodes that influence it, an activation function, firing threshold, and an output value. ANNs are analogous to neurons and their intercommunication[4,5].

Convolutional Neural Networks are made up of convoluting series of pooling layers. CNNs apply a neural-network layer to a part of an image and systematically traverse over the image. CNNs downsample and summarize features by alternating convolutional layers with pooling layers. Their computational requirements are much lower because they operate on a small subset of an image[4,5].

Generative Adversarial Networks are made up of two networks, a generator, and a discriminator, that are in a zero-sum game. Generators generate fake input data to minimize the difference between counterfeits and real inputs. The discriminator classifies the real and counterfeit inputs, attempting to maximize efficiency. Over time, the generator will be good at generating input data and the discriminator will be good at classification[5].

APPLICATIONS

AI advancements in the last decade have improved AI's application in medical imaging. The myriad of applications of AI in nuclear medicine includes all steps of a typical medical imaging workflow: planning, image acquisition, and interpretation. In the future, even patient admission and payment could be included[7-9].

For medical imaging planning, AI will automatically check for specific contraindications, such as allergies and drug interference, or eliminate needless repetition of exams by evaluating past examinations before any examination is done on a patient[10,11].

In nuclear medicine, attenuation maps and scatter correction remain relevant topics for image scanning, thus AI research focuses on these topics intensively. Hwang *et al*[10] generated attenuation maps for whole-body positron emission tomography/magnetic resonance imaging (PET/MRI) using a modified U-Net, a specialized convolutional network architecture for biomedical image segmentation. They compared the CT-derived attenuation map to the Dixon-based 4-segment technique[10,11].

Another hot topic for research is the enhancement of image quality; Hong *et al*[12] improved the picture resolution and noise properties of PET scanners using large pixelated crystals with a deep residual convolutional neural network[12,13]. Kim *et al*[14] demonstrated that Iterative PET reconstruction employing denoising CNNs and local linear fitting enhanced picture quality and robustness to noise-level disparities.

For the interpretation of images, studies on an AI-based triage system for identifying artifacts have been published recently[15]. In the near future, similar systems will be able to detect directly using raw data, such as sinograms, and issue alarms throughout the scanning process, even before reconstruction, so that technicians can adjust or prolong the scheduled scan procedure to accommodate an unexpected discovery[16]. Automated identification of pathologies provides additional intriguing potential in identifying overlooked results and secondary discoveries, saving time and effort[17].

Table 1 Artificial intelligence techniques in nuclear medicine

Machine learning (ML)
Deep learning (DL)
Artificial neural networks (ANNs)
Convolutional neural networks (CNNs)
Generative adversarial networks(GANs)

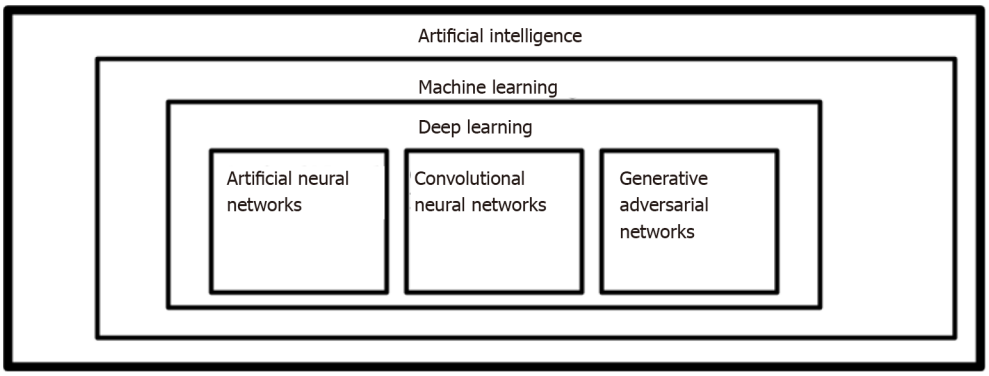

DOI: 10.4329/wjr.v14.i6.151

Figure 1 Current artificial intelligence subfields studied in the field of nuclear medicine.

ETHICAL CONSIDERATIONS, DATA PROTECTION, REGULATIONS, AND PRIVACY

Despite the improvements that the field of AI brings to nuclear medicine, there are drawbacks. Ethical considerations, data protection, legal regulations, privacy, and education are among these problems. According to Hagendorf, the ethical concerns of AI in healthcare can be summarized in the "fairness, accountability, and transparency paradigm of AI ethics"[18,19]. Moreover, AI requires considerable sensitive data in healthcare, thus standards for data protection and privacy raise issues that must be dealt with. Furthermore, for AI to generalize large numbers, large amounts of data with variability are needed. This raises more questions about consent, data anonymization, and de-identification[19]. There are promising techniques being developed on top of DL algorithms such as federative learning that might mitigate some of these issues[20]. Additionally, traditional regulatory pathways are lagging behind the recent advancements, creating difficulties regarding regulations and laws. Lastly, insufficient education about AI both from patients, physicians, and academia causes mistrust of AI applications in healthcare. Physicians and academia need familiarity with AI and the rudimentary knowledge necessary to provide patients with the necessary information[19].

CONCLUSION

The integration of AI into clinical practice will transform the medical profession and nuclear medicine imaging in particular. New abilities, such as clinical data science, computer science, and ML will be considered a necessity when AI is applied to medical imaging workflow and protocols. This could provide the opportunity to decrease the error rate of physicians and eventually lead to improved patient management.

FOOTNOTES

Author contributions: Tamam MO performed the majority of the writing, prepared the figures and tables; Tamam MC performed data accusation and writing; Tamam MC provided the input in writing the paper; Tamam MC designed the outline and coordinated the writing of the paper.

Conflict-of-interest statement: There is no conflict of interest associated with the senior author or other coauthors who contributed their efforts to this manuscript.

Country/Territory of origin: Turkey

ORCID number: Muge Oner Tamam 0000-0002-3793-0178; Muhlis Can Tamam 0000-0002-1327-8947.

S-Editor: Liu JH
L-Editor: A
P-Editor: Liu JH

REFERENCES

1 National Human Genome Research Institute. Personalized Medicine. Available from: https://www.genome.gov/genetics-glossary/Personalized-Medicine
2 **Chartrand G**, Cheng PM, Vorontsov E, Drozdzal M, Turcotte S, Pal CJ, Kadoury S, Tang A. Deep Learning: A Primer for Radiologists. *Radiographics* 2017; **37**: 2113-2131 [PMID: 29131760 DOI: 10.1148/rg.2017170077]
3 **Currie G**, Rohren E. Intelligent Imaging in Nuclear Medicine: the Principles of Artificial Intelligence, Machine Learning and Deep Learning. *Semin Nucl Med* 2021; **51**: 102-111 [PMID: 33509366 DOI: 10.1053/j.semnuclmed.2020.08.002]
4 **Herskovits EH**. Artificial intelligence in molecular imaging. *Ann Transl Med* 2021; **9**: 824 [PMID: 34268437 DOI: 10.21037/atm-20-6191]
5 **Castiglioni I**, Rundo L, Codari M, Di Leo G, Salvatore C, Interlenghi M, Gallivanone F, Cozzi A, D'Amico NC, Sardanelli F. AI applications to medical images: From machine learning to deep learning. *Phys Med* 2021; **83**: 9-24 [PMID: 33662856 DOI: 10.1016/j.ejmp.2021.02.006]
6 Machine Learning. Available from: https://www.ibm.com/cloud/Learn/machine-learning
7 **Visvikis D**, Cheze Le Rest C, Jaouen V, Hatt M. Artificial intelligence, machine (deep) learning and radio(geno)mics: definitions and nuclear medicine imaging applications. *Eur J Nucl Med Mol Imaging* 2019; **46**: 2630-2637 [PMID: 31280350 DOI: 10.1007/s00259-019-04373-w]
8 **Currie GM**. Intelligent Imaging: Artificial Intelligence Augmented Nuclear Medicine. *J Nucl Med Technol* 2019; **47**: 217-222 [PMID: 31401616 DOI: 10.2967/jnmt.119.232462]
9 **Currie G**, Hawk KE, Rohren E, Vial A, Klein R. Machine Learning and Deep Learning in Medical Imaging: Intelligent Imaging. *J Med Imaging Radiat Sci* 2019; **50**: 477-487 [PMID: 31601480 DOI: 10.1016/j.jmir.2019.09.005]
10 **Hwang D**, Kang SK, Kim KY, Seo S, Paeng JC, Lee DS, Lee JS. Generation of PET Attenuation Map for Whole-Body Time-of-Flight ^{18}F-FDG PET/MRI Using a Deep Neural Network Trained with Simultaneously Reconstructed Activity and Attenuation Maps. *J Nucl Med* 2019; **60**: 1183-1189 [PMID: 30683763 DOI: 10.2967/jnumed.118.219493]
11 **Ronneberger O**, Fischer P, Brox T. U-Net: convolutional networks for biomedical image segmentation. In: Navab N, Hornegger J, Wells WM, Frangi AF, eds. mMedical Image Computing and Computer-Assisted Intervention–MICCAI 2015.Cha, Switzerland: Springer International Publishing; 2015:234-241
12 **Hong X**, Zan Y, Weng F, Tao W, Peng Q, Huang Q. Enhancing the Image Quality *via* Transferred Deep Residual Learning of Coarse PET Sinograms. *IEEE Trans Med Imaging* 2018; **37**: 2322-2332 [PMID: 29993685 DOI: 10.1109/TMI.2018.2830381]
13 **Orlhac F**, Boughdad S, Philippe C, Stalla-Bourdillon H, Nioche C, Champion L, Soussan M, Frouin F, Frouin V, Buvat I. A Postreconstruction Harmonization Method for Multicenter Radiomic Studies in PET. *J Nucl Med* 2018; **59**: 1321-1328 [PMID: 29301932 DOI: 10.2967/jnumed.117.199935]
14 **Kim K**, Wu D, Gong K, Dutta J, Kim JH, Son YD, Kim HK, El Fakhri G, Li Q. Penalized PET Reconstruction Using Deep Learning Prior and Local Linear Fitting. *IEEE Trans Med Imaging* 2018; **37**: 1478-1487 [PMID: 29870375 DOI: 10.1109/TMI.2018.2832613]
15 **Li W**, Liu H, Cheng F, Li Y, Li S, Yan J. Artificial intelligence applications for oncological positron emission tomography imaging. *Eur J Radiol* 2021; **134**: 109448 [PMID: 33307463 DOI: 10.1016/j.ejrad.2020.109448]
16 **Noortman WA**, Vriens D, Mooij CDY, Slump CH, Aarntzen EH, van Berkel A, Timmers HJLM, Bussink J, Meijer TWH, de Geus-Oei LF, van Velden FHP. The Influence of the Exclusion of Central Necrosis on [^{18}F]FDG PET Radiomic Analysis. *Diagnostics (Basel)* 2021; **11** [PMID: 34359379 DOI: 10.3390/diagnostics]
17 **Nensa F**, Demircioglu A, Rischpler C. Artificial Intelligence in Nuclear Medicine. *J Nucl Med* 2019; **60**: 29S-37S [PMID: 31481587 DOI: 10.2967/jnumed.118.220590]
18 **Hagendorff T**. The Ethics of AI Ethics: An Evaluation of Guidelines. *Minds & Machines* 2020; 30: 99-120 [DOI: 10.1007/s11023-020-09517-8]
19 **Aktolun C**. Artificial intelligence and radiomics in nuclear medicine: potentials and challenges. *Eur J Nucl Med Mol Imaging* 2019; **46**: 2731-2736 [PMID: 31673788 DOI: 10.1007/s00259-019-04593-0]
20 **Gajera J**, Knipe H. Federated learning. Reference article, Radiopaedia.org. (accessed on 19 Apr 2022) [DOI: 10.53347/rID-81590]

World Journal of Radiology

Submit a Manuscript: https://www.f6publishing.com

World J Radiol 2022 June 28; 14(6): 155-164

DOI: 10.4329/wjr.v14.i6.155

ISSN 1949-8470 (online)

ORIGINAL ARTICLE

Prospective Study

Evaluation of the dual vascular supply patterns in ground-glass nodules with a dynamic volume computed tomography

Chao Wang, Ning Wu, Zhuang Zhang, Lai-Xing Zhang, Xiao-Dong Yuan

Specialty type: Radiology, nuclear medicine and medical imaging

Provenance and peer review: Unsolicited article; Externally peer reviewed.

Peer-review model: Single blind

Peer-review report's scientific quality classification

Grade A (Excellent): 0
Grade B (Very good): B
Grade C (Good): C
Grade D (Fair): D
Grade E (Poor): 0

P-Reviewer: Esch M, Germany; Konovalov AB, Russia

Received: December 2, 2021
Peer-review started: December 2, 2021
First decision: April 8, 2022
Revised: April 20, 2022
Accepted: June 16, 2022
Article in press: June 16, 2022
Published online: June 28, 2022

Chao Wang, Zhuang Zhang, Lai-Xing Zhang, Department of Graduate, Hebei North University, Zhangjiakou 075000, Hebei Province, China

Ning Wu, Xiao-Dong Yuan, Department of Radiology, The Eighth Medical Center of the People's Liberation Army General Hospital, Beijing 100091, China

Corresponding author: Xiao-Dong Yuan, MD, PhD, Chief Doctor, Professor, Department of Radiology, The Eighth Medical Center of the People's Liberation Army General Hospital, No. 17 Heishanhu Road, Haidian District, Beijing 100091, China. yuanxiaodongzj@163.com

Abstract

BACKGROUND

In recent years, the detection rate of ground-glass nodules (GGNs) has been improved dramatically due to the popularization of low-dose computed tomography (CT) screening with high-resolution CT technique. This presents challenges for the characterization and management of the GGNs, which depends on a thorough investigation and sufficient diagnostic knowledge of the GGNs. In most diagnostic studies of the GGNs, morphological manifestations are used to differentiate benignancy and malignancy. In contrast, few studies are dedicated to the assessment of the hemodynamics, *i.e.*, perfusion parameters of the GGNs.

AIM

To assess the dual vascular supply patterns of GGNs on different histopathology and opacities.

METHODS

Forty-seven GGNs from 47 patients were prospectively included and underwent the dynamic volume CT. Histopathologic diagnoses were obtained within two weeks after the CT examination. Blood flow from the bronchial artery [bronchial flow (BF)] and pulmonary artery [pulmonary flow (PF)] as well as the perfusion index (PI) = [PF/(PF + BF)] were obtained using first-pass dual-input CT perfusion analysis and compared respectively between different histopathology and lesion types (pure or mixed GGNs) and correlated with the attenuation values of the lesions using one-way ANOVA, student's *t* test and Pearson correlation analysis.

RESULTS

Of the 47 GGNs (mean diameter, 8.17 mm; range, 5.3-12.7 mm), 30 (64%) were

carcinoma, 6 (13%) were atypical adenomatous hyperplasia and 11 (23%) were organizing pneumonia. All perfusion parameters (BF, PF and PI) demonstrated no significant difference among the three conditions (all $P > 0.05$). The PFs were higher than the BFs in all the three conditions (all $P < 0.001$). Of the 30 GGN carcinomas, 14 showed mixed GGNs and 16 pure GGNs with a higher PI in the latter ($P < 0.01$). Of the 17 benign GGNs, 4 showed mixed GGNs and 13 pure GGNs with no significant difference of the PI between the GGN types ($P = 0.21$). A negative correlation ($r = -0.76$, $P < 0.001$) was demonstrated between the CT attenuation values and the PIs in the 30 GGN carcinomas.

CONCLUSION

The GGNs are perfused dominantly by the PF regardless of its histopathology while the weight of the BF in the GGN carcinomas increases gradually during the progress of its opacification.

Key Words: Ground-glass nodules; Tomography; X-ray computed; Lung cancer; Perfusion computed tomography; Dual blood supply

Core Tip: In this study, bronchial flow (BF) and pulmonary flow (PF) as well as perfusion index (PI) were obtained by using first-pass dual-input computed tomography perfusion analysis and compared respectively among different histopathological types and between pure and mixed ground-glass nodules (GGNs), then correlated with the attenuation values in forty-seven GGNs from 47 patients. We found that the GGNs are perfused dominantly by the PF regardless of histopathological types while the weight of the BF in the GGN carcinomas increases gradually during its opacification. Therefore, the PI may be a potentially useful biomarker for distinguishing indolent nodules from aggressive ones.

Citation: Wang C, Wu N, Zhang Z, Zhang LX, Yuan XD. Evaluation of the dual vascular supply patterns in ground-glass nodules with a dynamic volume computed tomography. *World J Radiol* 2022; 14(6): 155-164
URL: https://www.wjgnet.com/1949-8470/full/v14/i6/155.htm
DOI: https://dx.doi.org/10.4329/wjr.v14.i6.155

INTRODUCTION

In recent years, more and more ground-glass nodules (GGNs) have been detected due to the application of low-dose screening with high-resolution computed tomography (CT)[1]. The rapidly increasing GGN cases requires appropriate management which depends on a thorough investigation and sufficient knowledge of the GGNs. In most diagnostic studies of the GGNs, morphological factors or nodular characteristics are used to differentiate benignancy and malignancy[2-6]. On the other hand, studies of the solid lesions suggested that the information of CT perfusion is helpful in identification and treatment planning[7-13]. A few studies have quantitatively measured iodine concentration to assess the blood supply status of the GGNs with promising outcomes[14]. Furthermore, quantification of the dual blood supply from the pulmonary and bronchial artery, *i.e.*, the pulmonary flow (PF) and bronchial flow (BF) in lung disorders is recently achieved with the first-pass dual-input perfusion analysis at a dynamic volume CT, producing helpful information for differentiations and treatment planning[15]. Therefore, this prospective study was designed to determine the patterns of the dual vascular supply in the GGNs on different histopathology and attenuation values (HU).

MATERIALS AND METHODS

Study population

The prospective study was approved by the Institution Ethics Committee. Written informed consent was obtained from all patients. Between Jan 2014 and May 2018, 50 patients who had been previously evaluated by non-contrast CT and had GGNs with an axial diameter > 5 mm were prospectively enrolled into this study. All patients received histopathological diagnoses which were acquired by CT-guided puncture biopsy or surgical resection within 2 wk after the CT perfusion. Exclusion criteria were as follows: severe motion artifacts on the perfusion images that made it difficult to perform the perfusion analysis; patients receiving any antitumor treatment prior to the CT perfusion and contraindications to the administration of the iodinated contrast media. 1 patient with beam hardening artifacts

caused by the contrast agent in an ipsilateral subclavian vein and 2 patients who received antitumor treatment before the CT perfusion were excluded. Eventually, forty-seven patients (27 men and 20 women; mean age, 53 years; range, 35-69 years) with 47 GGNs were included in the statistical analysis.

The radiation dose of the dynamic CT was calculated from the dose–length product (DLP) listed in the exposure summary sheet generated by the CT equipment and multiplied by a k-factor of 0.014[16].

CT perfusion imaging technique

Before the CT examination, all patients performed breath training by holding their breath during the dynamic CT scan procedure and otherwise adopted regularly shallow breathing.

First, unenhanced helical CT of the entire thorax was performed to determine the location of the GGN. Then, the dynamic volume CT perfusion was performed at a 320-row multidetector CT (Aquilion ONE, Toshiba Medical Systems, Otawara, Japan). With a dual-head power injector, 50 mL of non-ionic contrast medium with an iodine concentration of 370 mgI/mL (Iopromide, Bayer Schering, Berlin, Germany) was injected at a flow rate of 5 mL/s, followed by 20 mL of saline solution at the same rate. Five seconds after the start of the bolus injection, 15 intermittent low-dose volume acquisitions were made with 2 s intervals with no table movement.

The dynamic contrast-enhanced volume CT protocol was performed with the following parameters: 80 kV tube voltage, 80 mA tube current, 0.5 s gantry rotation speed and 0.5 mm slice thickness. The 16 cm coverage included both the lung hilum and the GGN. The first two volumes were acquired before the contrast medium arrived in the pulmonary artery (PA) and served as the baseline. The duration of the breath hold was approximately 30 s. The raw data were reconstructed with adaptive iterative dose reduction and automatically produced 0.5 mm slice thickness and 0.5 mm spacing images, resulting in 320 images per volume and a total of 4800 images for the entire perfusion dataset.

Data post-processing and analysis

Post-processing was performed using perfusion software available on the CT equipment (Body Perfusion, dual-input maximum slope analysis, Toshiba Medical Systems, Otawara, Japan). The first step is volume registration. The registration is performed to correct for motion between the dynamic volumes and creates a registered volume series. The registered volumes were then loaded into the body perfusion analysis software.

Rectangular region of interests (ROIs) (mean area 1.0 cm^2) was manually placed in the pulmonary artery trunk and the aorta at the level of the hilum to generate the TDCs representing the PA input function and the bronchial artery input function, respectively. An elliptical ROI was placed in the left atrium and the peak time of the left atrium tunneled dialysis catheters (TDCs) was used to differentiate pulmonary circulation (before the peak time point) and bronchial circulation (after the peak time point) [15]. A freehand ROI was drawn to encompass the lesion to generate the TDC of the contrast medium's first-pass attenuation in the GGN. The perfusion analysis range was set from -700 HU to 50 HU to confine the perfusion analysis to the GGN or mixed GGN regions only and to ignore normal lung parenchyma. Finally, 512 × 512 matrix color-coded maps of the PF, BF and perfusion index [PI = PF/(PF + BF)] were generated automatically. For each lesion, measurements were repeated on all relevant 5.0-mm axial slices and then averaged to calculate the final value. Lesion opacity (mean HU) was measured on the non-contrast axial slice with the maximum lesion diameter using a freehand ROI closely encompassing the lesion and avoiding major vessels. This post-processing procedure was independently performed by two radiologists (**BLINDED**, with 13 and 11 years of experience, respectively in CT perfusion in the abdomen and chest). Each radiologist was blinded to the results of the other and the histopathological diagnoses. The final results were the average of the two observers. Inter-observer reproducibility was assessed for the PF, BF and PI as well as the lesion opacity (mean HU). The lesion type (pure GGN or mixed GGN) was independently determined by the two radiologists and by a third radiologist (**BLINDED**) if the results of the two radiologists were inconsistent.

The pure GGN was defined as a focal, slightly increased attenuation in lung without masking the underlying structures on the lung window images while the mixed GGN as a focal increased attenuation with solid components masking the underlying structures of pulmonary vessels[17].

Statistical analysis

Forty-seven GGNs were analyzed. The bronchial artery (BF) and pulmonary artery (PF) as well as the PI [= PF/ (PF+BF)] were compared respectively between the histopathologic types and the lesion types (pure GGNs or mixed GGNs) using one-way ANOVA and students' *t* test and correlated respectively with lesions' HU using Pearson correlation analysis. In addition, the BF and PF were compared by paired *t* test to determine the dominant blood flow in the GGNs. The inter-observer reproducibility of perfusion parameters (BF, PF and PI) and HU of GGNs were assessed using intraclass correlation coefficients (ICC). Statistical analysis was performed using commercially available software (SPSS, V13.0, IBM). A P value < 0.05 was considered to indicate a significant difference.

RESULTS

All patients showed good compliance with the CT perfusion procedure. No severe motion artifacts or adverse events occurred.

Of the 47 GGNs (mean diameter, 8.17 mm; range, 5.3-12.7 mm), 30 (64%) proved to be bronchioloalveolar cell carcinoma (BAC) (n = 24) or adenocarcinoma with predominant BAC component (n = 6), six (13%) atypical adenomatous hyperplasia and 11 (23%) organizing pneumonia. None of the three perfusion parameters demonstrated significant difference among the three histopathological types (Table 1). Of the 30 carcinomas GGNs, 14 showed mixed GGNs and 16 pure GGNs, with a greater PI in the latter (P < 0.01). Of the 17 benign GGNs, 4 showed mixed GGNs (including 1 atypical adenomatous hyperplasia and 3 organizing pneumonia) and 13 pure GGNs (including 5 atypical adenomatous hyperplasia and 8 organizing pneumonia) with no significant difference of the PI between the GGN types (P = 0.21). Of the 30 cancerous GGNs, the lesions' HU demonstrated mild negative correlation with the PF (r = -0.558, P = 0.001) while mild positive correlation with the BF (r = 0.565, P = 0.001). The PI demonstrates moderate negative correlation with the HU (r = -0.76, P < 0.001). No correlation between the perfusion parameters and the HU was revealed in the other two diseases (all P > 0.05).

Perfusion parameters were visualized by color maps and fused onto the original axial CT images. Representative perfusion color maps are shown in Figure 1 and Figure 2. Statistical results of the perfusion parameters derived from dual-input computed tomography perfusion are listed in Table 1 and shown in Figures 3-5. ICC (0.94, 95%CI: 0.93-0.95) demonstrated that the reproducibility between the two observers is good.

The dynamic volume CT perfusion protocol was identical for all 47 cases. The CT dose DLP = 324.8 mGy cm or 4.55 mSv (k = 0.014).

DISCUSSION

The PF and the BF, *i.e.*, the dual vascular supply was revealed in lung cancer through post-mortem microarteriography in the early 1970s[18]. Since then, the BF in lung cancer was confirmed by many reports and broncho angiography studies[19]. In contrast, PF in lung cancer was rarely reported until recently with an *in vivo* evaluation of the dual vascular supply in lung cancer and was achieved by using a dynamic contrast-enhanced volume CT[20] which reported a dominant BF along with a subordinate PF in solid cancerous nodules. In the present investigation, however, we revealed a dominant PF along with a subordinate BF in the GGN carcinomas. In addition, we revealed that with the increase of the lesion opacity, the weight of the PF in the total blood flow of the GGN carcinomas decreases while the weight of the BF increases. Thus, we would like to provide an interpretation of our findings combining with the findings of the previous reports as the following: During the progress of the lung adenocarcinoma from a pure GGN to a mixed GGN then to a solid nodule[21,22], the PF dominant perfusion pattern may gradually reverse to the BF dominant perfusion pattern. In contrast to solid nodular carcinoma, GGN carcinoma are supposed to be indolent, which allows long-term follow-up of their morphological changes for treatment planning[23-25]. Our findings on the increasing weight of the BF in GGNs during its opacification suggest that the PI which represents the weight of the BF in the total blood supply (BF + PF) may be a potentially useful biomarker for distinguishing indolent nodules from active ones.

Though the dual vascular supply patterns of the GGNs were determined in the current investigation, it cannot help differentiate GGNs between benignancy and malignancy because none of the three perfusion parameters (PF, BF and PI) showed significant difference between benign and malignant GGNs. Nevertheless, the feature of the PF dominant perfusion in the GGN carcinomas may have two important clinical implications: (1) Bronchial arterial chemoembolization may not be suitable for the treatment of a GGN carcinoma; and (2) radiation therapy may not be suitable for the treatment of a GGN carcinoma. The reason for the former is self-evident. The reason for the latter is because the PF dominant perfusion indicates a low level of oxygenation in the GGN carcinoma resulting in a low level of radiosensitivity[20,26].

It was reported that the pure GGNs are difficult to be distinguished morphologically between malignancy and benignancy[27]; however, the mixed GGNs tend to be a malignant one[28,29]. During a long-term CT follow-up of an adenocarcinoma in the lung, the typical case may be a pure GGN at the very beginning then gradually changing into a mixed GGN and a solid nodule at last[30,31]. Therefore, it strongly suggests an adenocarcinoma when a pure GGN gradually changed into a mixed one during follow-up. According to the current investigation, a pure GGN carcinoma is mainly perfused by the PF while the weight of the BF increases in a mixed GGN. In addition, a solid carcinoma is mainly perfused by the BF according to the previous study[15,20,32]. These adaptive changes of the perfusion patterns may bring more oxygen to feed the growth of the GGN carcinomas because of a low oxygen level in the PF and a high oxygen level in the BF. However, the mechanism behind these changes is still unknown and needs to be investigated further.

Table 1 Results of histopathologic comparisons on the three perfusion parameters

Parameters	Histopathology	*n*	mean ± SD	95% CI		One way ANOVA
				Lower	Upper	
PF (mL/min/100 mL)	Carcinoma	30	135.54 ± 46.58	118.15	152.93	$P = 0.435$
	Adenomatous hyperplasia	6	121.51 ± 40.56	78.94	164.08	
	Organizing pneumonia	11	116.06 ± 43.15	87.07	145.05	
BF (mL/min/100 mL)	Carcinoma	30	33.21 ± 12.12	28.68	37.74	$P = 0.079$
	Adenomatous hyperplasia	6	26.55 ± 4.08	22.26	30.83	
	Organizing pneumonia	11	24.96 ± 9.90	18.31	31.61	
PI (100%)	Carcinoma	30	0.79 ± 0.09	0.75	0.82	$P = 0.657$
	Adenomatous hyperplasia	6	0.80 ± 0.07	0.73	0.88	
	Organizing pneumonia	11	0.81 ± 0.69	0.76	0.86	

PF: Pulmonary flow; BF: Bronchial flow; PI: Perfusion index.

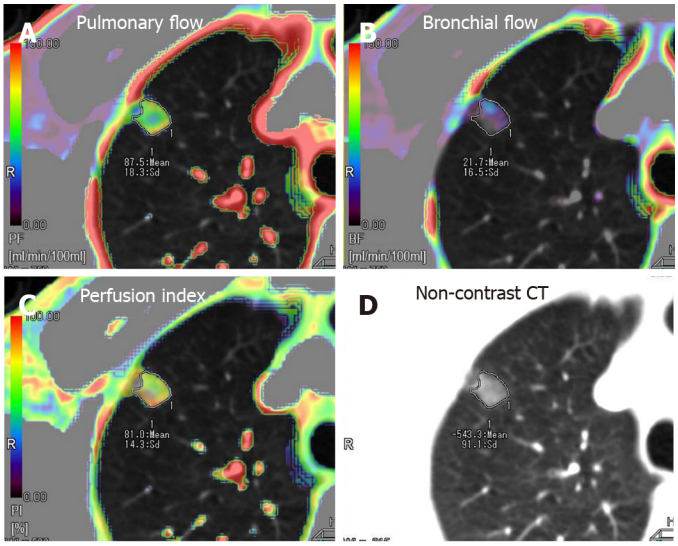

DOI: 10.4329/wjr.v14.i6.155

Figure 1 Axial colored perfusion maps in a 55-year-old male patient with pure ground-glass nodule carcinoma located in the right superior lung. Dominant pulmonary flow (PF) along with subordinate bronchial flow (BF) was observed in the pure ground-glass nodule. A: Axial colored perfusion map of PF; B: Axial colored perfusion map of BF; C: Axial colored perfusion map of perfusion index; D: Axial non-contrast computed tomography.

In this investigation, the perfusion analysis range was set from -700 HU to 50 HU to confine the perfusion analysis to the GGN or mixed GGN while ignore the normal lung parenchyma. In fact, the perfusion analysis range could be set individually according to an on-spot CT measurement of the GGN. To simplify and standardize the post-processing procedure, we adopted a fixed CT perfusion analysis range, *i.e.*, -700 HU to 50 HU in this study.

There are some limitations to this study. First, the relatively small sample size of this study will undermine the significance of our findings. Second, a relatively high radiation dose is an unavoidable limitation of perfusion CT though the total effective dose of each patient was controlled to comparable with a multiphasic CT procedure[33,34]. Third, although the difference of CT perfusion between the pure and mixed GGN carcinomas was investigated, the solid components and the pure components of the mixed GGN carcinomas were not evaluated separately because it's difficult to define the boundary of the two components. Fourth, our findings cannot help to differentiate between malignant and benign GGNs because no significant difference in perfusion parameters was revealed between them. However, the change regularity of the dual vascular supply patterns during the opacification of GGN carcinomas could help to better understand its biological behavior and therefore help to better manage it.

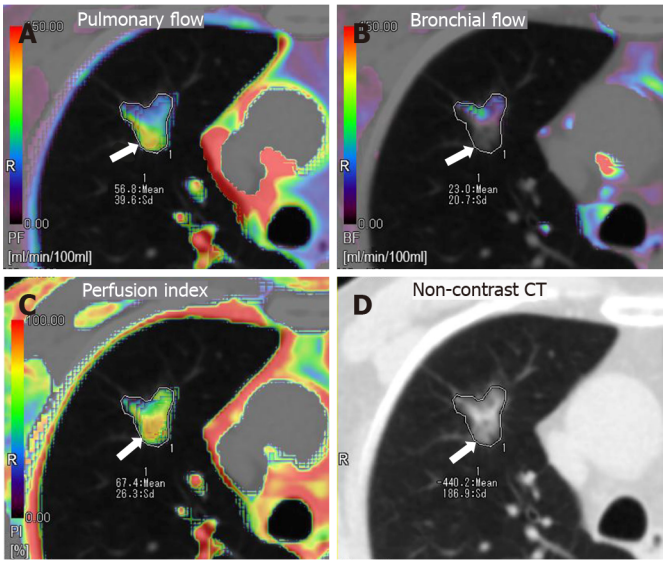

DOI: 10.4329/wjr.v14.i6.155 **Copyright** ©The Author(s) 2022.

Figure 2 Axial colored perfusion maps in a 72-year-old male patient with mixed ground-glass nodule carcinoma located in the right superior lung. The perfusion is heterogeneous throughout the lesion. Pulmonary flow (PF) is globally dominant, especially in the dorsal part of the lesion (arrow), which corresponds to the lower attenuation region of the mixed ground-glass nodule. A: Axial colored perfusion map of PF; B: Axial colored perfusion map of bronchial flow; C: Axial colored perfusion map of perfusion index; D: Axial non-contrast computed tomography.

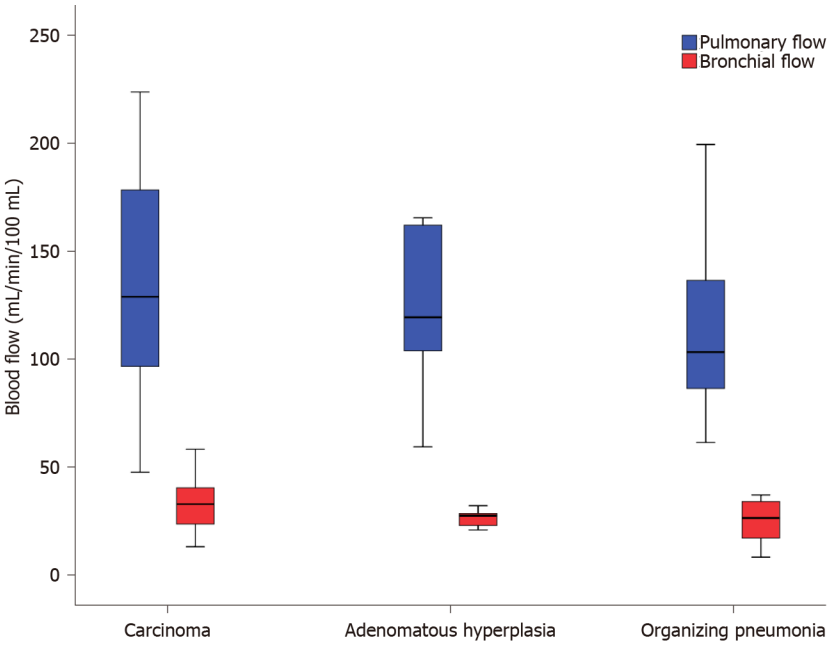

DOI: 10.4329/wjr.v14.i6.155 **Copyright** ©The Author(s) 2022.

Figure 3 Box plot of perfusion parameters demonstrates dominant Pulmonary flow (PF) along with relatively low bronchial flow (BF) in carcinoma (*n* = 30), atypical adenomatous hyperplasia (*n* = 6) and organizing pneumonia (*n* = 11).

CONCLUSION

In conclusion, the GGNs are perfused dominantly by the PF regardless of its histopathology while the weight of the BF in the GGN carcinomas increases gradually during its opacification. The PI may be a potentially useful biomarker for distinguishing indolent nodules from aggressive ones.

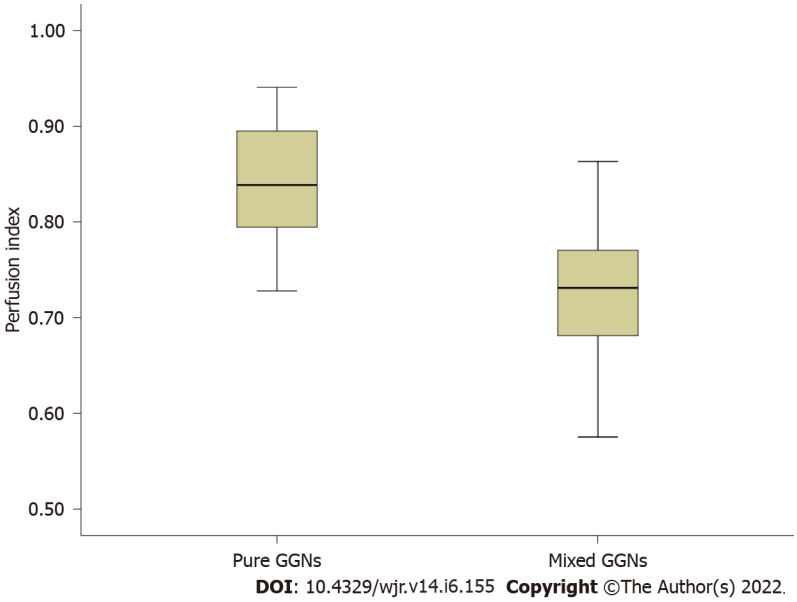

DOI: 10.4329/wjr.v14.i6.155

Figure 4 Box plot of perfusion index [= pulmonary flow/(pulmonary flow + bronchial flow)] demonstrates dominant pulmonary flow along with subordinate bronchial flow in pure ground-glass nodule carcinoma (*n* = 16) and a weakened pulmonary flow along with an enhanced bronchial flow in mixed ground-glass nodule carcinoma.

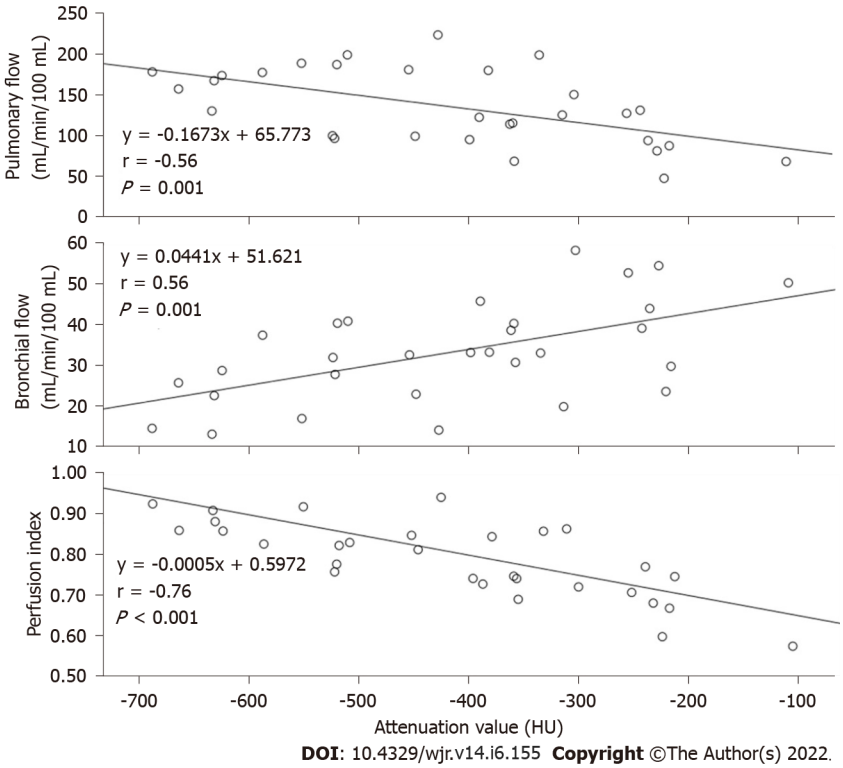

DOI: 10.4329/wjr.v14.i6.155

Figure 5 Plots of the Pearson correlation between the attenuation values of the ground-glass nodule carcinoma and the three perfusion parameters. The HU of the GGN carcinoma correlates negatively, positively and negatively with the pulmonary flow (PF), bronchial flow (BF) and the perfusion index (PI), respectively. A: Correlation between the HU of ground-glass nodule (GGN) carcinoma and PF; B: Correlation between the HU of GGN carcinoma and BF; C: Correlation between the HU of GGN carcinoma and PI.

ARTICLE HIGHLIGHTS

Research background

In recent years, the detection rate of ground-glass nodules (GGNs) has been improved dramatically due to the application of low-dose computed tomography (CT) screening and high-resolution CT. The rapidly increasing detection rate requires appropriate managements of the GGNs which depends on a thorough investigation and sufficient knowledge of the GGNs. In most diagnostic studies of the GGNs, morphological factors are used to differentiate benignancy and malignancy. However, evaluation of the dual vascular supply patterns in GGNs with a dynamic volume CT could provide more valuable information for identification and treatment planning.

Research motivation

Studies of the solid lesions suggested that the information of CT perfusion is helpful in identification and treatment planning. Furthermore, quantification of the dual blood supply from the pulmonary and bronchial artery, *i.e.*, the pulmonary flow (PF) and bronchial flow (BF) in lung disorders was recently achieved with a dynamic volume CT and the first-pass dual-input perfusion analysis producing helpful information for differentiations and treatment planning. Based on this, our study is devoted to the assessment of the dual blood supply pattern of GGNs by dynamic CT to provide more valuable information for differentiations and treatment planning.

Research objectives

To assess the dual vascular supply patterns of GGNs with regard to different histopathology and opacities using a dynamic volume CT.

Research methods

In this prospective study, 47 GGNs from 47 patients were included and underwent the dynamic volume CT. Histopathologic diagnoses were obtained within two weeks after the CT examination. BF and PF as well as the perfusion index [(PI) = PF/ (PF+BF)] were obtained using first-pass dual-input CT perfusion analysis and compared respectively between different histopathology and lesion types (pure or mixed GGN) and correlated with the attenuation values of the lesions, using one-way ANOVA, student's *t* test and Pearson correlation analysis.

Research results

Forty-seven GGNs including three histopathological types (30 carcinoma, 6 atypical adenomatous hyperplasia and 11 organizing pneumonia). All perfusion parameters (BF, PF and PI) demonstrated no significant difference among the three conditions (all $P > 0.05$). The PFs were higher than the BFs in all the three conditions (all $P < 0.001$). Of the 30 GGN carcinomas, 14 showed mixed GGNs and 16 pure GGNs, with a higher PI in the latter ($P < 0.01$). A negative correlation ($r = -0.76$, $P < 0.001$) was demonstrated between the CT attenuation values and the PIs in the 30 GGN carcinomas.

Research conclusions

In conclusion, the GGNs are perfused dominantly by the PF regardless of its histopathology while the weight of the BF in the GGN carcinomas increases gradually during the progress of its opacification.

Research perspectives

Our future study will expand the GGNs sample size to further investigate potential difference of perfusion parameters between malignant and benign GGNs and to further confirm that the PI is a useful biomarker for distinguishing indolent GGNs carcinomas from aggressive ones.

FOOTNOTES

Author contributions: Yuan XD and Wu N designed the study; Wang C wrote the first draft of the manuscript; Zhang Z and Zhang LX collected the data; Wang C performed the literature search and analysis; Yuan XD and Wang C conducted the statistical analysis and polished the language; all authors participated in and approved the final manuscript.

Supported by the National Natural Science Foundation of China, No. 81671680.

Institutional review board statement: Our prospective study was approved by our institutional review board.

Informed consent statement: Written informed consents were obtained from all patients.

Conflict-of-interest statement: The authors of this manuscript having no conflicts of interest to disclose.

Data sharing statement: No additional data are available.

Country/Territory of origin: China

ORCID number: Chao Wang 0000-0003-3446-9045; Ning Wu 0000-0002-9307-3115; Zhuang Zhang 0000-0002-9270-8342; Lai-Xing Zhang 0000-0001-7034-8043; Xiao-Dong Yuan 0000-0003-1964-5098.

S-Editor: Zhang H
L-Editor: Filipodia CL
P-Editor: Zhang H

REFERENCES

1 **Tsutsui S**, Ashizawa K, Minami K, Tagawa T, Nagayasu T, Hayashi T, Uetani M. Multiple focal pure ground-glass opacities on high-resolution CT images: Clinical significance in patients with lung cancer. *AJR Am J Roentgenol* 2010; **195**: W131-W138 [PMID: 20651172 DOI: 10.2214/AJR.09.3828]
2 **Lee HY**, Choi YL, Lee KS, Han J, Zo JI, Shim YM, Moon JW. Pure ground-glass opacity neoplastic lung nodules: histopathology, imaging, and management. *AJR Am J Roentgenol* 2014; **202**: W224-W233 [PMID: 24555618 DOI: 10.2214/AJR.13.11819]
3 **Yang J**, Wang H, Geng C, Dai Y, Ji J. Advances in intelligent diagnosis methods for pulmonary ground-glass opacity nodules. *Biomed Eng Online* 2018; **17**: 20 [PMID: 29415726 DOI: 10.1186/s12938-018-0435-2]
4 **Hu H**, Wang Q, Tang H, Xiong L, Lin Q. Multi-slice computed tomography characteristics of solitary pulmonary ground-glass nodules: Differences between malignant and benign. *Thorac Cancer* 2016; **7**: 80-87 [PMID: 26913083 DOI: 10.1111/1759-7714.12280]
5 **Jiang B**, Takashima S, Miyake C, Hakucho T, Takahashi Y, Morimoto D, Numasaki H, Nakanishi K, Tomita Y, Higashiyama M. Thin-section CT findings in peripheral lung cancer of 3 cm or smaller: are there any characteristic features for predicting tumor histology or do they depend only on tumor size? *Acta Radiol* 2014; **55**: 302-308 [PMID: 23926233 DOI: 10.1177/0284185113495834]
6 **Meng Y**, Liu CL, Cai Q, Shen YY, Chen SQ. Contrast analysis of the relationship between the HRCT sign and new pathologic classification in small ground glass nodule-like lung adenocarcinoma. *Radiol Med* 2019; **124**: 8-13 [PMID: 30191447 DOI: 10.1007/s11547-018-0936-x]
7 **Zhang M**, Kono M. Solitary pulmonary nodules: evaluation of blood flow patterns with dynamic CT. *Radiology* 1997; **205**: 471-478 [PMID: 9356631 DOI: 10.1148/radiology.205.2.9356631]
8 **Lee YH**, Kwon W, Kim MS, Kim YJ, Lee MS, Yong SJ, Jung SH, Chang SJ, Sung KJ. Lung perfusion CT: the differentiation of cavitary mass. *Eur J Radiol* 2010; **73**: 59-65 [PMID: 19481401 DOI: 10.1016/j.ejrad.2009.04.037]
9 **Boll DT**, Merkle EM. Differentiating a chronic hyperplastic mass from pancreatic cancer: a challenge remaining in multidetector CT of the pancreas. *Eur Radiol* 2003; **13** Suppl 5: M42-M49 [PMID: 14989611 DOI: 10.1007/s00330-003-2100-8]
10 **Coolen J**, Vansteenkiste J, De Keyzer F, Decaluwé H, De Wever W, Deroose C, Dooms C, Verbeken E, De Leyn P, Vandecaveye V, Van Raemdonck D, Nackaerts K, Dymarkowski S, Verschakelen J. Characterisation of solitary pulmonary lesions combining visual perfusion and quantitative diffusion MR imaging. *Eur Radiol* 2014; **24**: 531-541 [PMID: 24173597 DOI: 10.1007/s00330-013-3053-1]
11 **Bellomi M**, Petralia G, Sonzogni A, Zampino MG, Rocca A. CT perfusion for the monitoring of neoadjuvant chemotherapy and radiation therapy in rectal carcinoma: initial experience. *Radiology* 2007; **244**: 486-493 [PMID: 17641369 DOI: 10.1148/radiol.2442061189]
12 **Li XS**, Fan HX, Fang H, Huang H, Song YL, Zhou CW. Value of whole-tumor dual-input perfusion CT in predicting the effect of multiarterial infusion chemotherapy on advanced non-small cell lung cancer. *AJR Am J Roentgenol* 2014; **203**: W497-W505 [PMID: 25341164 DOI: 10.2214/AJR.13.11621]
13 **Lin G**, Sui Y, Li Y, Huang W. Diagnostic and prognostic value of CT perfusion parameters in patients with advanced NSCLC after chemotherapy. *Am J Transl Res* 2021; **13**: 13516-13523 [PMID: 35035693]
14 **Liu G**, Li M, Li G, Li Z, Liu A, Pu R, Cao H, Liu Y. Assessing the Blood Supply Status of the Focal Ground-Glass Opacity in Lungs Using Spectral Computed Tomography. *Korean J Radiol* 2018; **19**: 130-138 [PMID: 29354009 DOI: 10.3348/kjr.2018.19.1.130]
15 **Yuan X**, Zhang J, Ao G, Quan C, Tian Y, Li H. Lung cancer perfusion: can we measure pulmonary and bronchial circulation simultaneously? *Eur Radiol* 2012; **22**: 1665-1671 [PMID: 22415414 DOI: 10.1007/s00330-012-2414-5]
16 **Valentin J**; International Commission on Radiation Protection. Managing patient dose in multi-detector computed tomography(MDCT). ICRP Publication 102. *Ann ICRP* 2007; **37**: 1-79, iii [PMID: 18069128 DOI: 10.1016/j.icrp.2007.09.001]
17 **Godoy MC**, Naidich DP. Overview and strategic management of subsolid pulmonary nodules. *J Thorac Imaging* 2012; **27**: 240-248 [PMID: 22847591 DOI: 10.1097/RTI.0b013e31825d515b]

18 **Milne EN**. Circulation of primary and metastatic pulmonary neoplasms. A postmortem microarteriographic study. *Am J Roentgenol Radium Ther Nucl Med* 1967; **100**: 603-619 [PMID: 5230250 DOI: 10.2214/ajr.100.3.603]

19 **Luo L**, Wang H, Ma H, Zou H, Li D, Zhou Y. [Analysis of 41 cases of primary hypervascular non-small cell lung cancer treated with embolization of emulsion of chemotherapeutics and iodized oil]. *Zhongguo Fei Ai Za Zhi* 2010; **13**: 540-543 [PMID: 20677656 DOI: 10.3779/j.issn.1009-3419.2010.05.29]

20 **Yuan X**, Zhang J, Quan C, Cao J, Ao G, Tian Y, Li H. Differentiation of malignant and benign pulmonary nodules with first-pass dual-input perfusion CT. *Eur Radiol* 2013; **23**: 2469-2474 [PMID: 23793548 DOI: 10.1007/s00330-013-2842-x]

21 **Takashima S**, Maruyama Y, Hasegawa M, Yamanda T, Honda T, Kadoya M, Sone S. CT findings and progression of small peripheral lung neoplasms having a replacement growth pattern. *AJR Am J Roentgenol* 2003; **180**: 817-826 [PMID: 12591704 DOI: 10.2214/ajr.180.3.1800817]

22 **Min JH**, Lee HY, Lee KS, Han J, Park K, Ahn MJ, Lee SJ. Stepwise evolution from a focal pure pulmonary ground-glass opacity nodule into an invasive lung adenocarcinoma: an observation for more than 10 years. *Lung Cancer* 2010; **69**: 123-126 [PMID: 20478641 DOI: 10.1016/j.lungcan.2010.04.022]

23 **Mironova V**, Blasberg JD. Evaluation of ground glass nodules. *Curr Opin Pulm Med* 2018; **24**: 350-354 [PMID: 29634577 DOI: 10.1097/MCP.0000000000000492]

24 **Pedersen JH**, Saghir Z, Wille MM, Thomsen LH, Skov BG, Ashraf H. Ground-Glass Opacity Lung Nodules in the Era of Lung Cancer CT Screening: Radiology, Pathology, and Clinical Management. *Oncology (Williston Park)* 2016; **30**: 266-274 [PMID: 26984222]

25 **Lee GD**, Park CH, Park HS, Byun MK, Lee IJ, Kim TH, Lee S. Lung Adenocarcinoma Invasiveness Risk in Pure Ground-Glass Opacity Lung Nodules Smaller than 2 cm. *Thorac Cardiovasc Surg* 2019; **67**: 321-328 [PMID: 29359309 DOI: 10.1055/s-0037-1612615]

26 **Ohno Y**, Fujisawa Y, Koyama H, Kishida Y, Seki S, Sugihara N, Yoshikawa T. Dynamic contrast-enhanced perfusion area-detector CT assessed with various mathematical models: Its capability for therapeutic outcome prediction for non-small cell lung cancer patients with chemoradiotherapy as compared with that of FDG-PET/CT. *Eur J Radiol* 2017; **86**: 83-91 [PMID: 28027771 DOI: 10.1016/j.ejrad.2016.11.008]

27 **Kim HY**, Shim YM, Lee KS, Han J, Yi CA, Kim YK. Persistent pulmonary nodular ground-glass opacity at thin-section CT: histopathologic comparisons. *Radiology* 2007; **245**: 267-275 [PMID: 17885195 DOI: 10.1148/radiol.2451061682]

28 **Bach PB**, Silvestri GA, Hanger M, Jett JR; American College of Chest Physicians. Screening for lung cancer: ACCP evidence-based clinical practice guidelines (2nd edition). *Chest* 2007; **132**: 69S-77S [PMID: 17873161 DOI: 10.1378/chest.07-1349]

29 **Cha MJ**, Lee KS, Kim HS, Lee SW, Jeong CJ, Kim EY, Lee HY. Improvement in imaging diagnosis technique and modalities for solitary pulmonary nodules: from ground-glass opacity nodules to part-solid and solid nodules. *Expert Rev Respir Med* 2016; **10**: 261-278 [PMID: 26751340 DOI: 10.1586/17476348.2016.1141053]

30 **Sawada S**, Yamashita N, Sugimoto R, Ueno T, Yamashita M. Long-term Outcomes of Patients With Ground-Glass Opacities Detected Using CT Scanning. *Chest* 2017; **151**: 308-315 [PMID: 27435815 DOI: 10.1016/j.chest.2016.07.007]

31 **Bueno J**, Landeras L, Chung JH. Updated Fleischner Society Guidelines for Managing Incidental Pulmonary Nodules: Common Questions and Challenging Scenarios. *Radiographics* 2018; **38**: 1337-1350 [PMID: 30207935 DOI: 10.1148/rg.2018180017]

32 **Nguyen-Kim TD**, Frauenfelder T, Strobel K, Veit-Haibach P, Huellner MW. Assessment of bronchial and pulmonary blood supply in non-small cell lung cancer subtypes using computed tomography perfusion. *Invest Radiol* 2015; **50**: 179-186 [PMID: 25500892 DOI: 10.1097/RLI.0000000000000124]

33 **Tsai HY**, Tung CJ, Yu CC, Tyan YS. Survey of computed tomography scanners in Taiwan: dose descriptors, dose guidance levels, and effective doses. *Med Phys* 2007; **34**: 1234-1243 [PMID: 17500455 DOI: 10.1118/1.2712412]

34 **Galanski M**, Nagel HD, Stamm G. [Results of a federation inquiry 2005/2006: pediatric CT X-ray practice in Germany]. *Rofo* 2007; **179**: 1110-1111 [PMID: 17955412 DOI: 10.1055/s-2007-992844]

World Journal of Radiology

Submit a Manuscript: https://www.f6publishing.com

World J Radiol 2022 June 28; 14(6): 165-176

DOI: 10.4329/wjr.v14.i6.165

ISSN 1949-8470 (online)

ORIGINAL ARTICLE

Prospective Study

Do preoperative pancreatic computed tomography attenuation index and enhancement ratio predict pancreatic fistula after pancreaticoduodenectomy?

Senthil Gnanasekaran, Satish Durgesh, Ramprakash Gurram, Raja Kalayarasan, Biju Pottakkat, M Rajeswari, Bheemanathi Hanuman Srinivas, A Ramesh, Jayaprakash Sahoo

Specialty type: Radiology, nuclear medicine and medical imaging

Provenance and peer review: Invited article; Externally peer reviewed.

Peer-review model: Single blind

Peer-review report's scientific quality classification

Grade A (Excellent): 0
Grade B (Very good): B
Grade C (Good): 0
Grade D (Fair): 0
Grade E (Poor): E

P-Reviewer: Bencini L, Italy; Yang F, China
A-Editor: Morozov S

Received: January 29, 2022
Peer-review started: January 29, 2022
First decision: April 10, 2022
Revised: April 26, 2022
Accepted: June 20, 2022
Article in press: June 20, 2022
Published online: June 28, 2022

Senthil Gnanasekaran, Satish Durgesh, Ramprakash Gurram, Raja Kalayarasan, Biju Pottakkat, Department of Surgical Gastroenterology, Jawaharlal Institute of Postgraduate Medical Education and Research, Puducherry 605006, India

M Rajeswari, Department of Biostatistics, Jawaharlal Institute of Postgraduate Medical Education and Research, Puducherry 605006, India

Bheemanathi Hanuman Srinivas, Department of Pathology, Jawaharlal Institute of Postgraduate Medical Education and Research, Puducherry 605006, India

A Ramesh, Department of Radiodiagnosis, Jawaharlal Institute of Postgraduate Medical Education and Research, Puducherry 605006, India

Jayaprakash Sahoo, Department of Endocrinology, Jawaharlal Institute of Postgraduate Medical Education and Research, Puducherry 605006, India

Corresponding author: Raja Kalayarasan, DNB, MCh, MS, Additional Professor, Department of Surgical Gastroenterology, Jawaharlal Institute of Postgraduate Medical Education and Research, Room No. 5442, 4th Floor, Super Specialty Block, Puducherry-605006, India. kalayarasanraja@yahoo.com

Abstract

BACKGROUND

The commonly used predictors of clinically relevant postoperative pancreatic fistula (CR-POPF) following pancreaticoduodenectomy (PD) have subjective assessment components and can be used only in the postoperative setting. Also, the available objective predictors based on preoperative cross-sectional imaging were not prospectively studied.

AIM

To evaluate the accuracy of the pancreatic attenuation index (PAI) and pancreatic enhancement ratio (PER) for predicting CR-POPF following PD and its correlation with pancreatic fat fraction and fibrosis.

METHODS

A prospective observational study included patients who underwent PD for benign and malignant pathology of the periampullary region or pancreatic head between February 2019 and February 2021. Patients undergoing extended or total pancreatectomy and those with severe atrophy of pancreatic tissue or extensive parenchymal calcifications in the pancreatic head and neck precluding calculation of PAI and PER were excluded from the study. Preoperatively PAI was measured in the neck of the pancreas by marking regions of interest (ROI) in the non-contrast computed tomography (CT), and PER was measured during the contrast phase of the CT abdomen. Also, the fibrosis score and fat fraction of the pancreatic neck were assessed during the histopathological examination. Demographic, clinical and preoperative radiological indices (PAI, PER) were evaluated to predict CR-POPF. Preoperative pancreatic neck CT indices were correlated with the histopathological assessment of fat fraction and fibrosis.

RESULTS

Of the 70 patients who underwent PD, 61 patients fulfilling the inclusion criteria were included in the analysis. The incidence of CR-POPF was 29.5% (18/61). PAI had no association with the development of CR-POPF. Of the preoperative parameters, PER (mean ± standard deviation [SD]) was significantly lower in patients developing CR-POPF (0.58 ± 0.20 *vs* 0.81 ± 0.44, $P = 0.006$). The area under the curve for the PER was 0.661 (95%CI: 0.517-0.804), which was significant ($P = 0.049$). PER cut-off of 0.673 predicts CR-POPF with 77.8% sensitivity and 55.8% specificity. PAI and PER had a weak negative correlation (Strength-0.26, $P = 0.037$). Also, PER showed a moderately positive correlation with fibrosis (Strength 0.50, $P < 0.001$). Patients with CR-POPF had a significantly higher incidence of the intraabdominal abscess (50% *vs* 2.3%, $P < 0.001$), delayed gastric emptying (83.3% *vs* 30.2, $P < 0.001$), and prolonged mean (± SD) postoperative hospital stay (26.8 ± 13.9 *vs* 9.6 ± 3.6, $P = 0.001$).

CONCLUSION

PER exhibited good accuracy in predicting the development of CR-POPF. PER additionally showed a good correlation with PAI and fibrosis scores and may be used as an objective preoperative surrogate for assessing pancreatic texture. However, ROI-based PAI did not show any association with CR-POPF and pancreatic fat fraction.

Key Words: Pancreatic fistula; Minimally invasive; Pancreaticoduodenectomy; Pancreatic cancer; Neoplasms; Computed tomography

Core Tip: The prospective observational study evaluated the accuracy of the pancreatic computed tomography indices in predicting clinically relevant pancreatic fistula after pancreaticoduodenectomy. Though the predictive accuracy of pancreatic attenuation index (PAI) was low, pancreatic enhancement ratio (PER) exhibited good accuracy in predicting the development of clinically relevant postoperative pancreatic fistula (CR-POPF). Also, PER showed a statistically significant weak negative correlation with PAI and moderately positive correlation with fibrosis scores suggesting that PER may be an objective preoperative surrogate for assessing pancreatic texture. Preoperative quantification of PER can improve the risk stratification and management of patients at high risk of CR-POPF.

Citation: Gnanasekaran S, Durgesh S, Gurram R, Kalayarasan R, Pottakkat B, Rajeswari M, Srinivas BH, Ramesh A, Sahoo J. Do preoperative pancreatic computed tomography attenuation index and enhancement ratio predict pancreatic fistula after pancreaticoduodenectomy? *World J Radiol* 2022; 14(6): 165-176
URL: https://www.wjgnet.com/1949-8470/full/v14/i6/165.htm
DOI: https://dx.doi.org/10.4329/wjr.v14.i6.165

INTRODUCTION

Pancreaticoduodenectomy (PD) has been established as the standard surgical treatment for resectable pancreatic head cancer and periampullary tumors. Advances in surgical technology and perioperative care have reduced PD-related mortality from roughly 20% to less than 5%[1]. But the morbidity following a PD continues to remain high[2]. Hence, the focus has shifted to make PD a less morbid procedure. The most feared consequence of PD is postoperative pancreatic fistula (POPF)[1,2]. POPF is frequently linked to a lengthy and challenging hospital stay that imposes a significant social and

financial burden. Despite numerous novel perioperative therapies, there has been no substantial reduction in reported POPF rates[2,3].

The implications of identifying patients at risk of clinically relevant POPF (CR-POPF) are manifold. To begin, we can tailor surgical procedures to high-risk factors by making modifications that have been demonstrated to reduce the occurrence of CR-POPF. Second, high-risk patients can be closely assessed for the need for early intervention to avoid the disastrous consequences of POPF. Finally, it helps identify low-risk patients in whom the enhanced recovery after surgery (ERAS) pathway may be implemented confidently. Commonly used predictive models for POPF, such as the Fistula Risk Score (FRS), modified FRS, and Day 1 Drain Fluid Amylase estimation, can be used only in the postoperative setting[4-6]. Attenuation and enhancement patterns of pancreatic parenchyma on computed tomography (CT) were studied as preoperative predictors of CR-POPF[7-11]. While pancreatic attenuation index (PAI) can quantify pancreatic fat, pancreatic enhancement ratio (PER) has been correlated with pancreatic fibrosis. Therefore, the presence of a higher preoperative mean PER and lower PAI can be considered protective against the development of CR-POPF after PD[7-11]. However, the predictive accuracy of these indices for CR-POPF was not prospectively studied. Also, the distribution of fat and fibrosis within the pancreas varies, with pancreatic neck fat and fibrosis assuming relevance since it is the site of anastomosis, which previous studies have not addressed. Also, no previous research has prospectively correlated preoperative PAI and PER with histological pancreatic fat fraction and fibrosis, particularly in the neck. The present study aims to calculate the accuracy of the pancreatic neck PAI and PER in predicting CR-POPF and its correlation with histological pancreatic neck fat fraction and fibrosis scoring.

MATERIALS AND METHODS

Patient selection

Patients above 18 years of age who underwent elective PD for both benign and malignant pathology involving periampullary and pancreatic head from February 2019 to February 2021 and consented to participate were assessed for inclusion in the prospective observational study. Patients undergoing extended or total pancreatectomy and those with contraindication to undergo preoperative contrast-enhanced CT (CECT) or severe atrophy of pancreatic tissue or extensive parenchymal calcifications in the pancreatic head and neck precluding calculation of PAI and PER were excluded from the study. Also, patients who died in the immediate postoperative period (< 48 h) were excluded from the analysis. The study was approved by the Institute's scientific advisory and Ethics Committee (JIP/IEC/2018/500 dated 25-01-2019).

Preoperative CT protocol

As part of the routine evaluation, all patients underwent a pancreatic protocol CECT. Non-contrast and CECT of the abdomen and pelvis were performed using a 128 slice CT scanner (Somatom™ Definition Edge, M/s Siemens, Erlangen, Germany). Intravenous iodinated contrast media Iohexol with 300mg Iodine concentration (Contrapaque™ 300, JB chemicals and pharmaceuticals limited, India) was administered at a dose of 1.5 mL/ kg body weight at the rate of 3-4 mL/s followed by 20 mL of the saline chase at 3 mL/s. A dual head pressure injector (Medrad® Stellant D pedestal-mount with Certegra® Workstation) was used for contrast injection. Scans were triggered using the Bolus tracking technique when the threshold of 150HU was reached in the upper abdominal aorta. Contrast-enhanced scans included late arterial phase at 30-40 sec from the start of contrast injection (12-15 sec after bolus tracking), portal venous phase at 60-70 sec (25-30 secs delay after the arterial phase) and equilibrium phase at 3 min from contrast injection. The plain and contrast-enhanced images were reconstructed at 3 mm thickness and viewed in a picture archiving and communication system workstation using Centricity™ Universal Viewer Zero Footprint (GE, United States). On non-enhanced CT images, Hounsfield Units (HU) represents tissue density, while on contrast-enhanced CT images, it represents a measure of combination involving density and vascularity (18). Attenuation (HU) was measured in the neck of the pancreas and spleen, and attenuation values were calculated with regions of interest (ROI) of 0.2-0.3 cm^2. The mean of 3 ROI values obtained in the neck region divided by splenic attenuation gave the PAI of the pancreatic neck (Figure 1). PER was calculated in the neck of the pancreas as (EP-Pre)/(AP-Pre) (AP-arterial phase, pre-nonenhanced phase, EP-equilibrium phase)[11].

Surgery

All patients underwent pylorus resecting PD at the surgeon's discretion using an open, laparoscopic, or robot-assisted technique. All operations were performed by three qualified surgeons with extensive experience in pancreatobiliary surgery. Pancreaticojejunostomy (PJ) was performed using modified Blumgart or a modified invagination technique depending on the size of the pancreatic duct at the surgeon's discretion. Hepaticojejunostomy (HJ) was done 15 cm distal to PJ by Blumgart Kelly technique. Antecolic Gastrojejunostomy was done about 50 cm distal to the HJ. Two abdominal drains were placed, one in the subhepatic space near HJ and the other one adjacent to the PJ. Feeding

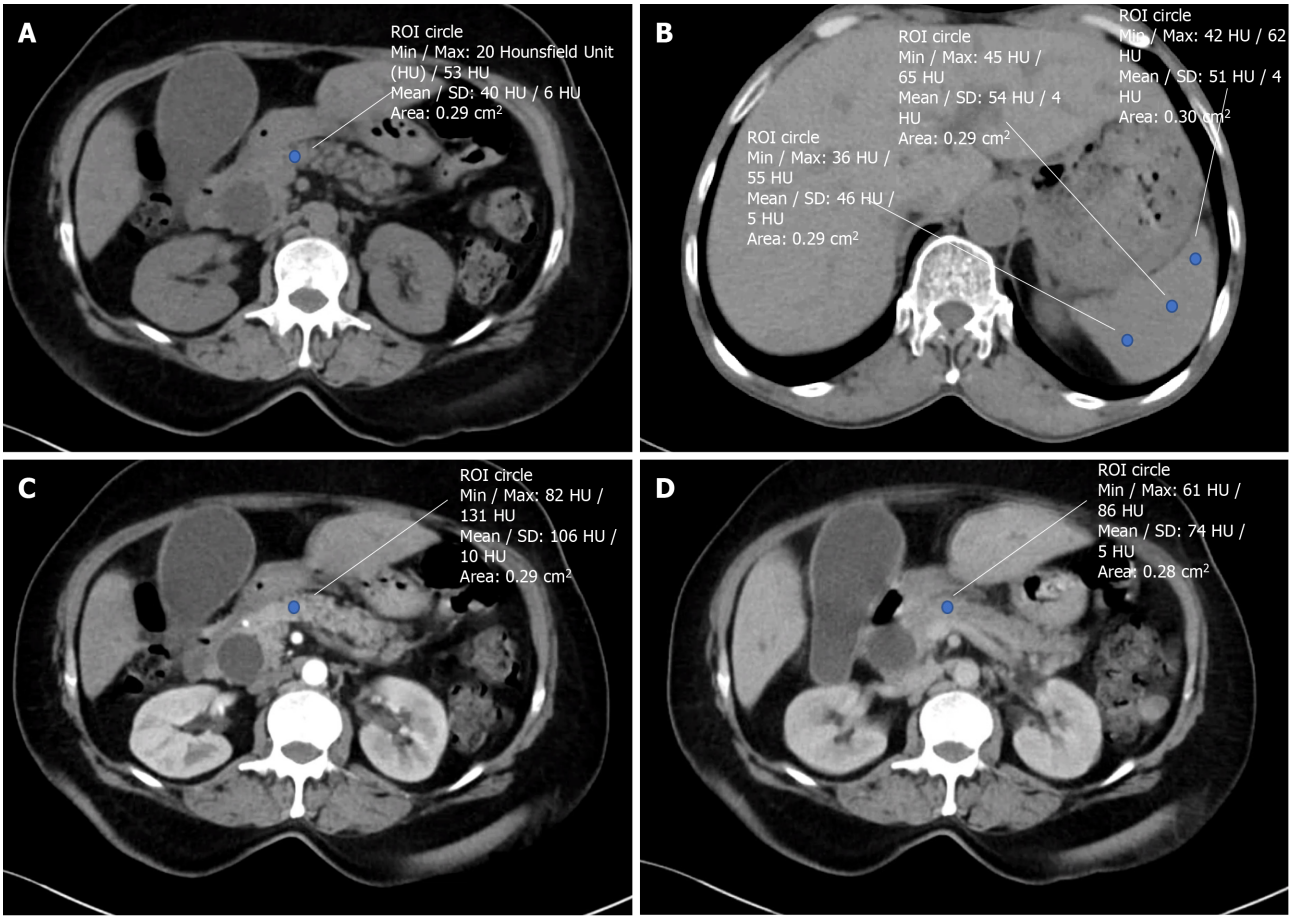

DOI: 10.4329/wjr.v14.i6.165

Figure 1 Calculation of preoperative radiological indices. A: Hounsfield unit (HU) of the pancreatic neck in plain phase; B: HU of the spleen in plain phase; C: HU of the pancreatic neck in the arterial phase; D: HU of the pancreatic neck in the equilibrium phase. ROI: Region of interest.

jejunostomy was done routinely for early postoperative enteral feeding.

Histopathological evaluation

A pancreatic neck tissue specimen was sent for histopathological evaluation. The pathologist, blinded to CT data and pancreatic texture, performed histological analysis. The existence of Langerhans' islets confirmed the Pancreatic tissue. Only tissue free of inflammatory lesions and calcifications was evaluated. The histologic pancreatic fat fraction was defined as the area ratio of pancreatic intraparenchymal fat to that of the total tissue times 100% (< 5%-mildly fatty; 5-15%-moderately fatty, > 15%-heavily fatty) using hematoxylin and eosin stain[12]. The degree of fibrosis was studied using Masson's trichome stain. The extent of intralobular and interlobular fibrosis was separately measured, and the total score (0-6) was calculated (Figure 2). According to the total score, fibrosis was classified as weak (score 0-3) and heavy (score 4-6)[13].

Outcome measures

The primary objective of this prospective observational study was to determine the predictive accuracy of PAI and PER for CR-POPF following PD. The patients' demographic and clinical data, including age, sex, body mass index, bilirubin level, preoperative biliary drainage, comorbidities (diabetes mellitus and hypertension), weight loss and radiological indices (PAI and PER) were collected to determine the preoperative factors predictive of CR-POPF. Also, the operative outcomes, including operative time, estimated blood loss, need for blood transfusion, pancreatic texture and postoperative complications, were compared between patients with and without CR-POPF. Delayed gastric emptying [DGE], Post pancreatectomy hemorrhage (PPH) and Postoperative pancreatic fistula [POPF] were graded as per the International Study Group for Pancreatic Surgery [ISGPS] definition[14-16]. To correlate preoperative CT indices (PAI and PER) with histopathological features, pancreatic neck fat fraction and fibrosis were measured in the pancreatic neck tissue specimen.

Statistical analysis

The statistical analysis was done using IBM SPSS Statistics for Windows, Version 28.0. (Armonk, NY,

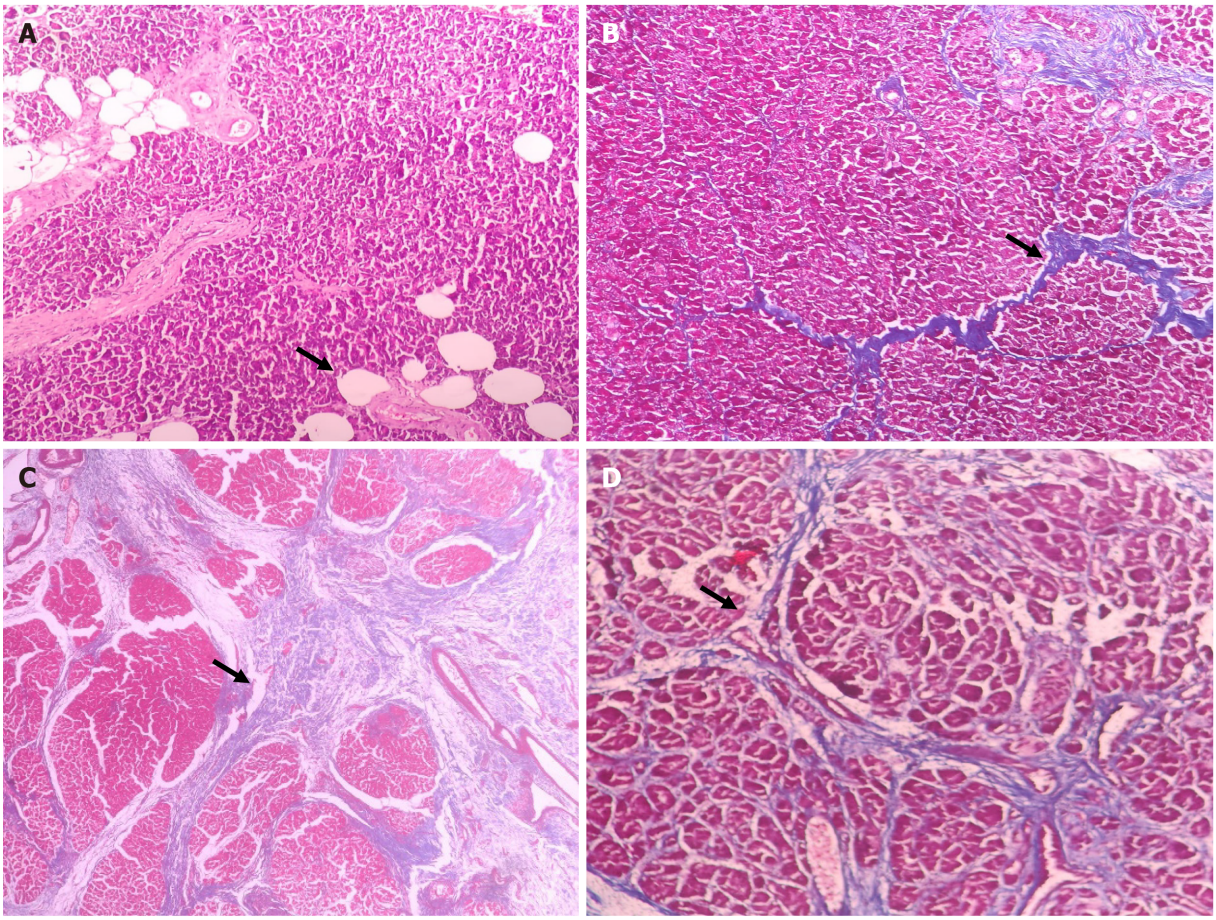

DOI: 10.4329/wjr.v14.i6.165

Figure 2 Histopathological evaluation of pancreatic neck fat fraction and fibrosis. A: Photomicrograph showing moderate fat inclusion (hematoxylin and eosin [H&E], × 100); B: Photomicrograph showing heavy intralobular fibrosis (Masson's trichome stain, H&E, × 100); C: Photomicrograph showing heavy interlobular fibrosis (Masson's trichome stain, × 40); D: Photomicrograph showing weak intra and interlobular fibrosis (Masson's trichome stain, × 200).

United States). The estimated sample size was calculated, anticipating an AUC of 0.75 for PER in predicting CR-POPF with 90% power and a 5% level of significance. The required sample size was calculated as 60. Both descriptive and inferential statistics were used to analyze the data. Baseline characteristics of the patients are presented by descriptive statistics. Categorical data (sex, clinical factors, presence or absence of DGE, CRPOPF, PPH, Intraabdominal abscess, pancreatic gland texture, pathological diagnosis) was described using percentages and frequencies and compared by using Fischer exact test or Chi-square test. The normality of continuous data was assessed by the Kolmogorov-Smirnov test. The normally distributed data were described by mean ± standard deviation (SD). Median and interquartile range was used for non-Gaussian data. Comparison of the continuous data (age, duct size, serum bilirubin) between the two groups was done by independent Student's *t*-test for parametric data and Mann-Whitney U-test for nonparametric data. The ability of PAI and PER to predict CR-POPF was assessed using receiver operating characteristic (ROC) analysis. A perfect test will have an AUC equaling 1. A 95% confidence interval was calculated and reported for the outcome measures. Statistical analysis was carried out at a 5% significance level, and $P < 0.05$ was considered statistically significant. The Pearson correlation coefficient (r) was used to examine the association of the histologic pancreatic fibrosis score and fat fraction with PAI and PER independently. A perfect positive correlation will show a value of +1, and a value of -1 indicates a perfect negative correlation.

RESULTS

Of the 70 patients who underwent PD during the study period, 61 patients fulfilling the inclusion criteria were included in the analysis. Five patients did not achieve the required ROI (0.2-0.3 cm^2), three patients who could not undergo histopathological analysis due to insufficient or other pathological changes in the sample and one patient who died during the immediate postoperative period were excluded from the analysis.

Preoperative predictive factors for CR-POPF

The overall incidence of CR-POPF in the study cohort was 29.5% (18/61). The demographic variables, history of weight loss, presence of comorbidities, preoperative hemoglobin, serum bilirubin and preoperative biliary drainage were comparable between groups with and without CR-POPF (Table 1). While PAI was similar between the two groups, the mean (± SD) PER was significantly lower in patients developing CR-POPF (0.58 ± 0.20 *vs* 0.81 ± 0.44, $P = 0.006$). The ROC analysis was done to determine the accuracy of PAI and PER in predicting CR-POPF (Figure 3). The area under the curve for the PAI was 0.461 (95%CI: 0.304-0.617), which was not significant ($P = 0.630$). At the same time, the area under the curve for the PER was 0.661 (95%CI: 0.517-0.804), which was significant ($P = 0.049$). We can predict whether a randomly chosen case will develop CR-POPF with a probability of 66.1%. With a cut-off of PER = 0.673, PER can predict those with CR-POPF with 77.8% sensitivity and 55.8% specificity (Figure 3).

Correlation between radiological indices (PAI, PER) and histopathological findings

There was no significant correlation between PAI and fat fraction or fibrosis score (Table 2). Pearson correlation coefficient between PER and fibrosis score was moderately positive and statistically significant with a strength of 0.504 and a P value of < 0.001. The positive correlation between PER and fibrosis score suggests that an increase in the intraparenchymal fibrosis results in the delayed pancreatic enhancement on CT, reflected as an increased PER. The correlation coefficient between PER and PAI was low negative and statistically significant, with a strength of -0.267 and a P-value of 0.037. The negative correlation between PER and PAI signifies that as the fibrosis increases, resulting in an increased delayed pancreatic enhancement, the fat fraction within the pancreas decreases, represented by a lower PAI.

Perioperative outcomes

The operative time, blood loss, intraoperative blood transfusion, surgical approach and pancreatic duct size was comparable between the two groups (Table 3). The proportion of patients with soft pancreas was significantly higher in the CR-POPF group. Postoperatively patients with CR-POPF had a significantly higher incidence of delayed gastric emptying (83.3% *vs* 30.2%, $P < 0.001$) and intra-abdominal abscess (50% *vs* 2.3%, $P < 0.001$). Also, Patients with CR-POPF had a prolonged postoperative hospital stay. There was no significant difference in the pancreatic fat fraction and fibrosis score between the two groups.

DISCUSSION

The present study documents the role of preoperative CT indices, especially PER, in predicting CR-POPF. Despite improved surgical techniques and perioperative management, PD remains a morbid procedure with a 30-50% estimated morbidity rate[1,2]. POPF is the critical cause of post-PD morbidity, and pancreatic texture has been reported as an important predictive parameter for POPF[17,18]. A soft pancreatic texture has been associated with an increased risk, while a firm pancreas protects against POPF. However, intraoperative assessment of gland consistency by the surgeon's digital palpation is highly subjective[18]. In recent years, laparoscopic and robotic approaches for PD have increased globally. Assessment of pancreatic texture during minimally invasive PD, especially the robotic approach, is challenging. Hence, parameters like acinar cell density and fibrosis score on histopathological examination were evaluated as objective criteria for pancreatic texture[19]. However, these parameters are not helpful for the preoperative prediction of POPF. Preoperative CR-POPF prediction using dependable parameters can assist in implementing intraoperative and postoperative measures to reduce CR-POPF-related morbidity. Hence, attempts have been made to correlate preoperative cross-sectional imaging (CECT and MRI) with pancreatic texture[7-11,20]. Most studies evaluating PAI and PER on the CECT abdomen were retrospective, which precludes assessment and correlation of pancreatic neck fat fraction and fibrosis[7-11].

PAI

The high fat fraction in the pancreas makes the pancreas softer, which might increase the risk of POPF following PD. Liver Attenuation Index is the widely used radiological index to measure liver fat fraction [21]. Similarly, Yardimci *et al*[22] proposed PAI as a simple tool to assess pancreatic fat fraction based on the study of 76 patients who underwent PD. The PAI cut-off value of 0.67 was valuable for risk calculation in their research. Other studies also reported the usefulness of PAI in assessing pancreatic fat fraction[7,8]. Although PAI was proposed as a simple tool that can be quickly evaluated, the lack of adequate external validation remains the primary impediment to its widespread adoption. In the present study, PAI was not useful for predicting CR-POPF. Also, PAI did not correlate with histological pancreatic fat fraction. On the other hand, PAI correlated negatively with PER, indicating an inverse relationship between pancreatic fat content with fibrosis and pancreatic texture. According to our analysis, PAI may not accurately reflect pancreas fat fraction and softness. However, the lack of predict-

Table 1 Comparison of demographic, clinical and preoperative radiological parameters between patients with and without clinically relevant postoperative pancreatic fistula

Parameter	CR-POPF, *n* = 18	No CR-POPF, *n* = 43	*P* value
Age in yr, mean ± SD	53.7 ± 10.8	54.7 ± 11.5	0.746
Sex, *n* (%)			
Male	10 (55.6)	28 (65.1)	0.567
Female	8 (44.4)	15 (34.9)	
BMI in kg/m^2, mean ± SD	21.1 ± 4.4	20.1 ± 3.9	0.388
Weight loss, *n* (%)	15 (83.3)	32 (74.4)	0.525
Comorbidities, *n* (%)	11 (61.1)	22 (51.2)	0.578
Hemoglobin in gm%, mean ± SD	10.7 ± 1.4	10.8 ± 1.5	0.735
Preoperative serum bilirubin (mg/dL), median (IQR)	2 (1.8-6)	3 (1-7)	0.848
Preoperative biliary drainage, *n* (%)	10 (55.6)	22 (51.2)	0.786
Pancreatic attenuation index, mean ± SD	0.8 ± 0.2	0.8 ± 0.2	0.741
Pancreatic enhancement ratio, mean ± SD	0.6 ± 0.2	0.8 ± 0.4	0.006

CR-POPF: Clinically relevant postoperative pancreatic fistula; gm: Gram; IQR: Inter quartile range; SD: Standard deviation.

Table 2 Correlation between preoperative radiological indices and histopathological pancreatic neck fat fraction and fibrosis

	Pancreatic attenuation index	Pancreatic enhancement ratio	Pancreatic fat fraction	Fibrosis score
Pancreatic attenuation index	-	-0.27 [a]	0.21	-0.20
Pancreatic enhancement ratio	-0.27[a]	-	-0.10	0.50 [b]
Pancreatic fat fraction	0.21	-0.10	-	-0.12
Fibrosis score	-0.20	0.50 [b]	-0.12	-

[a]Correlation is significant at the 0.05 level (2-tailed).
[b]Correlation is significant at the 0.01 level (2-tailed).

ability and correlation may be due to the small sample size and the underpowered study.

PER

An increase in the fibrosis of the pancreas makes the gland firmer, decreasing the incidence of POPF. It is technically straightforward to perform a pancreatoenteric anastomosis on a firmer gland. Maehira *et al* [9], in a retrospective analysis of 115 patients, reported that the pattern of pancreatic enhancement could be a reliable predictor for the development of CR-POPF. Also, Kang *et al*[11] documented that PER cut-off of 1.100 might be a valuable predictor for the risk of developing a CR-POPF following PD. In the present study, the PER cut-off value of 0.661 had a sensitivity of 78% and a specificity of 55% in predicting CR-POPF. Also, PER had a positive correlation with pancreatic fibrosis. The main drawback of using PER as a predictor for CR-POPF is that the perfusion of organs with injected contrast depends upon the patient's hemodynamic status, influencing the final indices values, unlike PAI, which is independent of contrast.

Correlation between the CT indices and Histopathological analysis

With pancreatic fibrosis known for the protection of CR-POPF and pancreatic fatty infiltration being a concern, it is prudent that radiological indices be correlated with histopathological findings to determine their predictive accuracy. While multiple studies have evaluated different CT parameters, a few have tried to link with histology. However, no previous studies have looked at both contrast and non-contrast indices and their relationship with pancreatic neck fat fraction and fibrosis. The present study results are similar to the study by Hashimoto *et al*[10], which reported a correlation between PER and pancreatic fibrosis. However, in contrast to the current study, bolus tracking was not used in their imaging protocol. Hence, the timing differences between the scan performance and arrival of injected contrast in the structures were not considered. Further, the iodine concentration of the contrast used

Table 3 Comparison of perioperative and pathological parameters between patients with and without clinically relevant postoperative pancreatic fistula

Parameter	CR-POPF, *n* = 18	No CR-POPF,*n* = 43	*P* value
Operative time in min, mean ± SD	521.9 ± 123	463.9 ± 101.2	0.275
Blood loss in mL, median (IQR)	550 (350-725)	475 (350-800)	0.830
Intraoperative blood transfusion, *n* (%)	6 (33.3)	17 (39.5)	0.775
Pancreatic texture, *n* (%)			
Firm	1 (5.6)	20 (47.6)	0.002
Soft	17 (94.4)	22 (52.4)	
Pancreatic duct size in mm, mean ± SD	2.8 ± 1.1	3.4 ± 1.6	0.169
Surgical approach, *n* (%)			
Open	9 (50)	24 (55.8)	
Laparoscopic	6 (33.3)	12 (27.9)	
Robot assisted	3 (16.7)	7 (16.3)	0.927
Delayed gastric emptying, *n* (%)	15 (83.3)	13 (30.2)	< 0.001
Postpancreatectomy hemorrhage, *n* (%)	3 (16.7)	4 (9.3)	0.662
Intra-abdominal abscess, *n* (%)	9 (50)	1 (2.3)	< 0.001
Hospital stay in d, mean ± SD	26.8 ± 13.9	9.6 ±.6	0.001
Pathology, *n* (%)			
Malignant	17 (94.4)	35 (81.4)	
Benign	1 (5.6)	8 (18.6)	0.259
Fat fraction, *n* (%)			
Absent	6 (33.3)	20 (46.5)	
Mild	9 (50.0)	17 (39.6)	0.669
Moderate	3 (16.7)	6 (13.9)	
Fibrosis score, *n* (%)			
Weak	16 (88.9)	27 (62.8)	
Heavy	2 (11.1)	16 (37.2)	0.063

CR-POPF: Clinically relevant postoperative pancreatic fistula; IQR: Inter quartile range; SD: Standard deviation.

could affect the magnitude of enhancement. Kang *et al*[11] reported that the CT enhancement ratio was a more powerful predictor of pancreatic fistula than fecal elastase-1 Levels. However, in contrast to the current study, their study was a retrospective analysis, with no reference standards of the pathological fibrosis data to correlate with the CT enhancement ratios.

Our study did not show any correlation of PAI with pancreatic fat fraction. Kim *et al*[12] reported a significant correlation between the PAI and histopathological fat fraction. However, the clinical parameter that was assessed was post PD glycemic control, unlike CR-POPF in our study. Though the study was able to show a positive correlation, it was a retrospective study, with a small sample size and lack of clarity on whether the histological fat fraction corresponded with the area of ROI. Hori *et al*[23] have recently shown that area-based assessment on unenhanced CT showed higher correlation and concordance with histopathology-based fat fraction in the pancreas than the ROI-based CT attenuation assessment. A few studies have reported the usefulness of MRI for analyzing pancreatic fat content[20]. As MRI is not widely available and routinely used for preoperative workup of patients undergoing PD, its use as a predictor tool for CR-POPF has a limited application. The different CT attenuation and enhancement values reported in the present study could be due to the calculation of CT indices precisely at the pancreatic neck. In contrast, previous studies measured randomly across the pancreas.

Limitations

Our study is limited by a few factors that require attention. Firstly, the small sample size may not

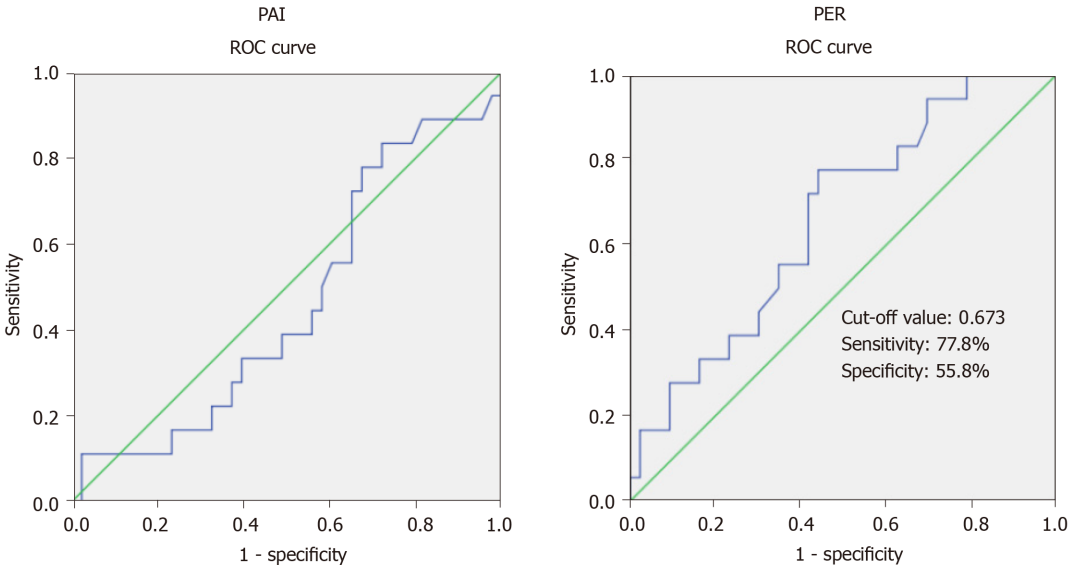

DOI: 10.4329/wjr.v14.i6.165

Figure 3 Receiver operating characteristic curve of the computed tomography indices for predicting clinically relevant postoperative fistula. The area under curve for the pancreatic attenuation index is 0.461 (95%CI: 0.304-0.617), which is not significant (P = 0.630). The area under curve for the pancreatic enhancement ratio is 0.661 (95%CI: 0.517-0.804), which is significant (P = 0.049). ROC: Receiver operating characteristic; PAI: Pancreatic attenuation index; PER: Pancreatic enhancement ratio.

represent the entire patient cohort. A future study with a larger sample size is needed to determine PAI's predictability accurately. The reliable prediction of CR-POPF preoperatively is challenging in patients undergoing PD as it is a mix of a heterogeneous population of patients subjected to different heterogeneous surgical approaches. In PD, with various reconstructive options available and each Institute and each surgeon adopting a technique of their own choice, creating a standardized operative technique is nearly impossible. A homogenous population of patients and standardized uniform surgical techniques are prerequisites for any preoperative prediction models to show good predictive ability, both of which are difficult to achieve in the case of PD. The patient characteristics, the surgeon's expertise and surgical techniques are vital in deciding the risk of a patient developing CR-POPF. With all these factors coming into play, it is expected that accurate preoperative prediction of CR-POPF is not always possible. Even if some studies show a single or group of parameters as predictors for CR-POPF, external validation might not offer the same result because of the factors mentioned above.

Nevertheless, identifying potential preoperative predictors for CR-POPF is a vital step in our journey to decrease the morbidity associated with PD. Our study failed to demonstrate any association of PAI with CR-POPF and postoperative fat fraction, which may be explained apart from the small sample size to the restrictive ROI. Area-based assessment for the pancreatic fat fraction in future studies may better correlate with histopathological fat fraction.

CONCLUSION

The PER showed good accuracy in predicting the development of CR-POPF and a PER ratio of 0.673 or below increased the likelihood of CR-POPF. The positive correlation of PER with fibrosis and negative correlation with PAI suggest that PER may be an objective surrogate for assessing pancreatic texture, especially in minimally invasive surgery, where pancreatic texture assessment could be challenging. ROI-based PAI has a poor prediction for CR-POPF and does not correlate with a pancreatic fat fraction or fibrosis scores. Preoperative quantification of PER can improve the risk stratification and management of patients at high risk of CR-POPF. A multi-center trial with a larger sample size is necessary to validate PAI and PER reliably.

ARTICLE HIGHLIGHTS

Research background

Postoperative pancreatic fistula is the critical cause of morbidity after pancreaticoduodenectomy. Identifying patients at risk of clinically relevant postoperative pancreatic fistula can potentially improve

clinical outcomes after pancreaticoduodenectomy.

Research motivation

Most of the available models to predict postoperative pancreatic fistula can be used only in the postoperative setting.

Research objectives

To calculate the accuracy of the pancreatic neck pancreatic attenuation index (PAI) and pancreatic enhancement ratio (PER) in predicting clinically relevant postoperative pancreatic fistula and its correlation with histological pancreatic neck fat fraction and fibrosis scoring.

Research methods

Patients who underwent pancreaticoduodenectomy for benign and malignant pathology of the periampullary region or pancreatic head between February 2019 and February 2021 were included in the prospective observational study. The PAI was measured in the neck of the pancreas by marking regions of interest in the preoperative non-contrast computed tomography (CT), and the PER was measured during the contrast phase of the CT abdomen. Preoperative pancreatic neck CT indices were correlated with histopathological evaluation of Fibrosis score and the fat fraction of the pancreatic neck and clinically relevant postoperative pancreatic fistula.

Research results

The PAI had no significant association with the development of clinically relevant postoperative pancreatic fistula (CR-POPF). However, PER was significantly lower in patients developing CR-POPF (0.58 ± 0.20 *vs* 0.81 ± 0.44, $P = 0.006$). Also, PER cut-off of 0.673 predicts CR-POPF with 77.8% sensitivity and 55.8% specificity. The PER showed a moderately positive correlation with fibrosis (Strength 0.50, $P < 0.001$).

Research conclusions

PER showed good accuracy in predicting CR-POPF. Also, PER showed a good correlation with fibrosis scores and may be used as an objective preoperative surrogate for assessing pancreatic texture.

Research perspectives

Quantifying PER on preoperative computed tomography can improve the risk stratification and management of patients at high risk of clinically relevant postoperative pancreatic fistula. Failure to demonstrate an association of PAI with clinically relevant postoperative pancreatic fistula and postoperative fat fraction suggests that area-based assessment for the pancreatic fat fraction may be better than the region of interest-based estimation.

FOOTNOTES

Author contributions: Gnanasekaran S and Kalayarasan R conceptualized the study; Durgesh S and Gurram R performed the research work; Rajeswari M performed the data analysis; Srinivas BH reviewed the histopathological slides for postoperative analysis; Ramesh A performed a preoperative radiological assessment of study participants; Durgesh S and Gurram R wrote the first draft of the manuscript; Gnanasekaran S, Kalayarasan R, Pottakkat B and Sahoo J gave intellectual input and critically revised the manuscript.

Institutional review board statement: The study was reviewed and approved by the institutional ethics committee (Human studies) of Jawaharlal Institute of Postgraduate Medical Education and Research (JIPMER), Puducherry, India (JIP/IEC/2018/500 dated 25-01-2019). The study protocol can be fully accessed at https://jipmer.edu.in/.

Informed consent statement: All study participants, or their legal guardian, provided written consent prior to study enrolment.

Conflict-of-interest statement: All authors of this manuscript have no financial relationships to disclose.

Data sharing statement: No additional data are available.

CONSORT 2010 statement: The authors have read the CONSORT 2010 Statement, and the manuscript was prepared and revised according to the CONSORT 2010 Statement.

Country/Territory of origin: India

ORCID number: Senthil Gnanasekaran 0000-0002-8639-5423; Satish Durgesh 0000-0001-8601-1576; Ramprakash Gurram 0000-0001-7106-2178; Raja Kalayarasan 0000-0003-4056-8672; Biju Pottakkat 0000-0002-8474-0270; M Rajeswari 0000-0003-1620-7359; BH Srinivas 0000-0002-9619-6719; A Ramesh 0000-0002-1404-6400; Jayaprakash Sahoo 0000-0002-8805-143X.

Corresponding Author's Membership in Professional Societies: Indian chapter of International Hepatopancreatobiliary Association, 563; Indian Association of Surgical Gastroenterology, K-65; International Hepatopancreatobiliary association, M02056.

S-Editor: Wang LL
L-Editor: Filipodia
P-Editor: Wang LL

REFERENCES

1 **Greenblatt DY**, Kelly KJ, Rajamanickam V, Wan Y, Hanson T, Rettammel R, Winslow ER, Cho CS, Weber SM. Preoperative factors predict perioperative morbidity and mortality after pancreaticoduodenectomy. *Ann Surg Oncol* 2011; **18**: 2126-2135 [PMID: 21336514 DOI: 10.1245/s10434-011-1594-6]

2 **Tzeng CW**, Katz MH, Fleming JB, Lee JE, Pisters PW, Holmes HM, Varadhachary GR, Wolff RA, Abbruzzese JL, Vauthey JN, Aloia TA. Morbidity and mortality after pancreaticoduodenectomy in patients with borderline resectable type C clinical classification. *J Gastrointest Surg* 2014; **18**: 146-55; discussion 155 [PMID: 24129825 DOI: 10.1007/s11605-013-2371-6]

3 **Berger AC**, Howard TJ, Kennedy EP, Sauter PK, Bower-Cherry M, Dutkevitch S, Hyslop T, Schmidt CM, Rosato EL, Lavu H, Nakeeb A, Pitt HA, Lillemoe KD, Yeo CJ. Does type of pancreaticojejunostomy after pancreaticoduodenectomy decrease rate of pancreatic fistula? *J Am Coll Surg* 2009; **208**: 738-47; discussion 747 [PMID: 19476827 DOI: 10.1016/j.jamcollsurg.2008.12.031]

4 **Callery MP**, Pratt WB, Kent TS, Chaikof EL, Vollmer CM Jr. A prospectively validated clinical risk score accurately predicts pancreatic fistula after pancreatoduodenectomy. *J Am Coll Surg* 2013; **216**: 1-14 [PMID: 23122535 DOI: 10.1016/j.jamcollsurg.2012.09.002]

5 **Kantor O**, Talamonti MS, Pitt HA, Vollmer CM, Riall TS, Hall BL, Wang CH, Baker MS. Using the NSQIP Pancreatic Demonstration Project to Derive a Modified Fistula Risk Score for Preoperative Risk Stratification in Patients Undergoing Pancreaticoduodenectomy. *J Am Coll Surg* 2017; **224**: 816-825 [PMID: 28408176 DOI: 10.1016/j.jamcollsurg.2017.01.054]

6 **Liu Y**, Li Y, Wang L, Peng CJ. Predictive value of drain pancreatic amylase concentration for postoperative pancreatic fistula on postoperative day 1 after pancreatic resection: An updated meta-analysis. *Medicine (Baltimore)* 2018; **97**: e12487 [PMID: 30235751 DOI: 10.1097/MD.0000000000012487]

7 **Tranchart H**, Gaujoux S, Rebours V, Vullierme MP, Dokmak S, Levy P, Couvelard A, Belghiti J, Sauvanet A. Preoperative CT scan helps to predict the occurrence of severe pancreatic fistula after pancreaticoduodenectomy. *Ann Surg* 2012; **256**: 139-145 [PMID: 22609844 DOI: 10.1097/SLA.0b013e318256c32c]

8 **Lim S**, Bae JH, Chun EJ, Kim H, Kim SY, Kim KM, Choi SH, Park KS, Florez JC, Jang HC. Differences in pancreatic volume, fat content, and fat density measured by multidetector-row computed tomography according to the duration of diabetes. *Acta Diabetol* 2014; **51**: 739-748 [PMID: 24671510 DOI: 10.1007/s00592-014-0581-3]

9 **Maehira H**, Iida H, Mori H, Kitamura N, Miyake T, Shimizu T, Tani M. Computed Tomography Enhancement Pattern of the Pancreatic Parenchyma Predicts Postoperative Pancreatic Fistula After Pancreaticoduodenectomy. *Pancreas* 2019; **48**: 209-215 [PMID: 30589830 DOI: 10.1097/MPA.0000000000001229]

10 **Hashimoto Y**, Sclabas GM, Takahashi N, Kirihara Y, Smyrk TC, Huebner M, Farnell MB. Dual-phase computed tomography for assessment of pancreatic fibrosis and anastomotic failure risk following pancreatoduodenectomy. *J Gastrointest Surg* 2011; **15**: 2193-2204 [PMID: 21948179 DOI: 10.1007/s11605-011-1687-3]

11 **Kang JH**, Park JS, Yu JS, Chung JJ, Kim JH, Cho ES, Yoon DS. Prediction of pancreatic fistula after pancreatoduodenectomy by preoperative dynamic CT and fecal elastase-1 Levels. *PLoS One* 2017; **12**: e0177052 [PMID: 28493949 DOI: 10.1371/journal.pone.0177052]

12 **Kim SY**, Kim H, Cho JY, Lim S, Cha K, Lee KH, Kim YH, Kim JH, Yoon YS, Han HS, Kang HS. Quantitative assessment of pancreatic fat by using unenhanced CT: pathologic correlation and clinical implications. *Radiology* 2014; **271**: 104-112 [PMID: 24475851 DOI: 10.1148/radiol.13122883]

13 **Klöppel G**, Maillet B. Pseudocysts in chronic pancreatitis: a morphological analysis of 57 resection specimens and 9 autopsy pancreata. *Pancreas* 1991; **6**: 266-274 [PMID: 1862065]

14 **Bassi C**, Marchegiani G, Dervenis C, Sarr M, Abu Hilal M, Adham M, Allen P, Andersson R, Asbun HJ, Besselink MG, Conlon K, Del Chiaro M, Falconi M, Fernandez-Cruz L, Fernandez-Del Castillo C, Fingerhut A, Friess H, Gouma DJ, Hackert T, Izbicki J, Lillemoe KD, Neoptolemos JP, Olah A, Schulick R, Shrikhande SV, Takada T, Takaori K, Traverso W, Vollmer CR, Wolfgang CL, Yeo CJ, Salvia R, Buchler M; International Study Group on Pancreatic Surgery (ISGPS). The 2016 update of the International Study Group (ISGPS) definition and grading of postoperative pancreatic fistula: 11 Years After. *Surgery* 2017; **161**: 584-591 [PMID: 28040257 DOI: 10.1016/j.surg.2016.11.014]

15 **Wente MN**, Bassi C, Dervenis C, Fingerhut A, Gouma DJ, Izbicki JR, Neoptolemos JP, Padbury RT, Sarr MG, Traverso

LW, Yeo CJ, Büchler MW. Delayed gastric emptying (DGE) after pancreatic surgery: a suggested definition by the International Study Group of Pancreatic Surgery (ISGPS). *Surgery* 2007; **142**: 761-768 [PMID: 17981197 DOI: 10.1016/j.surg.2007.05.005]

16 **Wente MN**, Veit JA, Bassi C, Dervenis C, Fingerhut A, Gouma DJ, Izbicki JR, Neoptolemos JP, Padbury RT, Sarr MG, Yeo CJ, Büchler MW. Postpancreatectomy hemorrhage (PPH): an International Study Group of Pancreatic Surgery (ISGPS) definition. *Surgery* 2007; **142**: 20-25 [PMID: 17629996 DOI: 10.1016/j.surg.2007.02.001]

17 **Lin JW**, Cameron JL, Yeo CJ, Riall TS, Lillemoe KD. Risk factors and outcomes in postpancreaticoduodenectomy pancreaticocutaneous fistula. *J Gastrointest Surg* 2004; **8**: 951-959 [PMID: 15585382 DOI: 10.1016/j.gassur.2004.09.044]

18 **Hu BY**, Wan T, Zhang WZ, Dong JH. Risk factors for postoperative pancreatic fistula: Analysis of 539 successive cases of pancreaticoduodenectomy. *World J Gastroenterol* 2016; **22**: 7797-7805 [PMID: 27678363 DOI: 10.3748/wjg.v22.i34.7797]

19 **Laaninen M**, Bläuer M, Vasama K, Jin H, Räty S, Sand J, Nordback I, Laukkarinen J. The risk for immediate postoperative complications after pancreaticoduodenectomy is increased by high frequency of acinar cells and decreased by prevalent fibrosis of the cut edge of pancreas. *Pancreas* 2012; **41**: 957-961 [PMID: 22699198 DOI: 10.1097/MPA.0b013e3182480b81]

20 **Kim Z**, Kim MJ, Kim JH, Jin SY, Kim YB, Seo D, Choi D, Hur KY, Kim JJ, Lee MH, Moon C. Prediction of post-operative pancreatic fistula in pancreaticoduodenectomy patients using pre-operative MRI: a pilot study. *HPB (Oxford)* 2009; **11**: 215-221 [PMID: 19590650 DOI: 10.1111/j.1477-2574.2009.00011.x]

21 **Adalı G**, Bozkurt B, Ceyhan Ö, Server S, Doğusoy GB, Yüzer Y, Tokat Y. Body Mass Index and Unenhanced CT as a Predictor of Hepatic Steatosis in Potential Liver Donors. *Transplant Proc* 2019; **51**: 2373-2378 [PMID: 31402250 DOI: 10.1016/j.transproceed.2019.02.047]

22 **Yardimci S**, Kara YB, Tuney D, Attaallah W, Ugurlu MU, Dulundu E, Yegen ŞC. A Simple Method to Evaluate Whether Pancreas Texture Can Be Used to Predict Pancreatic Fistula Risk After Pancreatoduodenectomy. *J Gastrointest Surg* 2015; **19**: 1625-1631 [PMID: 25982120 DOI: 10.1007/s11605-015-2855-7]

23 **Hori M**, Onaya H, Hiraoka N, Yamaji T, Kobayashi H, Takahashi M, Mutoh M, Shimada K, Nakagama H. Evaluation of the degree of pancreatic fatty infiltration by area-based assessment of CT images: comparison with histopathology-based and CT attenuation index-based assessments. *Jpn J Radiol* 2016; **34**: 667-676 [PMID: 27581428 DOI: 10.1007/s11604-016-0572-0]

World Journal of Radiology

Submit a Manuscript: https://www.f6publishing.com

World J Radiol 2022 June 28; 14(6): 177-179

DOI: 10.4329/wjr.v14.i6.177

ISSN 1949-8470 (online)

LETTER TO THE EDITOR

Comments on "Neonatal infratentorial subdural hematoma contributing to obstructive hydrocephalus in the setting of therapeutic cooling: A case report"

Ioannis Siasios, Aggeliki Fotiadou, Yulia Rud

Specialty type: Neurosciences

Provenance and peer review: Invited article; Externally peer reviewed.

Peer-review model: Single blind

Peer-review report's scientific quality classification
Grade A (Excellent): A
Grade B (Very good): 0
Grade C (Good): 0
Grade D (Fair): D
Grade E (Poor): 0

P-Reviewer: Wang Y, China; Yao W, China

Received: February 5, 2022
Peer-review started: February 5, 2022
First decision: April 8, 2022
Revised: April 17, 2022
Accepted: May 28, 2022
Article in press: May 28, 2022
Published online: June 28, 2022

Ioannis Siasios, Neurosurgery Department, Papageorgiou Hospital, Thessaloniki 56403, Greece

Aggeliki Fotiadou, Department of Neurology, General University Hospital of Alexandroupolis, Alexandroupoli 68100, Greece

Yulia Rud, Department of Anesthesiology, European Interbalkan Medical Center, Thessaloniki 57001, Greece

Corresponding author: Ioannis Siasios, MD, MSc, Neurosurgeon, Research Scientist, Department of Neurosurgery, Papageorgiou Hospital, Ring road of Thessaloniki, N. Efkarpia, Thessaloniki 56403, Greece. siasiosj@yahoo.gr

Abstract

Although therapeutic hypothermia (TH) contributes significantly in the treatment of hypoxic ischemic encephalopathy (HIE), it could result in devastating complications such as intracranial hemorrhages. Laboratory examinations for possible coagulation disorders and early brain imaging can detect all these cases that are amenable to aggravation of HIE after the initiation of TH.

Key Words: Therapeutic hypothermia; Hypoxic ischemic encephalopathy; Hemostatic disorders; Intracranial hemorrhage; Magnetic resonance imaging

Core Tip: It has not been yet elucidated if the initiation of therapeutic hypothermia (TH) contributes significantly to better outcomes in cases with already confirmed intracranial hemorrhage and hemostatic disorders. In such cases a close follow up with brain magnetic resonance imaging before and after the initiation of TH and repeated laboratory and clinical examinations may promptly identify neonates requiring emergent neurosurgical intervention.

Citation: Siasios I, Fotiadou A, Rud Y. Comments on "Neonatal infratentorial subdural hematoma contributing to obstructive hydrocephalus in the setting of therapeutic cooling: A case report". *World J Radiol* 2022; 14(6): 177-179
URL: https://www.wjgnet.com/1949-8470/full/v14/i6/177.htm
DOI: https://dx.doi.org/10.4329/wjr.v14.i6.177

TO THE EDITOR

Hypoxic ischemic encephalopathy (HIE) is thought to be a significant cause of morbidity and mortality at term and pre-term infants[1,2]. As stated in the literature, HIE is an evolving pathological process which within hours after its initiation promotes neuronal cell death through several biochemical events due to primary and secondary neuronal cell's energy crisis such as hypoperfusion, extracellular concentration of amino-acids, nitric oxide and free radicals and finally membrane depolarization[3]. Based on newborn's neurological status expressed by Sarnat scale, HIE is divided to mild, moderate and severe [4]. Diagnosis and follow up is based on patient's neurological status, laboratory monitoring as well as brain imaging studies such as cranial ultrasound and magnetic resonance imaging (MRI) of the head which is the gold standard imaging modality for intracranial lesions[5].

Therapeutic hypothermia (TH) is considered the first line treatment of HIE[6]. Several studies in the past revealed that TH can reduce neonatal mortality up to 20% in developed countries[7]. TH is widely used during the last decade for moderate to severe cases of HIE and it can be induced either as whole-body cooling or selective head cooling with a great variation in treatment protocols[8,9]. According to a published case series, hypothermia is limited to 33-34 degrees of Celsius for around 72 h under close medical surveillance and is slowly reinstated at normal body temperatures by patient rewarming with an increase rate of 0.5 Celsius degree per hour[3,5]. TH is applied only 6 h after birth in newborns with low Apgar score and a gestational age above 36 wk with evidence of moderate to severe HIE[5]. The literature describes several side effects of TH with an incidence around 20% of treated cases such as skin burns, electrolyte disturbances, low blood pressure, thrombocytopenia, prolonged prothrombin time (PT), and activated thromboplastin time[3].

We have read with great interest the case reported by Rousslang *et al*[10]. The authors eloquently highlighted the potential association between TH and increased risk of intracranial hemorrhage in neonates with HIE. They described the case of a term neonate that after an emergent C-section delivery required intubation due to cardiopulmonary instability[10]. According to the authors, the neonate fulfilled the criteria for TH which was applied from the day one. It is very interesting that the patient had from his first day of life pathological values of several parameters of coagulation mechanism such prolonged international normalized ration (INR), time of thromboplastin, activated partial thromboplastin time and low number of platelets. Authors tried to restore these pathological findings of coagulation parameters during the next four days. This is a gray zone in the literate regarding contraindications for TH. The question that has to be answered is whether a neonate with pathological laboratory findings of his coagulation mechanism is eligible for TH initiation without prior restoration of these abnormal values. We have to recognize that the time frame for such decisions is short in order to prevent a possible permanent neurological damage. It is strongly supported by the literature that TH can induce abnormalities of coagulation mechanism and indirectly favor occurrence of intracranial hemorrhages similar to the one that Rousslang *et al*[10] describe in their case report[3,11]. Obviously, this effect can be reinforced in patients with already pathological ratings of coagulation parameters.

In addition, the first screening of the neonate with head ultrasound revealed a left grade I germinal matrix hemorrhage. Although the patient already had a small intracranial hemorrhage authors applied TH. It is well known that around 38% of cases treated with TH can have an intracranial hemorrhage [12]. This is a finding that could be studied more thoroughly with an MRI scan before the application of TH as the MRI is more sensitive for the detection of any other hemorrhagic lesion, rendering it a potential first reference screening study for the neonate. Additionally, a brain MRI could be more valuable in assessing the severity of HIE and thus is a prognostic tool of great significance[12-14]. The coexistence of HIE and intracranial hemorrhages is another gray zone that requires more extensive investigation regarding the final outcome for the neonates receiving TH[13,14]. The current published case series refers to MRI scans performed usually several hours after the initiation of TH. Another issue that should be clarified in the future is whether any type of intracranial hemorrhage constitutes a contraindication for the initiation of any TH protocol.

Finally, it is well presented by the authors that any type of imaging screening combined with laboratory and clinical follow up of the neonates during TH can successfully detect any emergent intracranial hemorrhage. In these cases, prompt neurosurgical consultation can remarkably affect neurological outcome and prognosis for the neonates[15].

FOOTNOTES

Author contributions: Siasios I and Fotiadou A, Rud Y designed research; Siasios I, Fotiadou A, Rud Y performed research; Siasios I, Fotiadou A and Rud Y analyzed data; Siasios I and Fotiadou A wrote the letter; and Siasios I, Fotiadou A and Rud Y revised the letter.

Conflict-of-interest statement: All the authors declare that they have no conflict of interest.

Country/Territory of origin: Greece

ORCID number: Ioannis Siasios 0000-0001-7945-9604; Aggeliki Fotiadou 0000-0002-8614-2688; Yulia Rud 0000-0002-6063-4043.

S-Editor: Liu JH
L-Editor: A
P-Editor: Liu JH

REFERENCES

1 **Vannucci RC**. Hypoxic-ischemic encephalopathy. *Am J Perinatol* 2000; **17**: 113-120 [PMID: 11012134 DOI: 10.1055/s-2000-9293]
2 **Lee AC**, Kozuki N, Blencowe H, Vos T, Bahalim A, Darmstadt GL, Niermeyer S, Ellis M, Robertson NJ, Cousens S, Lawn JE. Intrapartum-related neonatal encephalopathy incidence and impairment at regional and global levels for 2010 with trends from 1990. *Pediatr Res* 2013; **74** Suppl 1: 50-72 [PMID: 24366463 DOI: 10.1038/pr.2013.206]
3 **Datta V**. Therapeutic Hypothermia for Birth Asphyxia in Neonates. *Indian J Pediatr* 2017; **84**: 219-226 [PMID: 27966094 DOI: 10.1007/s12098-016-2266-0]
4 **Sarnat HB**, Sarnat MS. Neonatal encephalopathy following fetal distress. A clinical and electroencephalographic study. *Arch Neurol* 1976; **33**: 696-705 [PMID: 987769 DOI: 10.1001/archneur.1976.00500100030012]
5 **Chiang MC**, Jong YJ, Lin CH. Therapeutic hypothermia for neonates with hypoxic ischemic encephalopathy. *Pediatr Neonatol* 2017; **58**: 475-483 [PMID: 28416250 DOI: 10.1016/j.pedneo.2016.11.001]
6 **Wassink G**, Davidson JO, Dhillon SK, Zhou K, Bennet L, Thoresen M, Gunn AJ. Therapeutic Hypothermia in Neonatal Hypoxic-Ischemic Encephalopathy. *Curr Neurol Neurosci Rep* 2019; **19**: 2 [PMID: 30637551 DOI: 10.1007/s11910-019-0916-0]
7 **Edwards AD**, Brocklehurst P, Gunn AJ, Halliday H, Juszczak E, Levene M, Strohm B, Thoresen M, Whitelaw A, Azzopardi D. Neurological outcomes at 18 mo of age after moderate hypothermia for perinatal hypoxic ischaemic encephalopathy: synthesis and meta-analysis of trial data. *BMJ* 2010; **340**: c363 [PMID: 20144981 DOI: 10.1136/bmj.c363]
8 **Giannakis S**, Ruhfus M, Rüdiger M, Sabir H; German Neonatal Hypothermia Network. Hospital survey showed wide variations in therapeutic hypothermia for neonates in Germany. *Acta Paediatr* 2020; **109**: 200-201 [PMID: 31432551 DOI: 10.1111/apa.14979]
9 **Gunn AJ**, Laptook AR, Robertson NJ, Barks JD, Thoresen M, Wassink G, Bennet L. Therapeutic hypothermia translates from ancient history in to practice. *Pediatr Res* 2017; **81**: 202-209 [PMID: 27673420 DOI: 10.1038/pr.2016.198]
10 **Rousslang LK**, Rooks EA, Meldrum JT, Hooten KG, Wood JR. Neonatal infratentorial subdural hematoma contributing to obstructive hydrocephalus in the setting of therapeutic cooling: A case report. *World J Radiol* 2021; **13**: 307-313 [PMID: 34630916 DOI: 10.4329/wjr.v13.i9.307]
11 **Rao R**, Trivedi S, Vesoulis Z, Liao SM, Smyser CD, Mathur AM. Safety and Short-Term Outcomes of Therapeutic Hypothermia in Preterm Neonates 34-35 Weeks Gestational Age with Hypoxic-Ischemic Encephalopathy. *J Pediatr* 2017; **183**: 37-42 [PMID: 27979578 DOI: 10.1016/j.jpeds.2016.11.019]
12 **Walas W**, Wilińska M, Bekiesińska-Figatowska M, Halaba Z, Śmigiel R. Methods for assessing the severity of perinatal asphyxia and early prognostic tools in neonates with hypoxic-ischemic encephalopathy treated with therapeutic hypothermia. *Adv Clin Exp Med* 2020; **29**: 1011-1016 [PMID: 32820870 DOI: 10.17219/acem/124437]
13 **Lakatos A**, Kolossváry M, Szabó M, Jermendy Á, Barta H, Gyebnár G, Rudas G, Kozák LR. Neurodevelopmental effect of intracranial hemorrhage observed in hypoxic ischemic brain injury in hypothermia-treated asphyxiated neonates - an MRI study. *BMC Pediatr* 2019; **19**: 430 [PMID: 31718607 DOI: 10.1186/s12887-019-1777-z]
14 **Weeke LC**, Groenendaal F, Mudigonda K, Blennow M, Lequin MH, Meiners LC, van Haastert IC, Benders MJ, Hallberg B, de Vries LS. A Novel Magnetic Resonance Imaging Score Predicts Neurodevelopmental Outcome After Perinatal Asphyxia and Therapeutic Hypothermia. *J Pediatr* 2018; **192**: 33-40.e2 [PMID: 29246356 DOI: 10.1016/j.jpeds.2017.09.043]
15 **van Steenis A**, Fumagalli M, Kruit MC, Peeters-Scholte CMPCD, de Vries LS, Steggerda SJ. Cranial Ultrasound Is an Important Tool in the Recognition of Life-Threatening Infratentorial Hemorrhage in Newborns. *Neuropediatrics* 2021; **52**: 170-178 [PMID: 33316833 DOI: 10.1055/s-0040-1716899]

Published by **Baishideng Publishing Group Inc**
7041 Koll Center Parkway, Suite 160, Pleasanton, CA 94566, USA
Telephone: +1-925-3991568
E-mail: bpgoffice@wjgnet.com
Help Desk: https://www.f6publishing.com/helpdesk
https://www.wjgnet.com